Fakultät Mathematik und
Naturwissenschaften der
Technischen Universität Dresden

TECHNISCHE
UNIVERSITÄT
DRESDEN

Exploring the Mechanical Stability and Visco-elasticity of Membrane Proteins by Single-Molecule Force Measurements

Dissertation

zur Erlangung des akademischen Grades

Doctor rerum naturalium

(Dr. rer. nat.)

vorgelegt von

Harald Janovjak

geboren am 23. Oktober 1979 in Basel (Schweiz)

1. Gutachter:	Prof. Dr. Petra Schwille *Technische Universität Dresden*
2. Gutachter:	Prof. Dr. Daniel J. Müller *Technische Universität Dresden*
3. Gutachter:	Prof. Dr. Mervyn Miles *Universität von Bristol, England*

Eingereicht am 3. August 2005.

Verteidigt am 19. Dezember 2005.

Abstract

Relatively little is known about the folding and stability of membrane proteins. Conventional thermal or chemical unfolding techniques probe the average behavior of large numbers of molecules and thus cannot resolve co-existing minor and major unfolding pathways and intermediates. Here, I applied single-molecule force measurements based on an atomic force microscope (AFM) to characterize the stability of the membrane protein bacteriorhodopsin (BR). In these mechanical unfolding experiments, an external pulling force played the role of the denaturant and lead to unfolding of the three-dimensional structure of individual proteins. It was found that single BRs unfold step-wise in a well-defined sequence of stable intermediates and in different unfolding pathways. Although single α-helices were sufficiently stable to unfold in individual steps they also exhibited certain probabilities to unfold in pairs. These observations support the ‘two-stage’ and the ‘helical-hairpin’ model of membrane protein folding. Dynamic force measurements showed that α-helices and helical hairpins are relatively rigid structures, which are stabilized by narrow energy barriers and have stabilities between 100-10’000 seconds. These forced unfolding experiments were complemented with the development of new force measurement techniques. It is demonstrated that hydrodynamic effects need to be considered to obtain more complete kinetic pictures of single molecules. In addition, two force spectroscopy approaches to measure the complex visco-elastic response of single molecules are presented and applied to BR. These experiments revealed that the unfolding patterns of single proteins are dominated by purely elastic polypeptide extension and determined the dissipative interactions associated with the unfolding of single α-helices. In addition, it was found that kinks result in a reduced unfolding cooperativity of α-helices.

" Why do we fall, Master Bruce ?
So that we might better learn to pick ourselves up. "

Pennyworth, 2005

Table of Contents

1. INTRODUCTION **1**

1.1 Atomic force microscopy 1
  1.1.1 History and physical principles 1
  1.1.2 Imaging modes 3
  1.1.3 Application to biological samples 4

1.2 Transmembrane proteins 6
  1.2.1 Biological relevance 6
  1.2.2 Structure, folding and stability 7
  1.2.3 Bacteriorhodopsin as a model system for transmembrane proteins 8

2. FORCE SPECTROSCOPY **10**

2.1 Introduction 10

2.2 Force-distance measurements 12

2.3 Force sensitivity 14

2.4 Spring constant calibration 16

2.5 Polymer extension models 18

2.6 Force spectroscopy model systems 20
  2.6.1 Abstract 20
  2.6.2 Experimental procedures 20
  2.6.3 Results and discussion 21

2.7 Conclusions 24

3. MECHANICAL STABILITY OF SINGLE BACTERIORHODOPSINS **25**

3.1 Introduction 25

3.2 Theoretical considerations 25
  3.2.1 Sample preparation 25
  3.2.2 Relation between unfolding force and stability 27
  3.2.3 Monte-Carlo simulations 31

3.3 Experimental procedures 33

3.4 Results and discussion 36
  3.4.1 Selection of F-D curves 36
  3.4.2 Unfolding pathways of single bacteriorhodopsins 37
  3.4.3 Unfolding forces depend on pulling speed 41
  3.4.4 Energy landscape of secondary structure elements 43
  3.4.5 Unfolding pathways depend on pulling speed 45

3.5 Conclusions 46

4. EXTENDED RANGE OF AFM FORCE LOADING RATES 48

4.1 Introduction 48

4.2 Experimental procedures 49

4.3 Results and discussion 49
    4.3.1 Hydrodynamic drag force acting on an AFM cantilever 49
    4.3.2 Correcting hydrodynamic effects 51
    4.3.3 Comparison to small cantilevers and other force probe methods 53
    4.3.4 Other factors limiting AFM pulling speeds 54

4.4 Conclusions 55

5. VISCO-ELASTICITY OF SINGLE BACTERIORHODOPSINS 56

5.1 Introduction 56

5.2 Theoretical considerations 57
    5.2.1 Resonance response of an AFM cantilever 57
    5.2.2 Visco-elastic response of single molecules 60
    5.2.3 Force modulation spectroscopy 61
    5.2.4 Thermal motion spectroscopy 63

5.3 Experimental procedures 64

5.4 Results and discussion 66
    5.4.1 Signal-to-noise ratio and time resolution 66
    5.4.2 Visco-elastic properties of single bacteriorhodopsins 69
    5.4.3 Uncovering new unfolding intermediates 71
    5.4.4 Resonstructing F-D curves: A novel approach to detect unfolding events 73

5.5 Conclusions 75

6. GENERAL CONCLUSIONS 76

7. OUTLOOK 78

7.1 Hidden complexity in the forced unfolding of single proteins 78

7.2 Probing the folding of single (membrane) proteins 79

7.3 Single-molecule visco-elasticity measurements 81

APPENDIX 82

Abbreviations 82

Symbols 82

List of publications 84

Acknowledgements 86

BIBLIOGRAPHY 87

1. Introduction

1.1 Atomic force microscopy

1.1.1 History and physical principles

In 1986, G. Binnig, C.F. Quate and C. Gerber introduced the AFM, a revolutionary microscope that works very differently from light or electron microscopes (Binnig *et al.*, 1986). The AFM measures interaction forces between an ultra-sharp tip and a sample surface to generate a topographical surface image. It belongs to the family of scanning probe microscopes (SPMs), each of which uses a specialized probe to detect different physical or chemical interactions to surfaces. The detectable interactions are tunneling currents in the scanning tunneling microscope (Binnig and Rohrer, 1983), optical signals in the scanning near field optical microscope (Ash and Nicholls, 1972; Meixner and Kneppe, 1998), magnetic forces in the magnetic force microscope (Saenz *et al.*, 1987), or ion conductance in the scanning ion conductance microscope (Proksch *et al.*, 1996), just to mention a few. The term 'atomic force' refers mainly to the high spatial resolution of the AFM as, in an ideal case, the instrument can resolve single atoms. Such true atomic resolution is possible with the AFM under restrictive conditions, e.g. in ultrahigh vacuum and for atomically flat samples (Giessibl, 1995; Sugawara *et al.*, 1995). There are different types of forces interacting between the AFM tip and the surface, most of which relate to those occurring between surfaces in close proximity, e.g. electrostatic double-layer (EDL) forces or van der Waals interactions (Table 1; Israelachvili, 1991).

Type of interaction	**Direction of force**	**Interaction range**
Steric (hard-core repulsion)	Repulsive	Very short ranged (≤ 0.1 nanometer (nm))
Van der Waals	Usually attractive, but can be repulsive	Short ranged (a few nm)
Electrostatic (Coulomb, ionic, double-layer)	Attractive or repulsive	Long ranged (nm to micrometer (□m))

Table 1 Interaction forces detected in the AFM. The three most common interaction forces observed in an AFM are summarized with their force direction and interaction range. Van der Waals interactions, electrostatic forces, and their interplay are more extensively addressed in Chapter 3.2.1.

Measuring intermolecular forces on such small scales requires (i) a tip with appropriate size to sense the local force (ii) a suited mechanism to amplify the interaction force into a measurable quantity (e.g. voltage), and (iii) a system to precisely control the relative position of the tip on the sample.

Typically, the tip of the AFM has a conical or pyramidal shaft ending in an apex with 5-50 nm radius (Figure 1-1 C; Tortonese, 1997). It is mounted to the end of a flexible cantilever (Figure 1-1 B), which bends in response to interaction forces between the tip and the sample surface. Thus, by introducing the cantilever, nanoscopic forces as small as a few piconewton (pN) can be measured by converting them into deflection of a microscopic cantilever. In the most typical optical detection setup, the cantilever deflection is detected by reflecting a laser beam from the backside of the cantilever onto a split position-sensitive photodetector (Figure 1-1 A) (Alexander *et al.*, 1989; Meyer and Amer, 1988)[1]. As the cantilever bends, the position of the laser beam on the detector shifts from its initial central point. The resulting voltage difference between the segments of the photodiode gives a direct and linear measure for the deflection of the cantilever with a resolution down to 0.1 Ångstrom (Å) (Sarid, 1994).

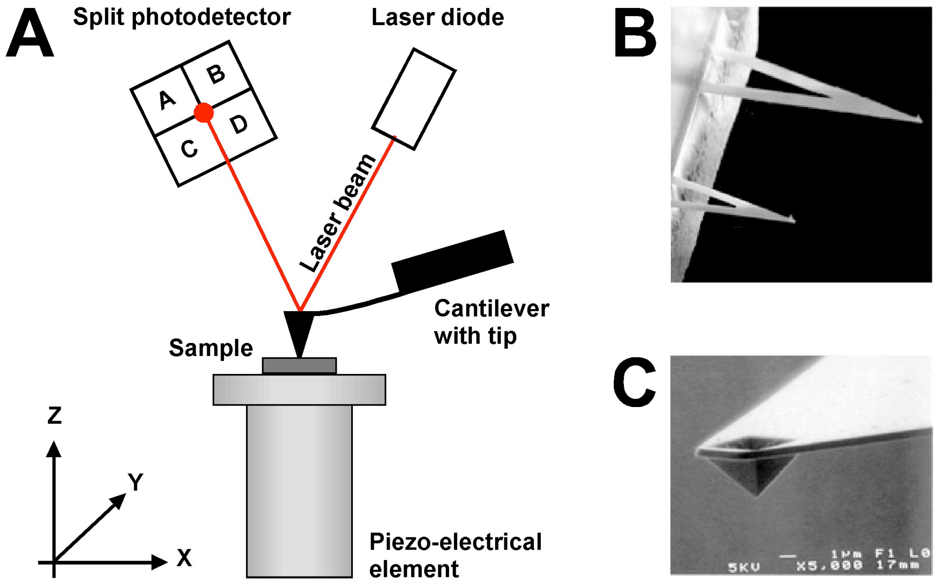

Figure 1-1 AFM setup and cantilever. (A) The sample is mounted on a three-axis piezo-electrical element and scanned under the tip attached to the cantilever. The deflection of the cantilever is measured using a laser beam reflected of its back. The voltage difference between the upper and lower half of the photodetector (A+B-(C+D)) is a measure for the vertical deflection of the cantilever. (B and C) Scanning electron micrographs of V-shaped AFM cantilevers, which are micro-fabricated from silicon or silicon nitride in a lithographic process equivalent to the fabrication of integrated circuits. They typically are between 30 μm and 250 μm long, several hundreds of nm thick, and covered by a thin metal coating to increase the reflectivity. Images courtesy of Digital Instruments, Veeco Metrology, Santa Barbara, CA, USA.

---

[1] Other detection systems are based on capacitance (Göddenhenrich *et al.*, 1990; Neubauer *et al.*, 1990) or interferometry (Erlandsson *et al.*, 1988; Martin *et al.*, 1987; Schönenberger and Alvarado, 1989).

The final step from the force sensor to a microscope is comparably simple: each point on the sample is addressed with a positioning system to create a map of local interaction forces. Most commonly piezo-electrical elements provide reliable lateral X-Y-positioning with nm accuracy over scan-sizes as larges a few hundred μm. While the lateral displacement is used for scanning, movements in Z-direction adjust the vertical position of the sample allowing the tip to gently contour the surface (see next chapter).

1.1.2 Imaging modes

The AFM can be operated in different imaging modes, which are either referred to as quasi-static or dynamic imaging modes. I will firstly introduce constant-force contact mode as a typical representative of the quasi-static imaging modes. To obtain an image in contact mode, the tip is scanned in contact with the sample surface and the deflection signal is monitored along the trace of the tip. Using a feedback loop, the Z-position of the sample is adjusted such that the cantilever deflection (and hence the applied force) remains at a preset value (Figure 1-2 A). Recording the sample displacement along the Z-axis together with the lateral position of the tip then allows generating a topographical image of the sample. Small errors in the regulation of the force are inevitable since the feedback loop can only react as the cantilever bends. This error signal is used in error signal imaging and provides an image related to the first derivative of the topography in scan direction, thus emphasizing edges of the surface topography (Figure 1-2 B; Putman *et al.*, 1992). In the quasi-static imaging modes, the operator can vary the tip-sample force from gently touching to deep carving of the surface. Typical contact forces during imaging of biological samples range from 100 - 300 pN (Müller *et al.*, 1995; Müller *et al.*, 1999). Higher forces are required to manipulate matter but potentially deform soft structures and lower the resolution due to an increased tip-sample contact area (Weihs *et al.*, 1991).

Another approach to reduce sample deformation arising from tip-sample contact is the minimization of the contact time using dynamic imaging modes. In tapping mode, the cantilever is excited to oscillate close to its natural resonant frequency (Figure 1-2 C; Putman *et al.*, 1994). Once during every cycle, the tip interacts with the sample and the consequent modulation of the oscillation amplitude is amplified in the feedback loop. Tapping mode with oscillation amplitudes of a few nm is especially well suited to image fragile samples such as cells or dynamic biological systems (see below). Due to dissipative tip-sample interactions one often observes a phase shift in the cantilever oscillation. This phase shift can be exploited in phase mode imaging to gain additional information about the properties of the scanned surface (Figure 1-2 D; Cleveland *et al.*, 1998; Stark *et al.*, 2001; Tamayo and Garcia, 1996; Tamayo and Garcia, 1998). However, the results obtained in dynamic imaging modes exhibit a great variance in image quality, which reflects the fact that the cantilever oscillation follows highly non-linear dynamics (e.g., see Garcia and Perez, 2002). In addition, vertical or lateral forces are not necessarily reduced in dynamic imaging modes compared to the quasi-static ones.

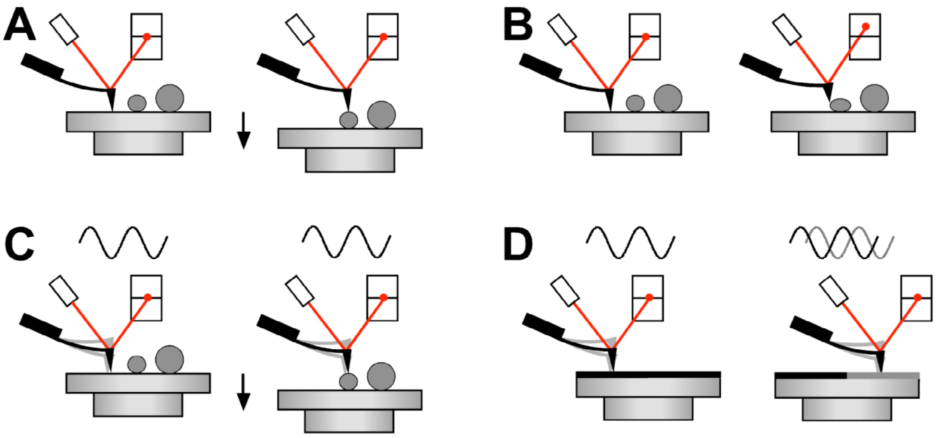

Figure 1-2 Imaging modes of the AFM. The cantilever is quasi-static in contact mode (A) and error signal mode (B) while it is oscillating in tapping mode (C) and phase imaging (D). Contact and tapping mode reveal the surface topography by maintaining the deflection signal or oscillation amplitude at a setpoint value. The error signal reveals the edges of the surface and phase imaging allows mechanical properties of surface to be probed.

1.1.3 Application to biological samples

The ability of the AFM to image biological samples was shown shortly after its invention (Marti *et al.*, 1988). The implementation of a fluid cell (Drake *et al.*, 1989) and improved sample preparation techniques (Wagner, 1998) then further improved the life science capabilities of the instrument. Most interestingly for biologists, the AFM is capable of revealing the surface topography of soft objects in buffer solution and at physiological temperatures. Thus the AFM has been applied to a variety of biological systems ranging from single biological molecules (such as proteins, nucleic acids, polysaccharides) to molecular assemblies and cells (for recent reviews, see Abu-Lail and Camesano, 2003; Dufrene, 2004; Hansma *et al.*, 2004; Müller *et al.*, 2002; Scheuring *et al.*, 2005). Today the AFM, and other members of the SPM family, are still the only instruments that provide images of functional bio-molecular structures in their native environment and allow the direct observation of dynamic biological processes (e.g., see Ando *et al.*, 2001; Engel and Müller, 2000; Guthold *et al.*, 1999; Kasas *et al.*, 1997; Viani *et al.*, 2000).

To image the native conformation of biological objects at high resolution, it appeared crucial to understand and adjust the interaction forces between tip and sample (Müller *et al.*, 1995; Weihs *et al.*, 1991). It was shown that the resolution and precision of topographs of native proteins critically depend on the electrolyte concentration (Müller *et al.*, 1999). At an electrolyte concentration, which completely compensates the repulsive EDL interaction, the tip reversibly deforms the surface. Consequently, a small repulsive EDL force is desirable to minimize interactions between the tip and sample allowing the proteins to be imaged at sub-nm resolution (Müller *et al.*, 1999). As an example, Figure 4-1 shows an AFM topograph of native purple membrane (PM) patches, whose only protein content is the membrane protein BR (also see Chapter 1.2.3). High-resolution images of the cytoplasmic and extracellular side of the membrane reveal single BRs in trimers, which order in a hexagonal lattice.

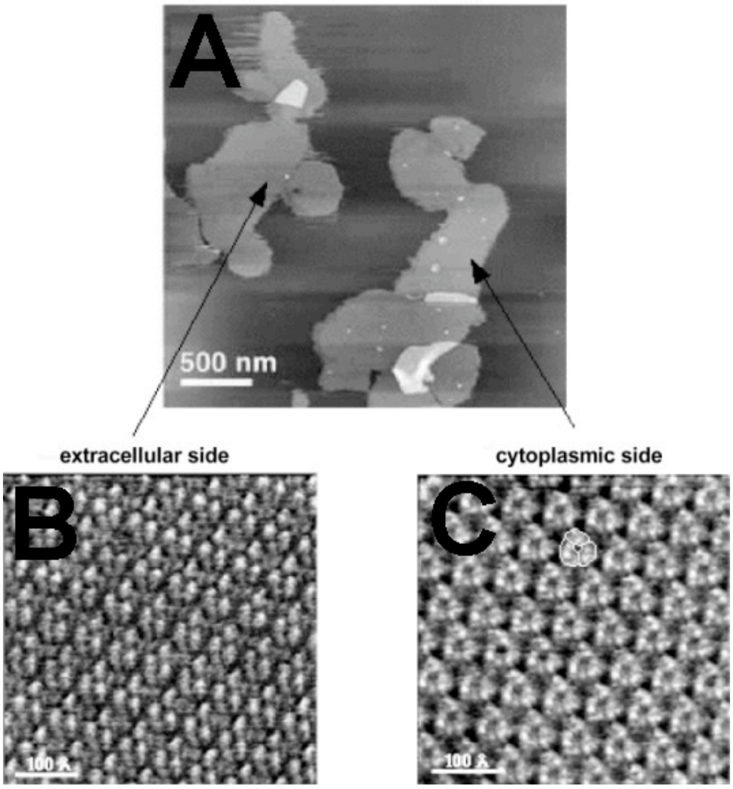

Figure 1-3 Force microscopy of native PM patches. (A) Low magnification image of PM recorded at room temperature in buffer solution. (B and C) High resolution images showing the extracellular and the cytoplasmic surface of the membrane. In Figure C one trimer is contoured. The sample was prepared as described in Chapter 3.2.1 and imaged in 150 mM KCl, 10 mM Tris, pH 7.8. Images are courtesy of D.J. Müller, Dresden.

Due to surface roughness, surface flexibility and the intrinsic mobility of biological specimens, the achievable resolution in the AFM is often limited to ≈ one nm. Nevertheless, single bio-macromolecules, their sub-structures, their oligomeric states and structural assemblies can be resolved (for reviews, see Czajkowsky *et al.*, 2000; Engel and Müller, 2000; Frederix *et al.*, 2004; Müller *et al.*, 2002). During imaging the AFM tip can also be used as a sensor to probe the local elasticities of single proteins and to directly observe functionally related conformational changes (Müller *et al.*, 2002). Finally, functionalized probes enabled researchers to image biological surfaces with simultaneous detection of multiple (bio-)chemical or biophysical information, such as surface charges, ligand binding, or sample elasticity (e.g., see Butt *et al.*, 1995; Frederix *et al.*, 2004; Heinz and Hoh, 1999; Philippsen *et al.*, 2002; Radmacher *et al.*, 1992; Scheuring *et al.*, 2002; Stroh *et al.*, 2004).

1.2 Transmembrane proteins

1.2.1 Biological relevance

Biological membranes are essential to all organisms as they provide permeability barriers and environments for a multitude of functional processes. Even in the simplest organisms, membranes are highly complex and dynamic compartments as they consist of many different types of proteins and lipids. Transmembrane proteins embedded in the lipid bilayer membranes fulfill many of the essential functions of the membranes. They act, for example, as sensors, receptors, and channels. They are involved in the regulation of pH and ion concentrations and establish an electrochemical potential across the membrane. In line with their vital roles in the cell, membrane proteins comprise approximately 20-30% of the total proteins in organisms of every kingdom (Krogh *et al.*, 2001; Wallin and von Heijne, 1998). In the case of *E. coli* (*C. elegans*) this means that there are ≈ 900 (≈ 8900) different membrane proteins further indicating the highly heterogeneous character of biological membranes.

Due to their essential roles and abundancy, membrane proteins also form major targets for drug development. Among the ≈ 16’000 missense mutations linked to human diseases a large number could be associated with membrane proteins (Sanders and Myers, 2004). Interestingly a majority of these mutations influence folding or trafficking rather than specifically affecting the residues involved in protein function. In this context it might be interesting to note that G-protein coupled receptors (GPCRs; also see below) are the most important targets for drug discovery and account for 40-60% of all prescription drugs (Filmore, 2004; Torres *et al.*, 2003).

1.2.2 Structure, folding and stability

The steadily increasing number of known gene sequences coding for membrane proteins is in sharp contrast with our lacking knowledge of their three-dimensional structures and folding in the anisotropic environment of the lipid bilayer. Less than 1% of the structures deposited within the Protein Data Bank (RCSB, see bibliography) are membrane proteins and mechanistic information is only available for a few of these. Nevertheless, two distinct classes of membrane proteins have been structurally characterized. The all-β class tends to form large rigid transmembrane pores known as β-barrels (Schulz, 2002; Schulz, 2003). They often are toxins or found in the outer membranes of gram-negative bacteria, mitchondria, and chloroplast, where they facilitate the diffusion of small to large molecules across the membrane. The larger α-helical class includes cell-surface receptors, ion channels, transporters, and redox proteins of widely different structure and function (e.g., see Bezanilla, 2005; DeFelice, 2004; Filipek *et al.*, 2003; Pusch and Jentsch, 2005). An estimated 20% of the α-helical membrane proteins have single transmembrane α-helices, which either hetero- or homo-oligomerize to form helical bundles (Krogh *et al.*, 2001). While the α-helical membrane proteins vary widely in the number of membrane-spanning regions and membrane topologies, the transmembrane domains are typically composed of 20 to 27 amino acids (aas). These α-helices can be tilted with respect to the membrane plane and can exhibit irregular features such as kinks or short unstructured segments (for an overview, see Popot and Engelman, 2000).

Initially, a two-stage model was proposed for the sequential folding of α-helical membrane proteins such as BR (Popot and Engelmann, 1990; Popot *et al.*, 1987). According to this model, the α-helices are first formed independently within the membrane and then assemble into the functional protein. Thus the α-helices act comparably to the domains of water-soluble proteins. The idea for this model came from experiments, which demonstrated that isolated fragments of BR reassemble spontaneously into a fully functional form in lipid bilayers (Popot *et al.*, 1987). The spontaneous assembly is consistent with the native protein residing in a free energy minimum. However, for larger proteins it seems that bundles of two, three or more α-helices can sometimes be needed to help the remaining α-helices fold (for an overview, see Popot and Engelman, 2000). The two-stage model has also been refined to include extra steps of ligand binding and folding of extramembranous loops (Engelman *et al.*, 2003; White and Wimley, 1999). It is important to note that membrane proteins have been largely excluded from more detailed folding studies due to major difficulties in mimicking the native, anisotropic environment of the membrane with its hydrophobic interactions (Seddon *et al.*, 2004; Torres *et al.*, 2003).

As for water-soluble proteins (Radford, 2000; Weissman and Kim, 1991), it is suggested that the folding intermediates of membrane proteins are guided by the same interactions that stabilize the final folded state (Booth *et al.*, 2001; Haltia and Freire, 1995; Popot and Engelman, 2000; White and Wimley, 1999). Hydrophobic interactions play a major role in the stability of membrane proteins in addition to van der Waals forces, inter- and intrahelix hydrogen bonds and salt bridges. Considerable effort has been devoted to investigate the unfolding of membrane proteins using conventional thermal and chemical denaturation methods (Chen and Gouaux, 1999; Cladera *et al.*, 1992; Shnyrov and Mateo, 1993; Taneva *et al.*, 1995). However, since membrane proteins cannot be denatured to a fully unfolded state, the free energy of the folded structures is not known. From thermodynamic predictions it became clear that the transfer of hydrophobic aa residues to the hydrophobic regions of the membrane is linked to a free energy gain of ≈ 1 kcal/mol (White and Wimley, 1999). Taking into account that hydrogen bonds are much stronger in the hydrophobic membrane core than in water (≈ 6 kcal/mol in the membrane compared to ≈ 0.5 kcal/mol in water) each α-helix is estimated to be stabilized by an energy of ≈ 80 – 100 kcal/mol (Engelman and Steitz, 1981; White and Wimley, 1999).

1.2.3 Bacteriorhodopsin as a model system for transmembrane proteins

Under anaerobic conditions the archea *Halobacter salinarium* expresses BR, a 248 aa long retinal-containing membrane protein (Oesterhelt and Stoeckenius, 1971). BR pumps protons from the inside to the outside of the cell upon light absorption (Oesterhelt and Stoeckenius, 1973) and thus forms a proton gradient across the cell membrane. Unlike chlorophyll-containing eucaryotic or eubacterial photosynthetic reaction centers, BR uses a retinal as the chromophore, which is covalently linked to a lysine by a protonated Schiff base (Oesterhelt and Stoeckenius, 1971). Due to a few almost unique features BR became a widely used model system for ion translocating membrane proteins. After *in vivo* expression BR accumulates in the PM patches of the cell membrane whose purple color originates from the retinal content. In the PM, BR naturally assembles into trimers, which order in a hexagonal lattice (Blaurock and Stoeckenius, 1971). This native 2D crystallinity of BR promoted the development of electron crystallography, and currently BR is one of the few membrane proteins for which several atomic models are available (Essen *et al.*, 1998; Grigorieff *et al.*, 1996; Kimura *et al.*, 1997; Luecke *et al.*, 1999; Pebay-Peyroula *et al.*, 1997). The retinal was revealed to be embedded in seven closely packed membrane α-helices lettered A to G, which are connected by extramembranous loops (Figure 1-4).

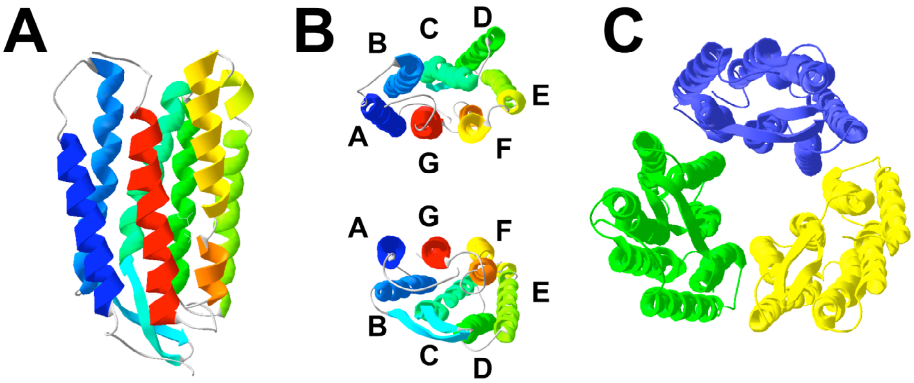

Figure 1-4: Model of the three-dimensional structure of BR. (A) Side view of a single BR. (B) Cytoplasmic (top) and extracellular surface (bottom). (C) Extracellular view of a BR trimer. Different structural models have been published for BR. The structure shown here is taken from Essen *et al.* (PDB-ID 1BRR; Essen *et al.*, 1998).

This structural motif is common among a large class of related GPCRs. However, the loops of BR and the GPCRs are substantially different and the GPCRs are subject to post-translational modifications (Filipek *et al.*, 2003; Okada and Palczewski, 2001). The structural and functional significance of many residues in BR was tested by mutagenesis (e.g., see Flitsch and Khorana, 1989; Marti *et al.*, 1991; Otto *et al.*, 1989; Otto *et al.*, 1990). As BR can routinely be refolded and recrystallized *in vitro,* detailed studies of the folding pathways and folding kinetics of BR are available (for reviews, see Booth, 2000; Booth *et al.*, 2001). The visible absorbance of the retinal cofactor, around 550 nm, and the proton-pumping activity can be used to characterize the protein under different conditions (Muccio and Cassim, 1979; Racker and Hinkle, 1974) as they and illustrate the structure-function relationship of the protein. Thus with increasing knowledge of its structural and functional properties, BR has become a paradigm for a-helical membrane proteins in general and for ion transporters in particular.

2. Force spectroscopy

2.1 Introduction

In the following, a non-imaging application of the AFM called force spectroscopy is introduced that will later be applied to study the stability of single proteins[2]. I will begin with a comparison of the AFM to other force probe methods and give a short overview the historical development of the technique. Then I will discuss the critical aspects of force spectroscopy measurements, such as force sensitivity, force calibration, and polymer extension models, as these are essential for a quantitative understanding of single-molecule experiments. In the last chapter, results will be presented demonstrating the application of force spectroscopy to investigate the mechanical properties of biological macromolecules. The two most important biological model systems for force spectroscopy, the polysaccharide dextran and a multi-domain protein consisting of domains of the muscle protein titin, were studied.

As already discussed in Chapter 1.1, the AFM was initially developed as an imaging technique. However, today the tip of the AFM is increasingly used as a nanomanipulator (Fotiadis *et al.*, 2002; Ikai and Afrin, 2003; Janshoff *et al.*, 2000; Rief and Grubmüller, 2002). As demonstrated within the past decade, the combination of AFM imaging and manipulation made precise and controlled modifications of biological systems from a macroscopic scale down to the scale of individual molecules possible. These applications take advantage of the pN force sensitivity and Ångstrom (Å) positioning capabilities of the AFM, which allow inter- and intramolecular forces to be measured on the nm length scale. With this ability, the AFM joins a range of other force measurement techniques that are designed to study molecular interactions, such as glass microfibers (Ishijima *et al.*, 1996; Nicklas, 1983), magnetic beads (Smith *et al.*, 1992), optical traps and tweezers (Ashkin, 1997; Ashkin *et al.*, 1987; Svoboda and Block, 1994), vesicle micropipettes (also called the Biomembrane Force Probe (BFP), Evans *et al.*, 1991) and the surface-force apparatus (SFA, Israelachvili, 1991). Figure 2-1 gives an overview of the ranges of forces accessible to these techniques.

The AFM has many similarities with other force-probe techniques. It is possible to consider the AFM and the microfiber technique as a miniature SFA as all of those measure forces via the deflection of a mechanical spring as a function of the separation of two structures. An important advantage of the AFM is that it uses a sharp probe (Chapter 1.1.1) compared to the SFA, which probes the adhesion between macroscopic surfaces with an radius of curvature of ≈ 1 cm. Thus the AFM is particularly well suited to manipulate single-molecules. Another similarity between the different force probe techniques is their time resolution, which gives the time of the fastest transient effect that can be detected. For most of the techniques shown in Figure 2-1 the time resolution is determined by mechanical resonance frequencies and is of the order of a few milliseconds (ms).

---

[2] Here, I will only cover force measurements using a quasi-static cantilever; oscillatory techniques will be left until Chapter 5.

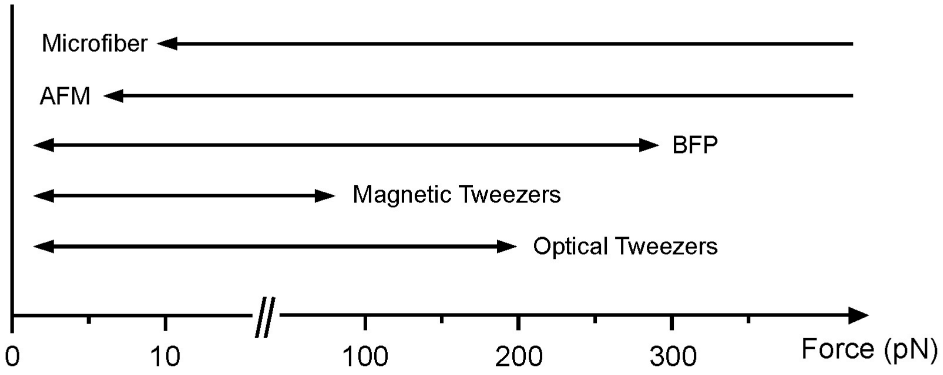

Figure 2-1 Different force probe techniques and their accessible range of forces. The force resolution of the AFM (and microfibers) is ≈ 10 pN (Chapter 2.3). The BFP, optical and magnetic tweezers are capable of detecting forces down to one pN but are limited to maximal forces of a few hundred pN. The SFA has a force resolution of ≈ 10 nN and thus is not shown here. The data for this figure were taken from Leckband *et al.* (Leckband and Israelachvili, 2001) and Florin *et al.* (Florin *et al.*, 1995).

A large and increasing focus of these force probe techniques is the measurement of the molecular interactions determining the mechanics of single biological macromolecules, such as polysaccharides, nucleic acids, proteins, or ligand-receptor pairs. In initial experiments in 1994, Lee *et al.* (Lee *et al.*, 1994) studied the intramolecular properties of complementary strands of DNA and Moy *et al.* measured the rupture force of single receptor-ligand bonds (Moy *et al.*, 1994). Only a few years later, Rief *et al.* observed a force-induced conformational transition within a single polysaccharide molecule (Rief *et al.*, 1997). At the same time, Mitsui *et al.* and Rief *et al.* demonstrated the reversible unfolding of single proteins using the AFM (Mitsui *et al.*, 1996; Rief *et al.*, 1997). Such mechanical unfolding experiments revealed for the first time a direct correlation between folding pattern and mechanical function (Oberhauser *et al.*, 1998; Rief *et al.*, 1998). In the meantime, forced unfolding experiments have not only addressed proteins with bio-mechanical functions (e.g. immunoglobulin and fibronectin (Li *et al.*, 2005; Marszalek *et al.*, 1999; Rief *et al.*, 1997; Rief *et al.*, 1998; Williams *et al.*, 2003), tenascin

(Oberhauser *et al.*, 1998), or spectrin (Law *et al.*, 2004; Law *et al.*, 2003)), but also enzymes or parts thereof (e.g. barnase (Best *et al.*, 2001) or E2lip3 (Brockwell *et al.*, 2003)), ubiquitin (Carrion-Vazquez *et al.*, 2003), and even the green fluorescent protein (Dietz and Rief, 2004).

2.2 Force-distance measurements

The principle of force spectroscopy lies in the measurement of the distance dependence of the interaction force between two structures which equals the derivative of their interaction energy with respect to their distance. In case of the AFM, force-distance (F-D) measurements are achieved in approach-retract cycles where the sample is linearly moved towards and away from the cantilever. Plotting the deflection of the cantilever as a function of sample position yields a characteristic F-D curve (Figure 2-2). Initially, the tip is far away from the surface and, as there is no tip-sample interaction, the cantilever is not deflected (Figure 2-2 A, frame a). Consequently the deflection of the free cantilever recorded far away from the surface defines the zero-force baseline (Figure 2-2 A, dashed line). As soon as the sample comes close to the tip surface forces cause the cantilever to bend towards the surface (in case of attractive interactions) or away from the surface (in case of repulsion). If the gradient of the attractive interaction force between tip and surface is greater than the spring constant of the cantilever, a jump to contact (also called snap-in) is observed (Figure 2-2 A, frame b). In a typical experiment, this instability is often encountered between two clean surfaces, e.g. a silicon nitride tip and a mica surface, due to attractive van der Waals interactions. As the approach continues, cantilever and surface come into hard contact (Figure 2-2 A, frames b and c) and the motion of the piezo-electrical element is directly monitored in the deflection of the cantilever. From this gradient the optical sensitivity of the cantilever, $\square$, is inferred[3]. The optical sensitivity is required to convert the voltage signal from the photodiode, x_V, to metric cantilever deflection, x, using the relationship

$$x = \frac{x_V}{\square} \qquad 2.1$$

---

[3] One should note that for the fundamental mode the optical sensitivity of a freely moving cantilever is lower than that of a simply supported cantilever by a factor of 0.92 (Butt and Jaschke, 1995; Walters *et al.*, 1996). Also, the optical sensitivity should be calibrated on a hard and clean surface in the same range of deflection voltages where the experiments will be performed.

Thus calibration of the optical sensitivity by pressing the cantilever on a hard surface is an important prerequisite for quantitative force measurements and error signal images. The intersection between the zero force baseline and the hard contact area is used to define the contact point (Figure 2-2 A, circle). At this point an undeflected cantilever would touch the surface and the separation between tip and sample is defined to be zero (see below).

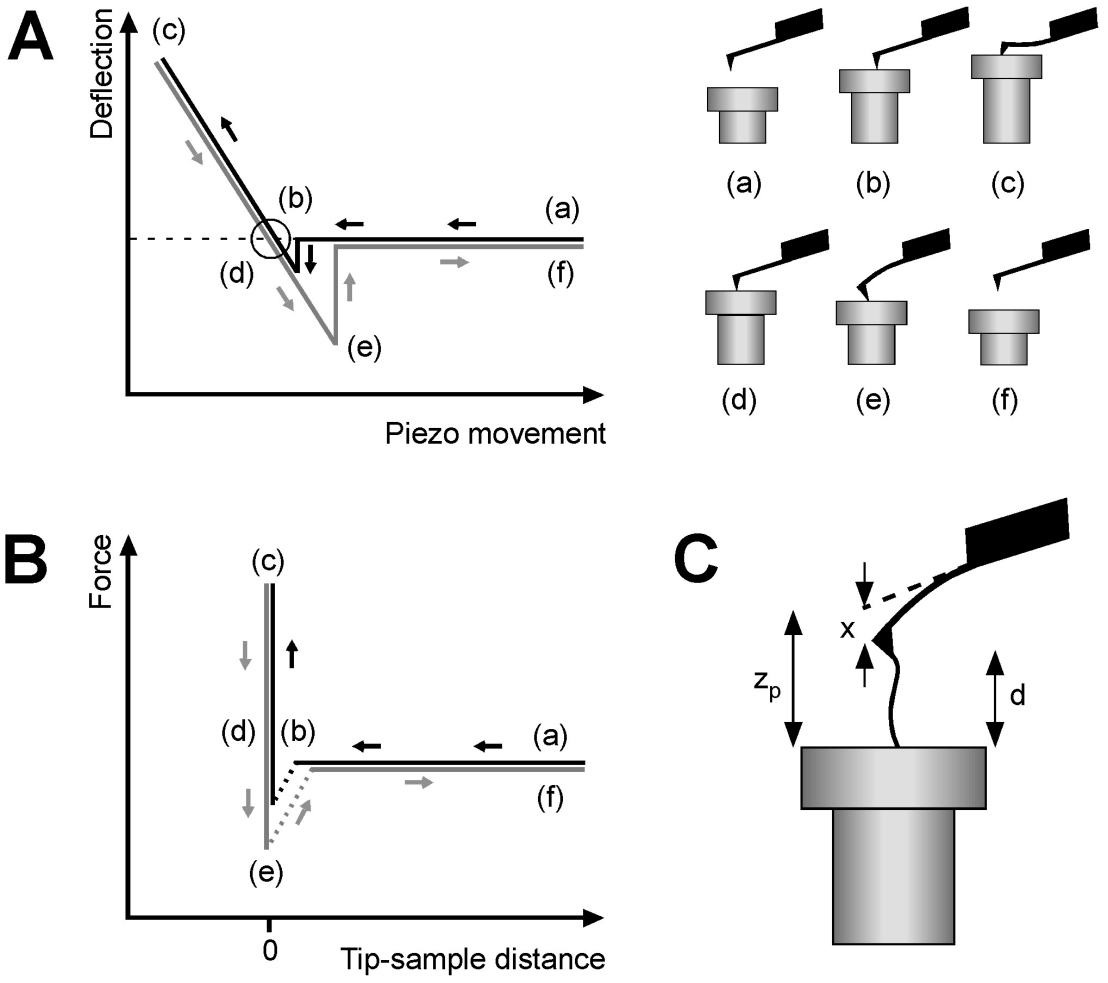

Figure 2-2 F-D measurement in the AFM. (A) An unprocessed approach-retract curve plotted as deflection against piezo movement (left) and schematics of the corresponding steps during the approach-retract cycle (right). Initially, the cantilever is away from the surface (frame a) but at some point the tip and sample come in contact (frames b and c). As the piezo-electrical element retracts again (frames c and d) adhesion can occur due to specific or non-specific interactions between the tip and the surface (frame e). Typically the cycle stops at the same point where it started (frame f). (B) The same F-D curve plotted as force against tip-sample distance. The dotted segments of the curve only connect two data points and therefore should be omitted during analysis. (C) Schematics of a cantilever deflected by a molecular bridge illustrating how the tip-sample distance is calculated.

After the piezo-electrical element has moved a certain distance or the cantilever reaches a certain deflection, the approach is finished and the piezoelectric stage begins to retract (Figure 2-2 A, frames c and d). Visco-elastic deformation of a soft surface and drag can lead to hysteresis and the F-D curve recorded during surface approach differs from that recorded during surface retract[4]. As the tip is separated from the surface adhesion can be observed, e.g. due to surface effects or when a molecule bridges the tip and the surface. During adhesion, the deflection drops below the baseline before tip-sample contact is disrupted (Figure 2-2 A, frame e). An ideal F-D curve cycle starts and ends at the same point (Figure 2-2 A, frames a and f).

In most cases, the relation of interest is the force, F, as a function of the tip-surface distance, d (Figure 2-2 B). According to Hooke's Law, the force is directly related to the deflection and the spring constant of the cantilever, k_c, according to

$$F = k_c x \qquad 2.2$$

As illustrated in Figure 2-2 C, the tip-sample distance takes the deflection of the cantilever into account and is calculated by subtracting the metric cantilever deflection from the piezo movement, z_P, following

$$d = z_P - x \qquad 2.3$$

From the next chapters it will become clear that the tip-sample distance provides a more meaningful measure for the extension of single molecules compared to the piezo displacement, particularly if soft cantilever were used.

2.3 Force sensitivity

For AFM force measurements at room temperature, the dominant source of noise is the thermal excitation of the cantilever. In a first approximation, the smallest detectable force can be estimated using the equipartition theorem (Landau and Lifshitz, 1980). As each degree of freedom of a thermodynamic system is assigned 1/2 $k_B T$ thermal energy (k_B is the Boltzmann constant, T the absolute temperature), each eigenmode of the cantilever is thermally excited by the same amount of energy (Sarid, 1994). However, in the case of the AFM cantilever higher order eigenmodes have much higher force constants as the first eigenmode and do not significantly contribute to the deflection at the end of the cantilever (Hutter and Bechhoefer, 1994; Meyer and Amer, 1988; Sarid, 1994). Consequently the time-averaged deflection of the thermally excited cantilever is related to the energy stored by the system following

---

[4] When in contact with a soft sample the tip can indent into the surface. The indentation as a function of the applied force gives insights into the visco-elastic properties of soft samples, such as cells or surfaces coated with polymers (e.g., see Benmouna and Johannsmann, 2004; Radmacher *et al.*, 1992).

$$\frac{1}{2}k_BT = \frac{1}{2}k_c\left|x^2\right| \tag{2.4}$$

where $\left|x^2\right|$ is the time averaged mean-square displacement. Equating the thermal time-averaged root-mean-square (RMS) displacement to the minimum detectable deflection allows the smallest detectable force, F_{min}, to be estimated as

$$F_{\min} = \sqrt{k_BTk_c} \tag{2.5}$$

In this first approximation, the force sensitivity is only related to thermal energy and the spring constant and can be improved by choosing a softer cantilever. According to Equation 2.5, a typical cantilever used for force spectroscopy (k_c = 10 pN/nm) has a smallest detectable force of ≈ 6.4 pN at a temperature of 300 K.

In a more elaborate description the measurement bandwidth and viscous damping of the cantilever is considered. Within the context of the fluctuation-dissipation theorem (Landau and Lifshitz, 1980; Sarid, 1994), the thermal RMS force noise, F_{RMS}, is given by

$$F_{RMS} = \sqrt{\frac{4k_BTBk_c}{\omega_0Q}} \tag{2.6}$$

where B is the measurement bandwidth, ω_0 the angular resonance frequency and Q the quality (Q-) factor (also see Chapter 5.2.1). For quasi-static force measurements, we are typically interested in the cantilever's response at relatively low frequencies of a few kHz. Assuming that a measurement was made with 2 kHz bandwidth, at a temperature of 300 K, using a cantilever with a spring constant of 10 pN/nm, a Q-factor of 1, and a resonant frequency of 1 kHz, the above equation yields a thermal RMS force noise of 7.3 pN with a thermal RMS displacement of 0.73 nm. Equation 2.6 also illustrates that smaller cantilevers with higher resonance frequencies will have smaller apparent force noise for a given spring constant and bandwidth (Viani *et al.*, 1999).

As already mentioned above, it is desirable that the deflection of the cantilever is limited by the thermal motion rather than by the electronic, optical, or vibrational noise of the instrument. Most commercial AFMs available today offer such thermally limited noise measurements. It is easy to validate the performance of the instrument by either measuring the RMS noise of the deflection signal and comparing it to the predicted value obtained from Equation 2.6 or by inspecting amplitude spectra (Chapter 5.2.1). One should note that these theoretical considerations apply to estimate the detection limit of short force pulses. Remarkably, Marshall *et al.* showed that much smaller forces can be resolved if they exist for time periods of the order of a few hundred ms (Marshall *et al.*, 2003). In addition, the laboratories of T. Yanagida and Z.F. Shao demonstrated that external dissipative forces can be used to conduct AFM force measurements with sub-pN force noise (Liang *et al.*, 2000; Tokunaga *et al.*, 1997).

2.4 Spring constant calibration

Accurate knowledge of the spring constant of the AFM cantilever is a prerequisite for quantitative force measurements. Spring constant calibration is especially important as the spring constants of commercially available cantilevers can vary up to 50% from the nominal values supplied by the manufacturer (Hodges, 2002; Tortonese, 1997). The most prominent reason for such large variations lies in the cantilever thickness, which is difficult to control during the manufacturing process. As the spring constant depends on the third power of the thickness (Walters *et al.*, 1996) even cantilevers from the same wafer can have very different spring constants (e.g., see Maeda and Senden, 2000). About a dozen methods have been developed to determine the spring constant of AFM cantilevers, many of which are addressed in a recent review (Hodges, 2002). Here I will introduce the two most commonly applied approaches, thermal fluctuation analysis and the added mass method.

The most popular method for calibrating the spring constant of an AFM cantilever is thermal fluctuation analysis (Butt and Jaschke, 1995; Florin *et al.*, 1995; Hutter and Bechhoefer, 1994). As already mentioned in Chapter 2.3, the equipartition theorem assigns an energy of 1/2 $k_B T$ to each eigenmode of the cantilever. Thus the time-averaged thermal oscillation amplitude can be related to the spring constant of the cantilever following Equation 2.4. To separate the thermal excitation from other sources of noise, the data analysis is performed in the frequency domain (also see Chapter 5.2.1). Parseval's theorem (Landau and Lifshitz, 1980; Sarid, 1994) states that the integral of the power spectral density (PSD), $\left|X(\square)^2\right|$, equals the time domain integral of $\left|x(t)^2\right|$ according to

$$\int \left| x(t)^2 \right| dt = \int \left| X(\omega)^2 \right| d\omega \qquad 2.7$$

Since the main contribution to the power spectra near the resonant frequency originates from the thermal excitation, other sources of noise can be excluded by restricting the integral to the resonance peak. Using Equations 2.4 and 2.7 the spring constant of cantilevers can be calculated in both air (Hutter and Bechhoefer, 1994) and liquid (Florin *et al.*, 1995).

In the added mass method introduced by Cleveland *et al.* in 1993, the cantilever is assumed to have harmonic behavior (Cleveland *et al.*, 1993; also see Chapter 5.2.1). Hence the resonance frequency of the cantilever in the absence of damping is given by

$$\omega_0 = \sqrt{\frac{k_c}{m_c}} \qquad 2.8$$

where m_c is the effective mass of the cantilever. It was demonstrated that the effective mass (and thus the resonant frequency) of the cantilever can be altered by a small tungsten sphere glued to the tip of the cantilever. Following Equation 2.6 and by correcting for the exact position of the mass the spring constant of the cantilever can then be determined. The exact mass of the sphere is estimated from its diameter determined by scanning electron microscopy and the known density.

In apparent contrast to thermal fluctuation analysis, the added mass method is destructive and can thus only be applied to the cantilever after the experiment. On the other hand, thermal fluctuation analysis is associated with an error of at least ±10%. In addition, thermally calibrated spring constants typically only agree to those determined with other methods with an error of about ±20% (Hodges, 2002; Walters *et al.*, 1996). Recently Proksch *et al.* measured the spring constant as a function of the position of the laser spot along the length of the cantilever using thermal fluctuation analysis (Proksch *et al.*, 2004). The observed systematic variation in the spring constant ranged from ≈15% for short to ≈50% for long cantilevers. By using a model that accounts for the spot diameter and position on the cantilever, the thermally measured spring constants were brought into better than 10% agreement with the other methods.

2.5 Polymer extension models

An interpretation of molecular manipulation experiments requires an understanding of the mechanical behavior of single molecules in response to applied forces. Biological macromolecules of many different classes, such as proteins, polysaccharides or nucleic acids, are of polymeric nature. As a consequence, the mechanical extension of these molecules causes enthalpic and entropic restoring forces, which determine their force-extension pattern (Austin *et al.*, 1997; Treolar, 1975). Entropic contributions dominate at small extensions and are due to permanent fluctuations of the molecule caused by Brownian motion. As the molecule is extended the number of accessible states, and thus the conformational entropy, is reduced resulting in the entropic elasticity. In contrast, the enthalpic elasticity dominates at larger extensions and originates from tensions in the backbone (e.g. the stretching of bonds) in the direction of the applied force. Statistical mechanics have been applied to develop a number of different models to predict enthalpic and entropic restoring forces. In the following, I will introduce the two most important polymer extension models, the Freely Jointed Chain (FJC) and the Worm Like Chain (WLC) model, as they have been applied for the analysis of F-D curves in the following chapters.

In the FJC model (Lee *et al.*, 1994) the polymer is divided into rigid elements connected by flexible joints (Figure 2-3 A). These elements have the same Kuhn length, l_k, and are assumed to act independently of each other without long range interactions. The extension of a FJC as a function of the applied force can described as (Lee *et al.*, 1994)

$$d(F) = L_c\left[\coth\left(\frac{Fl_k}{k_BT}\right) - \frac{k_BT}{Fl_k}\right] = L_c L\left[\frac{Fl_k}{k_BT}\right] \qquad 2.9$$

where n is the number of elements, L_c the contour length (L_c=nl_k), and L is the Langevin function. Since the FJC only considers entropic effects the extended FJC (FJC*) model was developed, which takes the deformation of bonds and bond angles into account. In the FJC*, the polymer is described as a chain of identical springs (Figure 2-3 B). The extension of the molecule as a function of the applied force can be written as (Smith *et al.*, 1996)

$$d(F) = L_c L\left[\left(\frac{Fl_k}{k_BT}\right)\left(1 + \frac{F}{\square L_c}\right)\right] \qquad 2.10$$

where □ is the elasticity of the polymer chain. In contrast to the FJC model, which yields an infinite stiffness at the contour length, a chain described with the FJC* model can be extended beyond its contour length. For large extensions the additional enthalpic term in Equation 2.10 gives rise to a linear increase. Examples for the successful application of the FJC and the FJC* model are polymers and polysaccharides (e.g., see Ortiz and Hadziioannou, 1999; Rief *et al.*, 1997; Senden *et al.*, 1998, also see Chapter 2.6).

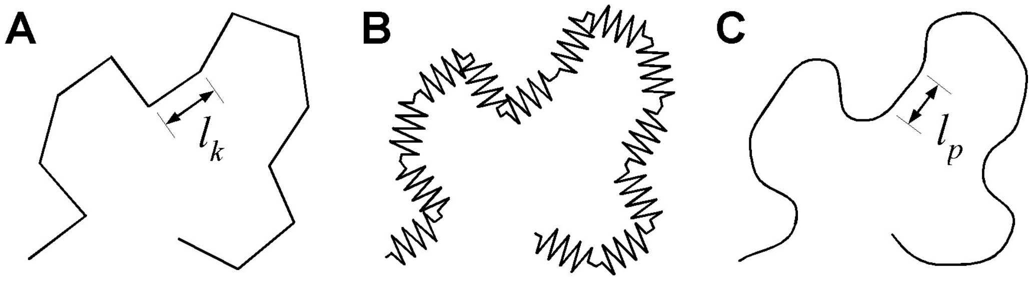

Figure 2-3 Schematic representation of the FJC, FJC* and the WLC model. (A) The FJC consists of independent but rigid segments, which are linked by flexible joints. (B) In the FJC* model, the rigid segments are replaced by springs in order to include enthalpic effects. (C) The WLC model describes a polymer as a curved filament, which is assumed to be linear on the scale of the persistence length. The introduction of a stiffness term yields the WLC* model with an elastic backbone (not shown).

The WLC model of Kratky and Porod describes a polymer as a homogenous string or a continuous curve of constant bending elasticity (Figure 2-3 C; Kratky and Porod, 1949). The following approximation of the F-D relationship for a WLC is accurate for forces up to several hundred pN (Bustamante *et al.*, 1994; Marko and Siggia, 1995)

$$F(d) = \frac{k_B T}{l_p}\left[\frac{1}{4}\left(1 - \frac{d}{L_c}\right)^{-2} - \frac{1}{4} + \frac{d}{L_c}\right] \qquad 2.11$$

Here, the persistence length, l_p, represents the flexibility of the molecule and describes the distance over which the orientation of the chain is lost (Smith *et al.*, 1992). Typically, the persistence length (as well as the Kuhn length) is a free parameter and must be experimentally determined. The WLC model with a persistence length of 4 Å has been successfully applied to describe the extension of unfolded peptides under applied forces larger than 50 pN (Oesterhelt *et al.*, 2000; Rief *et al.*, 1997). Although the WLC model contains bending elasticity, the polymer cannot be extended past its contour length (Baumann *et al.*, 1997). Chain stiffness is added by introducing a linear elasticity term, S, as a second free parameter. This parameter has the unit of force and is related to the spring constant of the chain according to $S=\square L_c$. The F-D relationship following to this extended WLC (WLC*) model can be written as

$$F(d)=\frac{k_B T}{l_p}\left[\frac{1}{4}\left(1-\frac{d}{L_c}+\frac{F}{S}\right)^{-2}-\frac{1}{4}-\frac{F}{S}+\frac{d}{L_c}\right] \qquad 2.12$$

and was successfully applied to describe the behavior of DNA under high forces (Wang *et al.*, 1997).

The models discussed above are largely independent of the molecular composition and no straightforward relation between the model parameters (l_p, l_k, $\square$, S) and real structural quantities such as bond length or the contour length can be found. However, e.g. in the case of the polysaccharide dextran the Kuhn length (≈ 5 Å) and the length of a monomer (≈ 4 Å) are rather close (Rief *et al.*, 1997; also see Chapter 2.6). Finally one should note that the persistence and Kuhn lengths not only depend on the magnitude of the applied force but also on the surrounding medium (e.g. polarity or ion strength) as they are linked to the molecular structure of the polymer.

2.6 Force spectroscopy model systems

2.6.1 Abstract

In the following, I will present force spectroscopy experiments on the polysaccharide dextran and a multi-domain protein consisting of 8 Immunoglobulin 27 domains (Ig27-8) since these two molecules are the most prominent model systems for single-molecule force spectroscopy. The multi-domain protein will also serve as a model system to study hydrodynamic effects in Chapter 4. The results presented in this chapter agree very well with previous experiments performed by a number of other groups and illustrate the application of the polymer extension models from the last chapter.

2.6.2 Experimental procedures

Sample preparation

The Ig27-8 sample was a kind gift of Julio Fernandez (Columbia University, New York, NY, USA). 2µl of Ig27-8 (concentration ≈ 100 µg/ml) were added to a drop of PBS buffer (Sigma) on a freshly gold-coated glass coverslip (SCD050 Sputter

Coater, Baltec, Tucson, AZ, USA). After 10 minutes, the sample was rinsed ten times with PBS. Dextran (average molecular weight 2 MDalton) was purchased from Sigma. 200 μl of a 5% w/w dextran solution in nanopure water were allowed to dry in air on glass coverslips at 37°C. Samples were then rinsed for 1 minute under a flow of nanopure water.

AFM Instrumentation

A commercial AFM (Picoforce, Digital Instruments, Veeco Metrology, Santa Barbara, CA, USA) was equipped with a X-Y-Z-piezo scanner with a closed-loop 20 μm Z-axis (for more details also see Chapter 3.3). The spring constants of the V-shaped silicon nitride cantilevers (short thin-legged NP-S: k_c ≈ 0.31 N/m, ν_{res} ≈ 10 kHz, length (l) ≈ 115 μm, width (w) ≈ 25 μm, thickness (t) ≈ 0.4 μm; Microlever MSCT-AUNM-C: k_c ≈ 0.015 N/m, ν_{res} ≈ 1 kHz, l ≈ 320 μm, w ≈ 22 μm, t ≈ 0.6 μm; di-Veeco) were calibrated in liquid using thermal fluctuation analysis (Chapter 2.4). Experiments on Ig27-8 (dextran) were performed using the large cantilever in PBS (the short cantilever in 150 mM KCl, 10 mM Tris, pH 7.8) at 1310 nm/s pulling speed and contact forces (times) of 0.5 – 1 nN (0.5 – 3 s).

2.6.3 Results and discussion

In 1997 Rief *et al.* applied force spectroscopy to single molecules of the polysaccharide dextran, which consists of α-1,6-linked D-glucopyranose residues (Rief *et al.*, 1997). Since then dextran became a very important model system for force spectroscopy because dextran samples are easily prepared on glass surfaces and F-D curves of single dextran molecules can routinely be recorded. The F-D curve in Figure 2-4 A displays the typical force-extension pattern of a single dextran molecule. The pattern is characterized by a plateau that was attributed to a conformational transition of the glucopyranose rings (Marszalek *et al.*, 1998; Rief *et al.*, 1997). At small extensions (here ≤ 180 nm), almost all pyranose rings are in the chair conformation and an increase in force is measured due to entropic stretching of the polysaccharide chain. As soon as the applied force reaches ~ 1 nN, the pyranose rings undergo the chair-boat transition, which elongates the chain by ~18% and appears as a plateau-like region in the F-D curve (Marszalek *et al.*, 1998; Rief *et al.*, 1997). After most of the pyranose rings have assumed the boat conformation, an increase in force is detected prior to the detachment of the molecule from the tip. Overlaid on the F-D curve is the fitting with the FJC* model (Equation 2.10) with a

Kuhn length of 0.50 and 0.55 nm and a segment elasticity of 11.5 and 25.3 Nm^{-1} before and after the force plateau[5]. These values are in good agreement with the recent literature, where Kuhn lengths of 0.44 and 0.57 nm before and after the force plateau and different segment elasticities between 8 and 40 Nm^{-1} have been reported (Marszalek *et al.*, 1998; Rief *et al.*, 1997). From Figure 2-4 B it becomes clear that dextran curves have different lengths due to the random attachment points on the adsorbed molecules. To assure that the F-D curves originate from single molecules they have to be normalized. This is either achieved using the contour length determined from the fitting or by setting the extension at a certain force to an arbitrary value (Janshoff *et al.*, 2000; Rief *et al.*, 1997).

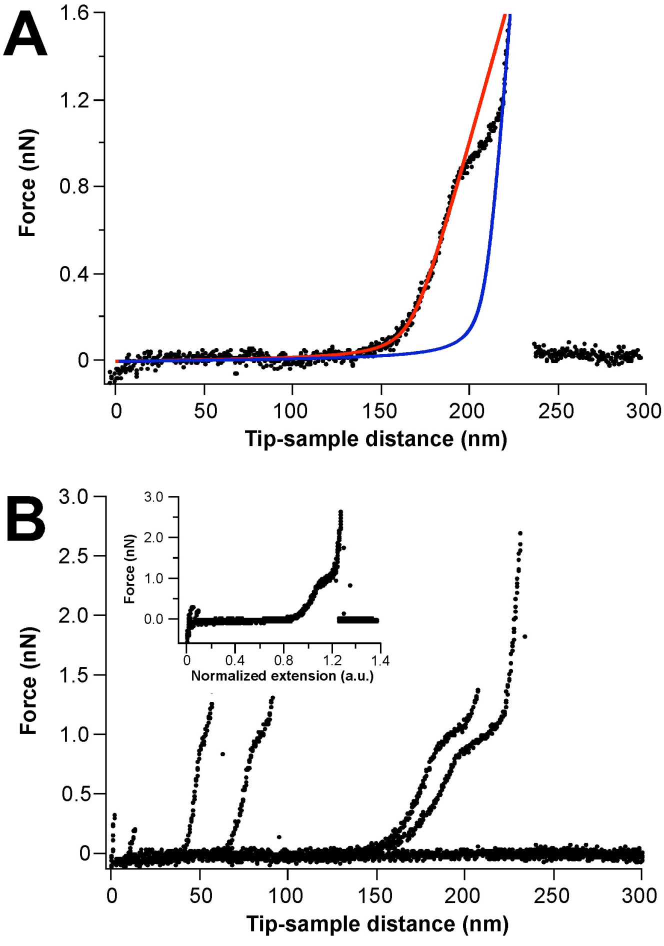

Figure 2-4 Force spectroscopy of the polysaccharide dextran. (A) Typical F-D curve recorded on a single dextran molecule displaying the chair-boat transition of the pyranose ring. The curve is well described using the FJC* model before (red line) and after the transition (blue line) with a Kuhn length of 0.50 and 0.55 nm and segment elasticity of 11.5 and 25.3 Nm^{-1}. (B) Due to the random point of attachment individual F-D curves had different lengths. The shown curves were normalized by setting the extension at 500 pN to 1 (inset). The common pattern of the curves is now clearly visible.

In addition to the detection of a reproducible pattern, there is another simple criteria to identify unfolding spectra originating from the manipulation of single molecules. An adhesion frequency of <20% implies that nearly 90% of the events originate from single molecule interactions (Williams and Evans, 2002). A higher adhesion frequency increases the probability that events originate from multiple molecules or indicates contamination of the AFM tip.

---

[5] To fit the experimental F-D curves with Equations 2.9 the extension was plotted as a function of force.

Later in 1997, Rief *et al.* presented first results on the force induced reversible unfolding and refolding of single proteins (Rief *et al.*, 1997). In contrast to the pioneering experiments presented by Mitsui *et al.* one year earlier (Mitsui *et al.*, 1996), Rief *et al.* only studied long multi-domain fragments of the giant muscle protein titin. Titin consists of long repeats of water-soluble immunoglobulin and tenascin domains and is responsible for the assembly of thick muscle filaments, muscle elasticity and the generation of passive tension (for a recent review, see Tskhovrebova and Trinick, 2003). The multi-domain constructs of titin not only provided a predictable pattern to identify the F-D curves but were also required to collect reliable unfolding data[6]. In their study, Rief *et al.* took advantage of genetic engineering to produce multi-domain proteins, which, in contrast to native fragments, consist of identical domains. In a typical experiment, multi-domain proteins were firstly adsorbed to a freshly prepared gold surface. Separating the tip from the sample resulted in the extension of the protein and the application of a gradually increasing pulling force. As a consequence of this external pulling force the protein domains subsequently unfolded. Consequently the F-D curve exhibited a saw-tooth pattern, which originated from the sequential unfolding of the domains and the stretching of the already unfolded polypeptide elements (Figure 2-5).

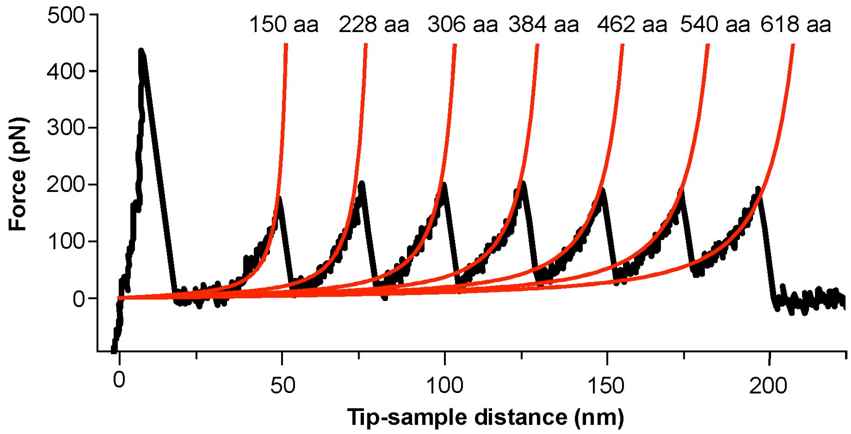

Figure 2-5 Mechanical unfolding of a multi-domain protein. A multi-domain protein consisting of 8 Ig27 domains from titin is unfolded using force spectroscopy. An increasing force is detected when stretching the protein until a single domain unfolds and the cantilever relaxes to the zero-force baseline. Unfolding of domains increases the length of the stretched polypeptide by 28 nm (78 aa). The unfolding of the first domain is not resolved, most probably due to non-specific surface interactions.

---

[6] At at small tip-sample distances (< 15 nm), unspecific tip-surface interactions are experienced, which prevent resolving the unfolding of short proteins. Thus multi-domain proteins are also used as “hosts” for proteins, which typically do not occur in multimers (Brockwell *et al.*, 2003; Dietz and Rief, 2004).

The force-extension relationship of unfolded parts of the protein in the F-D curve is well described using the WLC model with a persistence length of 4 Å and a monomer length of 3.6 Å. As expected, the peaks in the F-D curves were separated by the length of an unfolded domain and the contour length was incremented by 28 nm between the peaks. The force that unfolds each domain was revealed from the height of the peaks and an average unfolding force of 195 ± 23 pN was measured at a pulling speed of 1.31 μm/s.

2.7 Conclusions

Inter- and intramolecular forces determine the structures, dynamics, and functions of biological macromolecules and thus regulate all fundamental processes in life. Currently, molecular interactions are typically inferred indirectly from equilibrium binding and kinetic measurements (e.g., see Jelesarov and Bosshard, 1999) or are calculated using molecular models (Mulholland and Karplus, 1996; Schnell and Turner, 2004). With the recent development of single-molecule force spectroscopy, such inter- and intramolecular interactions of biological macromolecules became directly accessible (Janshoff *et al.*, 2000; Leckband and Israelachvili, 2001). Since the AFM allows measuring forces with a resolution of a few pN (Chapter 2.3), the interactions controlling the mechanics or adhesion of single molecules or the stability of single proteins can now be studied.

I have presented two force spectroscopy experiments that examine the mechanical properties of individual molecules (Chapter 2.6). In both cases excellent agreement with results reported by other groups is observed. The first experiment has revealed conformational transitions in single polysaccharide molecules. In the second experiment the external force played the role of the denaturant and lead to sequential unfolding of the three-dimensional structure of individual proteins. As explained in more detail in the next chapter, this type of experiment addresses the off-equilibrium stability of single proteins and is thus fundamentally different from thermal and chemical denaturation experiments where the average unfolding of large numbers of molecules are investigated.

3. Mechanical stability of single bacteriorhodopsins

3.1 Introduction

The folding and stability of proteins has been in the center of biophysical research since the pioneering work of C.B. Anfinsen (Anfinsen, 1973). However, most folding and unfolding studies have focused on small water-soluble proteins mainly because membrane proteins are considerably more difficult to work with and cannot be denatured to a fully unfolded state (Chapter 1.2.2). In addition, it is well-recognized that the bulk experimental methods applied to unfold membrane proteins only probe the average behavior of a large number of molecules and cannot resolve simultaneously occurring multiple (un-)folding pathways or non-accumulative (un-)folding intermediates. Thus it is not surprising that only limited experimental information about the stability of membrane proteins exist, also if compared to the wealth of data available for water-soluble proteins.

The force spectroscopy experiments presented in Chapter 2 provide a novel approach to reveal detailed insights into the molecular interactions determining the stability of proteins. Additionally, a modified form of force spectroscopy called dynamic force spectroscopy (DFS) probes the complex energy landscapes underlying the mechanical response of receptor ligand-pairs and single proteins (for a recent review, see Evans, 2001). As I will explain in more detail in Chapter 3.2.2, monitoring the unfolding force as a function of pulling speed allows detecting the energy barriers crossed during the unfolding process. Additionally, the natural transition rates over these barriers can be determined to give a previously inaccessible measure for protein stability. In the following, I present my results on the application of force spectroscopy and DFS to study the stability of the membrane protein BR.

3.2 Theoretical considerations

3.2.1 Sample preparation

An important prerequisite for the imaging and manipulation of biological specimens is the immobilization of the sample on a solid support. In the following, I will describe the adsorption procedure applied to prepare BR samples. The procedure is based on physical interactions between the sample and the surface and was shown to be applicable to a variety of different classes of biological macromolecules (Ellis *et al.*, 2004; Müller *et al.*, 1997).

Care has to be taken when choosing a supporting surface for AFM since it should be very flat and chemically inert to prevent unspecific reactions with the sample. The most commonly used AFM support for biological specimens are mica minerals, which are characterized by their layered crystal structure and their relative chemical inertness (Bailey, 1984). Muscovite mica is the most commonly used form where tetrahedral sheets of $(Si,Al)_2O_5$ are ionically linked by a central layer of $Al_2(OH)_2$. The net negative charge of the basal oxygen between these layers is balanced by hexagonally coordinated cations (K+ in muscovite, Na+ in paragonite mica). This layer is disrupted by simple cleavage procedures (e.g. by pulling apart with scotch tape). The resultant basal plane is negatively charged and provides clean and atomic flat surfaces over several hundreds of μm^2. The average surface charge density of muscovite mica in water is $\sigma_S \approx -0.0025\ Cm^{-2}$ or 0.015 electron per surface unit cell (Pashley, 1981; Pashley, 1981).

Biological samples can be immobilized to surfaces either by physical adsorption or by covalent binding (for a review, see Müller *et al.*, 1997). Here, I have used the physisorption approach because of its simplicity and versatility. The major physical interaction that drives the adsorption of bio-molecules from solutions to surfaces is the Derjaguin-Landau-Verwey-Overbeek (DLVO) force, which describes the interplay of attractive van der Waals and repulsive EDL forces (Israelachvili, 1991). In order to firmly bind molecules to mica, the net DLVO force between the two surfaces must be attractive. This is achieved by reducing the repulsive EDL force, which strongly depends on the concentration and valency of charged solutes. The origin of the EDL force lies in the fact that most surfaces exposed to an aqueous solution are charged and attract counter ions. This results in a charge cloud at the solid-liquid interface, which is balanced by the counter ions in the so-called EDL. If two equally charged surfaces with small surface potentials are brought together the EDLs overlap, resulting in a repulsive EDL force (per unit area), F_{el}, according to

$$F_{el}(D) = \frac{2\sigma_s\sigma_p}{\varepsilon_e\varepsilon_0} e^{-\frac{D}{\lambda_D}} \qquad 3.1$$

Equation 3.1 is valid for two planar surfaces where D is the distance between the surfaces, ε_0 the dielectric permittivity of free space, ε_e the relative dielectric permittivity of the electrolyte (≈ 80 for aqueous buffers), and σ_s and σ_p represent the surface charge density of the support and the proteins ($\sigma_p \approx -0.05$ Cm^{-2} for PM). The Debye length λ_D describes the thickness of the EDL and can be written as

$$\lambda_D = \frac{0.304}{\sqrt{e_c}} \qquad 3.2$$

or

$$\lambda_D = \frac{0.176}{\sqrt{e_c}} \qquad 3.3$$

for monovalent and divalent electrolytes, respectively (Israelachvili, 1991). From the Equations 3.2 and 3.3, the influence of the ion concentration in the solution, e_c, on the Debye length and thus to the EDL force becomes clear.

According to the Lifshitz theory, the van der Waals force per unit area between two flat surfaces is given by (Israelachvili, 1991)

$$F_{vdW}(D) = \frac{-H_a}{6\pi D^3} \qquad 3.4$$

where the Hamaker constant, H_a, characterizes the interaction of the two surfaces across a third medium ($H_a \approx 10^{-20}$ J for hydrocarbons in water). Thus the overall DLVO force per unit area (the sum of F_{el} and F_{vdW}) can be written as

$$F_{DLVO}(D) = \frac{2\sigma_s\sigma_p}{\varepsilon_e\varepsilon_0} e^{-\frac{D}{\lambda_D}} - \frac{H_a}{6\pi D^3} \qquad 3.5$$

Equation 3.5 can be directly applied to calculate the ion concentration necessary to reach an attractive net force between two surfaces and it suggested that increased adsorption densities can be achieved by increasing the ion concentration (Müller *et al.*, 1997)[7]. For PMs sensible adsorption densities on mica were achieved with salt concentrations between 150 and 300 mM KCl, in agreement with above theoretical considerations.

3.2.2 Relation between unfolding force and stability

In Chapter 2.6 I demonstrated that the AFM is capable of measuring the unfolding forces of single water-soluble proteins. However, unfolding forces are a very anonymous measure for protein stability as they primarily relate to the mechanical strength of the structures. DFS experiments have been developed to understand this relationship between force and stability, where latter is expressed in terms of an equilibrium unfolding rate with units of s^{-1} (Evans and Ritchie, 1997). DFS has already been applied to water-soluble proteins, receptor-ligand bonds, and numerous other non-covalent biological interactions (for a review, see Evans, 2001). In the following, I will introduce the theoretical framework underlying DFS as the technique will later be employed to study single BRs.

---

[7] A different approach to adsorb proteins to surfaces using lower concentrations of monovalent ions and increased protein concentrations was recently suggested (Czajkowsky and Shao, 2003).

In the simplest possible protein (un-)folding model only two energetical states exist. These are the low-energy folded and the high-energy unfolded state (Figure 3-1). In this classical scenario, the folded state is separated from the unfolded state by a single potential barrier located at a distance x_u. In absence of a pulling force, the natural unfolding rate over this barrier, k_u, is given by

$$k_u = \frac{1}{\tau_D} e^{\frac{-\Delta G_u^*}{k_B T}} \qquad 3.6$$

where τ_D is the diffuse relaxation time[8] and $-\Delta G_u^*$ denotes the free energy of activation. Equation 3.6 describes a thermally activated process, which obeys first-order kinetics and follows the theory of overdamped kinetics in liquids developed by H.A. Kramers (Hanggi *et al.*, 1990; Kramers, 1940).

As first shown by G.I. Bell (Bell, 1978) and later in a more elaborate description by E. Evans and K. Ritchie (Evans, 2001; Evans and Ritchie, 1997), the escape over a potential barrier under force occurs within a time range determined by the applied force rate. Since typical non-covalent interactions have finite lifetimes they will fail under any level of force if pulled on for the right length of time. In particular, fast pulling speeds will result in bonds with high rupture forces and short lifetimes, while low pulling speeds will render the rupture forces small and the lifetimes long. For a sharp barrier, the shape and location of transition state are insensitive to force (Evans and Ritchie, 1997), but the height of the energy barrier is lowered according to (Bell, 1978)

$$\Delta G_u^*(F) = \Delta G_u^* - F x_\beta \qquad 3.7$$

Here $x_\beta = x_u \cos\theta$ is the thermally averaged projection of the barrier along the direction of force where the angle θ accounts for deviations of the reaction coordinate from the pulling direction (Evans, 2001; Evans and Ritchie, 1997). Substituting Equation 3.7 into 3.6 gives

---

[8] The diffuse relaxation time, $\tau_D = \gamma_m l_c l_{ts} / (k_B T)$, is governed by the molecular damping, γ_m, and two lengths, which describe the thermal spread of folded states, l_c, and an energy weighted width of the barrier, l_{ts} (Hanggi *et al.*, 1990; Kramers, 1940). For proteins typical values of τ_D are of the order of 10^{-7} - 10^{-9} s (Bieri *et al.*, 1999; Lapidus *et al.*, 2000; Yang and Gruebele, 2003).

$$k_u(F) = \frac{1}{\tau_D} e^{\frac{-(\Delta G_u^* - F x_{\square})}{k_B T}} = k_u e^{\frac{F x_{\square}}{k_B T}} \qquad 3.8$$

and it becomes clear, that the unfolding rate increases exponentially with force on the scale of $\frac{k_B T}{x_{\square}}$.

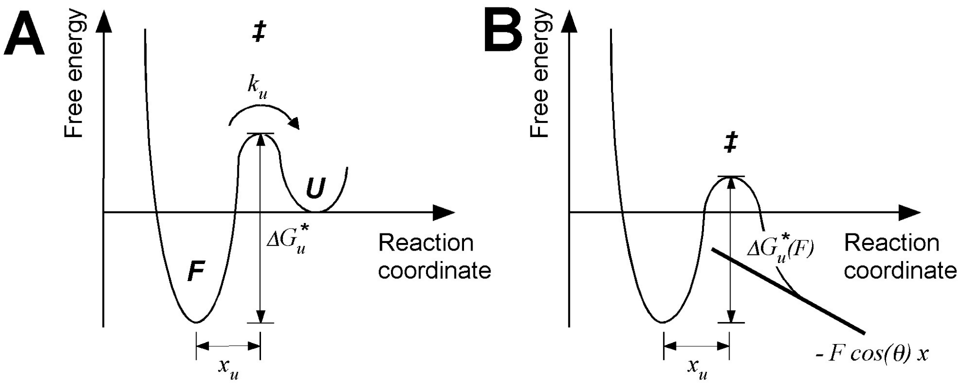

Figure 3-1 Two-state potential for the interpretation of mechanical unfolding experiments. (A) The energy landscape is characterised by a single sharp potential barrier separating the folded state (*F*) from the unfolded state (*U*). The activation energy for unfolding is given by $-\Delta G^*_u$, while x_u (the width of the potential barrier) is the distance along the reaction coordinate from the folded state to the transition state (‡). Extension of the folded state by the width of the potential barrier triggers the unfolding process. (B) Coupled to a projected reaction coordinate, an external force F adds a mechanical potential $-F\cos(\theta)\, x$ that tilts the landscape and lowers the energy barrier according to Equation 3.7.

After considering the effect of force on the energy landscape we need a way to describe the history of force loading on the bond. In the simplest scenario the force is treated as a ramp in time, which increases with a certain force loading rate, r_f, which is defined by

$$r_f = \frac{dF}{dt} \qquad 3.9$$

In fact, such a force ramp is what biomolecular bonds experience when a force probe (e.g. the AFM cantilever) and a sample surface are separated. If the cantilever is softer than the linker between the molecule and the cantilever (or the molecule and the surface) the loading rate is constant and equals the product of the spring constant of the cantilever and the pulling speed. However, in most experimental situations, molecules are connected to the cantilever via a flexible linker, such as polymer spacers for the study of single ligand-receptor pairs or already unfolded domains in case of proteins (Hinterdorfer *et al.*, 2000; Rief *et al.*, 1997). Thus the bond is subjected to non-linear loading, which can be taken into account either by approximating the loading rate from a linear fit to the F-D curve (Figure 3-6) or by applying Monte-Carlo (M-C) simulations (see Chapter 3.2.3)[9].

Importantly, the most probable unfolding force, F^*, is governed by the force loading rate according to (Evans, 2001; Evans and Ritchie, 1997)

$$F^* = \frac{k_B T}{x_\beta} \ln \frac{r_f x_\beta}{k_B T k_u} \qquad 3.10$$

Thus the principle of DFS lies the measurement of the most probable rupture force as a function of the loading rate (Figure 3-2). Fitting a dynamic force spectrum such as the one shown in Figure 3-2 A with Equation 3.10 then explores the energy landscape by determining x_β and k_u.

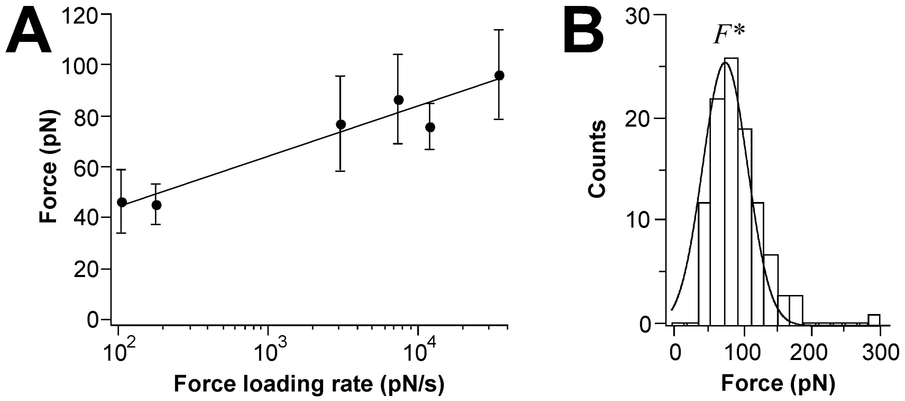

Figure 3-2 The principle of DFS. (A) Unfolding forces are measured as a function of different pulling speeds. For each pulling speed, the loading rate is calculated as shown in Figure 3-6. For a single potential barrier, plotting force against the logarithm of the loading rate yields a single linear regime. The data can be fit using Equation 3.10 (solid line) to reveal x_β and k_u. (B) Force histogram recorded at a loading rate of 3067 pN/s (654 nm/s pulling speed). The histogram is well described by a Gaussian fit centered at the most probable rupture force (here 77.2 ± 3.4 pN). The data shown here were taken from Chapter 3.4 (α-helix D, C3-175).

Evidently the potential shown in Figure 3-1 is an over-simplification as macromolecular complexes (such as receptor-ligand bonds) involve many distributed molecular interactions that create a mountainous terrain of energy barriers (e.g., see Evans *et al.*, 2001; Merkel *et al.*, 1999). Remarkably, plotting the most probable rupture force as a function of the logarithm of the loading rate maps the most prominent barrier transversed in the energy landscape (Figure 3-3). When force is applied, outer barriers are driven below inner barriers, which become the dominant impedance to unbinding. Because of the exponential dependence of kinetic rates on the barrier energies (Equation 3.8), the experimental challenge is to measure forces over many orders of magnitude loading rate[10]. In this way, DFS probes the inner world of molecular interactions and reveals barriers that are difficult or impossible to detect in equilibrium assays but determine the strength and stability of bonds or proteins under rapid detachment or unfolding.

---

[9] In some cases numerical methods were also developed for non-linear loading (Williams and Evans, 2002; Williams *et al.*, 2003).

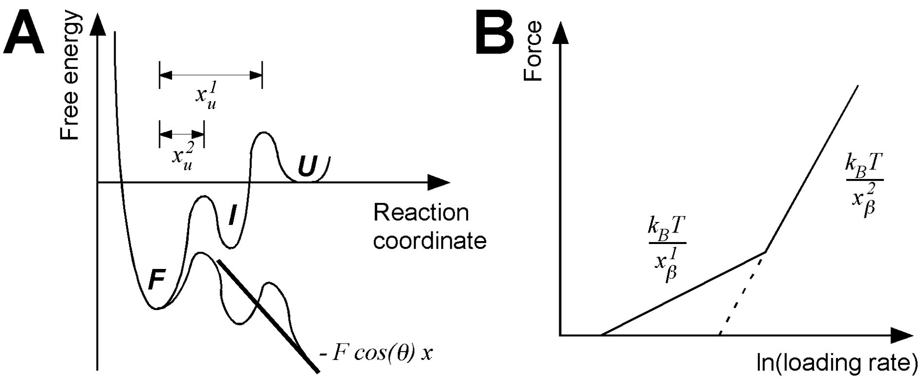

Figure 3-3 Energy landscape with two energy barriers. (A) Force can tilt a three-state energy landscape in such way that the outer barrier is suppressed and the inner barrier determines transition kinetics. (B) The corresponding dynamic force spectrum becomes a piecewise linear spectrum. The abrupt increase in slope results from probing different energy barriers as the slopes correspond to the ratio of the thermal energy and the width of the barriers. Two or more energy barriers have been observed e.g. in the case of the unbinding of biotin to avidin or PSGL-1 to L-selectin (Evans *et al.*, 2001; Merkel *et al.*, 1999).

3.2.3 Monte-Carlo simulations

M-C simulations offer a relatively simple but powerful method to analyze DFS data (Rief *et al.*, 1998). Importantly, MC simulations allow non-linear loading conditions to be taken into account and can also be applied to more complicated systems where several bonds are loaded at the same time (e.g., see Figure 3-4). In a MC simulation, a virtual model of the bond and its linker is stretched at constant pulling speed in an iterative process. The model of the bond is characterized by the width of the potential barrier and the natural transition rate and, in case of protein unfolding experiments, the WLC model is used to describe the F-D relationship of the polypeptide linker. For every iteration, the extension of the molecule, d, is calculated according to

$$d = v * dt \tag{3.11}$$

---

[10] An approach to extend the accessible range of AFM force loading rates is presented in Chapter 4.

where *v* is the pulling speed and dt is time interval assigned to each the iteration. From the extension, the force acting on the bond is the determined using the WLC model (Equation 2.11). To simulate the unfolding kinetics of the folded structure, the applied force is used to compute the loaded unfolding rate according to Equation 3.8. Finally, the unfolding probability, P_u, at each time step is calculated according to

$$P_u(t) = k_u(F) \cdot dt \qquad 3.12$$

and compared with a computer-generated random number between zero and one. If the unfolding probability is greater than this random number, the simulation decides for transition and the protein unfolds at the applied force. Subsequent transitions (e.g. corresponding to the unfolding of intermediates) can now be included into the simulation in the same way. In principle one would also have to take account of the probabilities for back reactions. However, refolding reactions are often negligible as the unbound or unfolded structures are separated by microscopic distances.

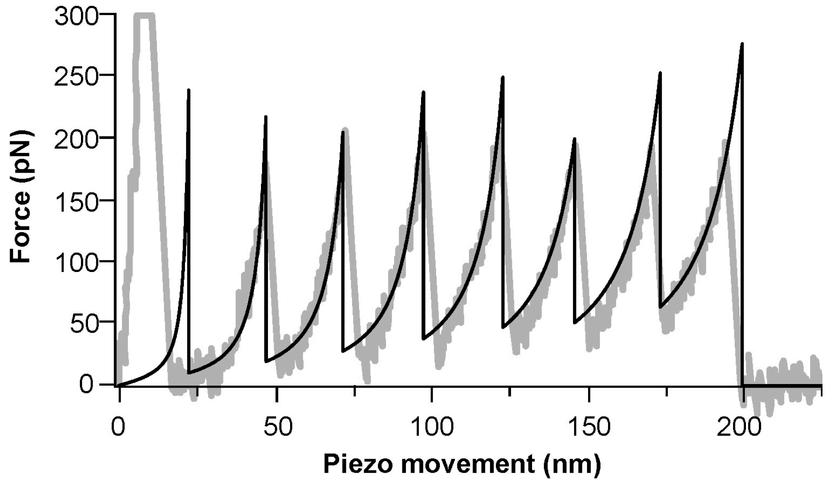

Figure 3-4 MC simulation of the unfolding of a multi-domain protein. A virtual representation of a multi-domain protein consisting of 8 Ig27-domains was unfolded in a MC simulation. Except for the first domain, the simulated F-D curve (solid line) is in very good agreement with the experimental curve (gray line) recorded at the same pulling speed (*v* = 1.31 µm/s). Since all domains are loaded at the same time, the number of folded domains was included in Equation 3.12. For the simulation a domain length of 28 nm and an infinitely stiff cantilever were chosen. The kinetic parameters ($x_{\square}$= 3 Å, k_u = 3.0 X 10^{-5} s^{-1}) were taken from Rief *et al.* (Rief *et al.*, 1997).

In order to analyze experimental DFS data, MC simulations are performed in the same range of pulling speeds as the experiment. At every speed, a few hundred of the unfolding experiments described above are run and compiled to obtained the most probable unfolding force for each speed. For a given pair of $x_{\square}$ and k_u the goodness of the simulation is then determined by calculating chi-square, $\square^2$, according to

$$\chi^2(x_\beta,k_u)=\sum_{i=1}^{n}\left[\frac{F^*(v_i)-F^*_{sim}(v_i;x_\beta,k_u)}{s(v_i)}\right]^2 \qquad 3.13$$

where F^* is the experimentally determined most probable unfolding force, F^*_{sim} the most probable unfolding force determined in the MC simulation, and s denotes the standard deviation (SD) of the experimentally determined most probable unfolding force (Best *et al.*, 2002). Using Equation 3.13 the best pair of x_β and k_u can be found for a given force-speed dataset.

3.3 Experimental procedures

Sample holders

A thin teflon foil (thickness ≈ 3 mm; University of Basel, Basel, Switzerland) was punched to discs with a diameter of ≈ 10 mm (Figure 3-5) and glued to magnetic steel sample holders (Agar Scientific, Stansted, UK) with instant glue (Loctite 770, Koenig, Dietikon, Switzerland). Muscovite mica (Mica New York Corp., New York, NY, USA or Agar Scientific, Stansted, UK) was punched to discs with a diameter of about 5 mm and glued onto the teflon disc with a water-insoluble, two-component epoxy glue (Araldit, Ciba Geigy, Basel, Switzerland). Pyrolytic Graphite (ZYH-grade; Advanced Ceramics, Lakewood, OH, USA) was cut to little squares (5 mm side length, 2 mm thickness) with a razor blade and glued glued onto the teflon disc with epoxy glue.

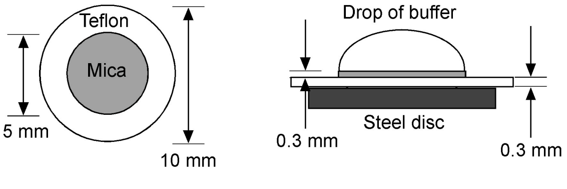

Figure 3-5 AFM sample holder. Steel discs are required to magnetically mount the sample on the piezo-electrical stage. The hydrophobic teflon foils prevent liquids from contacting other surfaces than the freshly cleaved mica.

Sample preparation and buffers

Wild-type PM patches extracted from *H. salinarum* as described (Oesterhelt and Stoeckenius, 1974) were a kind gift of D. Oesterhelt (MPI of Biochemistry, Martinsried). The mica (graphite) surface was cleaved using scotch tape (Milian, Geneva, Switzerland). A 28 μl drop of buffer (300 mM KCl, 20 mM Tris, pH 7.8) was placed on the mica before 2 μl of PM solution (c ≈ 150 μg/ml) were added. After an adsorption time of 15 minutes, the sample was rinsed five times with buffer to remove weakly attached and unadsorbed membranes.

All buffer solutions were prepared with nanopure water (18.2 MΩ*cm; Purelab Plus, ELGA, Celle). Chemicals utilized were purchased from Sigma and were p.a. grade. The Tris buffer (Tris-(hydroxymethyl)-aminomethane) has a pK_a of 8.3. The pH was measured using an electrode pH-Meter with a built-in temperature sensor (766calimatic, Knick, Berlin) and adjusted with HCl.

AFM Instrumentation and force spectroscopy

A commercial AFM (Picoforce, di-Veeco) was equipped with a contact mode fluid cell. The fluid cell was cleaned with dishwasher (Pril, Henkel GmbH, Düsseldorf) and then rinsed with p.a. grade ethanol and nanopure water five times. The spring constants of the Si_3N_4 cantilevers with oxide sharpened pyramidal tips (long thin-legged NP-S: $k_c \approx 0.06$ N/m, $v_{res} \approx 3.8$ kHz, l ≈ 196 μm, w ≈ 23 μm, t ≈ 0.6 μm; short OTR-4: $k_c \approx 0.08$ N/m, $v_{res} \approx 7$ kHz, l ≈ 100 μm, w ≈ 15 μm, t ≈ 0.4 μm; di-Veeco) were calibrated in buffer using thermal fluctuation analysis (Chapter 2.4).

To perform force spectroscopy experiments topographs of the cytoplasmic PM surface were recorded in 300 mM KCl, 20 mM Tris, pH 7.8. The AFM tip was then approached to the cytoplasmic membrane surface and kept in contact with the proteins for about 1 s while applying a force between 300 and 1000 pN. Tip and protein surface were then separated at velocities in the range of 10 nm/s to 5.23 µm/s. In about 15% of all retraction curves one or more adhesive peaks were detected. These curves were recorded using the software of the microscope with sampling rates of 0.5 – 2 kHz.

F-D curve analysis, MC simulations and error estimation of unfolding pathways

F-D curves were imported to Igor Pro (Wavemetrics, Lake Oswego, OR, USA) for data analysis. Every peak of the F-D curves was fitted using the WLC model with a persistence length of 4 Å and a monomer length of 3.6 Å (Chapter 2.5). If the contour length indicates that the peptide is not anchored at the cytoplasmic membrane surface, the thickness of the lipid bilayer (4 nm corresponding to 11 extended aa) must be considered. The correct position of the anchoring residue is then obtained by adding 5 aa (in case the anchoring point was near the middle of the membrane) or 11 aa (in case the anchoring point was near the extracellular membrane surface).

To derive the unfolding forces and probabilities every event of each curve was analyzed. For each peak, the loading rate was calculated using a line fit to a WLC curve of the corresponding length. The curve was fit in the range between 0.33*F and F (Figure 3-6), where F denotes the average rupture force with respect to the unfolding pathway (Figure 3-10).

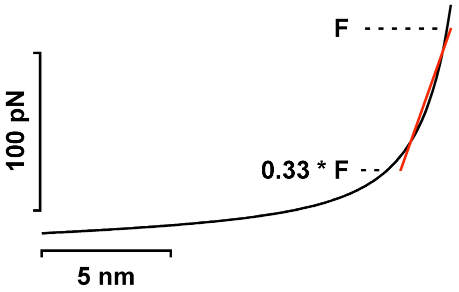

Figure 3-6 Determining the force loading rate. The force loading rates were determined using a line fit (red line) to a WLC curve of the length corresponding to the unfolding peak. The fit was performed between the average unfolding force, F, and 0.33*F. The slope of the fit curve was then multiplied with the pulling speed to determine the loading rate.

MC simulations were performed either in Igor Pro or a custom C++ software programmed by M. Hubain (MPI of Molecular Cell Biology and Genetics, Dresden). The same WLC parameters as for the fitting and a time constant of 1 μs were used. The simulations were run for pairs of x_β (ranging from 1 to 10 Å with 80 linear increments) and k_u (ranging from 1 to 10^{-5} s^{-1} with 20 logarithmic increments). For each pair of x_β and k_u the goodness of the simulations was determined by calculating χ^2 according to Equation 3.13. When determining the shape of energy landscapes, the tilt of the α-helices relative to the membrane normal was not considered, i.e. x_β was assumed to be equal to x_u (Chapter 3.2.2). However, the relative difference in x_β and x_u caused by tilted α-helices will be very small, e.g. ≈3% for a tilt of 15°.

For the unfolding pathways, the standard error of the mean unfolding frequency (SEM) was derived from a binomial distribution. It equals $SEM(p) = \sqrt{\frac{p(1-p)}{N}}$, where p represents the apparent frequency of peak appearance and N the number of unfolding events analyzed. I analyzed 10 (10 nm/s), 84 (50 nm/s), 79 (87 nm/s), 165 (654 nm/s), 121 (1310 nm/s), 23 (2620 nm/s) and 51 (5230 nm/s) individual F-D curves at the indicated pulling speed.

3.4 Results and discussion

3.4.1 Selection of F-D curves

To bind individual BR molecules to the AFM tip I took advantage of the same non-specific interactions as for the multi-domain protein in Chapter 2.6. Figure 3-7 A shows a collection of F-D curves recorded on the cytoplasmic PM surface. The cytoplasmic surface was selected for the experiments as it exhibits the 22 aa long C-terminus[11]. As a direct consequence of the non-specific attachment, the F-D curves showed a large variation in their overall length. This indicated that individual molecules attached to the tip by different regions of their polypeptide backbone. Therefore a clear criterion was required to select those curves, which corresponded to a completely unfolded molecule picked up at the C-terminus. Using the secondary structure of the protein (Figure 3-7 B), I estimated the minimal and maximal length of a F-D curve originating from a completely unfolded BR molecule. A safe number for the upper limit was found by taking the length of the complete BR molecule (247 aa). For the lower limit, I assumed that α-helix A anchored the protein in a last unfolding event and that the tip contacted the C-terminus close to the membrane surface. Subtracting the length of α-helix A (21 aa), the N-terminus (7 aa) and the C-terminus (22 aa) from the length of the protein estimates the minimal length of a fully unfolded BR to 197 aa (Figure 3-7 B).

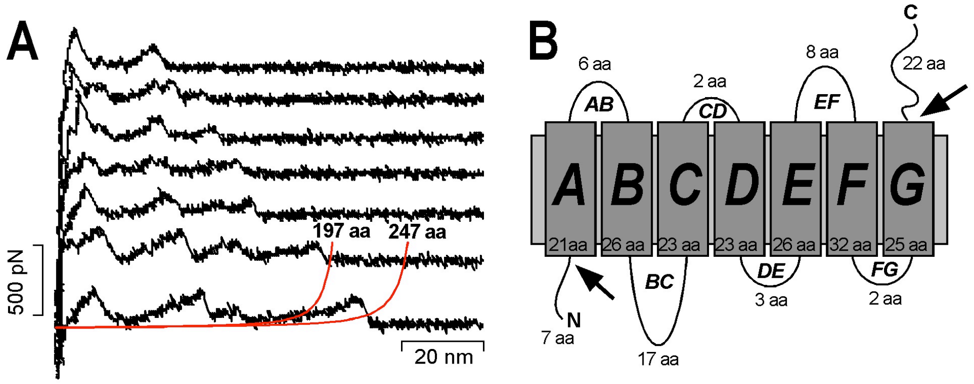

Figure 3-7 Force spectroscopy of BR. (A) F-D curves recorded on the cytoplasmic PM surface. The curves showed a large variation in length and were only considered for further analysis if the last peak lay between WLC curves of 197 and 247 aa length (such as the curve at the bottom). (B) Secondary structure of BR taken from Mitsuoka *et al.* (PDB ID 2AT9; Mitsuoka *et al.*, 1999). The maximum length of a F-D curve reflecting a BR molecule unfolded from the C-terminus corresponds to 247 aa, while the minimum length was estimated to be 197 aa (the distance between the two arrows).

About 50% of the recorded F-D curves were selected using this length criterion, which also assures that the protein was not contacted in the intramembraneous parts of the protein. About 40% of the recorded F-D curves had the final rupture peak at a position earlier than 197 aa indicating the attachment of one of the polypeptide loops. In ≈10% of the recorded curves, the rupture peak occurred after 247 aa. These curves could correspond to the unfolding of more than one protein or contamination of the AFM tip.

---

[11] Preliminary data for N-terminal unfolding of BR from the extracellular side have been collected by M. Kessler (Ludwig-Maximilians-University, Munich).

3.4.2 Unfolding pathways of single bacteriorhodopsins

To highlight common features the selected F-D curves were superimposed according to the adhesion peak, which occurred at a tip-sample distance of ≈ 28 nm. This and two other peaks were observed in all F-D curves indicating a common unfolding pattern among the individual molecules (Figure 3-8).

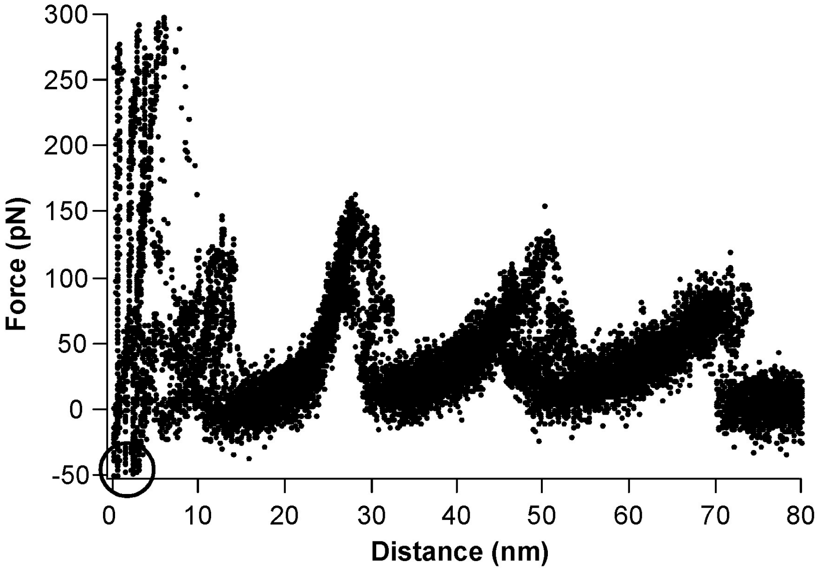

Figure 3-8 F-D curve superimposition. F-D curves were selected with the length criterion and overlaid at the peak at ≈ 28 nm tip-sample distance. Here only 20 curves are shown and each dot represents a datapoint of a recorded F-D curve. A common pattern among the curves is visible showing three main peaks (at 28, 48 and 70 nm tip-sample distance). The small shifts in distance direction near zero (circle) originate from different attachment points of the protein to the tip.

The appearance of several peaks in the F-D suggests sequential unfolding of the protein via several unfolding intermediates. Using the WLC model the three main peaks were assigned to the stretching of unfolded polypeptide fragments of 88, 148 and 219 aa extension lengths (Figure 3-9, red lines). A comparison of these contour lengths with the structure of BR (Mitsuoka *et al.*, 1999) then allowed the following unfolding pathway to be concluded, in agreement with a recently published model (Oesterhelt *et al.*, 2000).

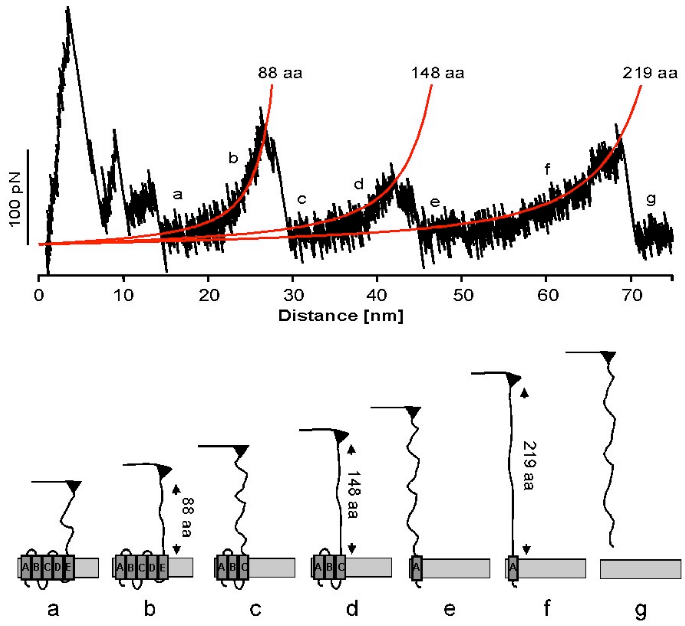

Figure 3-9 Pairwise unfolding pathway of a single BR. The experimental F-D curve was analyzed using the WLC model (red lines) to derive the length of the unfolded elements. These lengths were then used to reconstruct the unfolding pathway of the protein. In this simplest pairwise unfolding pathway α-helices G & F, E & D, and C & B unfold pairwise. For details see text.

The first group of force peaks detected at tip-sample distances below 15 nm indicate the unfolding of α-helices F and G. However, non-specific interactions between the membrane surface and AFM tip were frequently observed in this part of the F-D curve and made a detailed analysis of the peaks difficult (also see Figures 3-8 and 3-10 A). However, after unfolding α-helices F and G, 88 aa are tethered between the tip and the membrane and the is cantilever relaxed (Figure 3-9, frame a). Separating the tip further from the surface stretches the polypeptide (Figure 3-9, frame b) and thereby exerts a pulling force on α-helices E and D. At a certain load, the mechanical stability of α-helices E and D is overcome and they unfold together with loop DE. As the number of aa linking the tip and the surface is now increased to 148 the cantilever again relaxes (Figure 3-9, segment c). In a next step, the 148 aa are extended thereby pulling on α-helix C (Figure 3-9, segment d). After unfolding α-helices B and C and loop BC in a single step the molecular bridge is lengthened to 219 aa (Figure 3-9, segment e). Further separating tip and PM unfolds α-helix A (Figure 3-9, segment f) and the protein is completely extracted from the membrane (Figure 3-9, segment g).

In addition to the three main peaks described above, many F-D curves showed additional events (Figure 3-10). These events indicated that two α-helices did not always unfold pairwise but rather exhibited more unfolding intermediates. To analyze these side peaks, I superimposed every main peak separately as recently suggested (Müller *et al.*, 2002). Three different unfolding pathways named A1 to A3 were found for the unfolding of α-helices G and F (Figure 3-10 A). In the A1 and A2 pathway the peak at 36 aa indicated that α-helix G is already unfolded after tip-sample contact was disrupted. In the A1 pathway, the FG loop and α-helix F then unfolded together in a single step, while in the A2 pathway both elements unfolded in individual steps as indicated by peaks at 36 and 51 aa. In the A3 pathway, the peak at 26 aa indicated that only the cytoplasmic half of α-helix G is unfolded after disruption of tip-sample contact. This event was then followed by unfolding of the extracellular half of α-helix G, the FG loop, and α-helix F each in an individual unfolding step. As already mentioned above these three unfolding pathways of the first two α-helices were not be reproducibly detected in all F-D curves and thus excluded from further analysis.

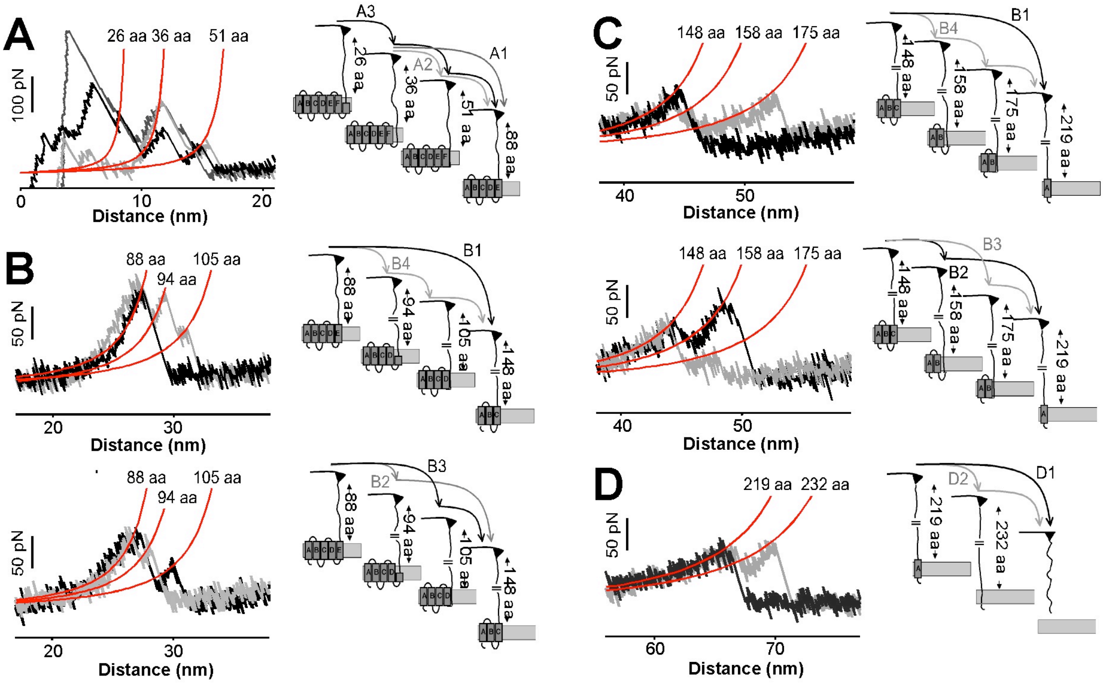

Figure 3-10 Unfolding pathways of BR. Two α-helices do not always unfold pairwise but rather follow a network of unfolding pathways. These pathways are discussed in detail in the text. The contour lengths shown here are the average values, which have been determined with an accuracy of ± 3 aa. The average contour lengths agree with the secondary structure elements within this uncertainty. Here, only one representative curve is shown per pathway, which the average WLC curve does not necessarily fit accurately.

Four different unfolding pathways named B1 to B4 were detected for α-helices E and D (Figure 3-10 B). In the pairwise unfolding pathway (B1), α-helices E and D unfolded with the DE and CD loops in a one-step process. A single unfolding intermediate was detected in the B2 and the B3 pathways, indicating that the two α-helices unfold in a two-step process. In the B2 pathway, α-helix E was partially unfolded (peak at 94 aa) before the remaining part of the α-helix, the DE loop and α-helix D were extracted from the membrane in one more single step. In the B3 pathway α-helix E fully unfolded together with the DE loop (peak at 105 aa), before in a second step the α-helix D was extracted from the membrane. Both intermediates were detected in the B4 pathway, where the two α-helices unfolded in a three-step process.

Four different pathways named C1-C4 describe the unfolding of α-helices B and the C (Figure 3-10 C). In the simplest case the two α-helices, the BC loop and the AB loop unfolded in a one-step process (C1 pathway). As for α-helices D and E, two intermediate unfolding steps were detected for α-helices B and C. In the C2 pathway, α-helix C unfolded in a first step, while the BC loop and α-helix B remained anchored in the membrane prior to unfolding. In the C3 pathway, α-helix C unfolded together with the BC loop in one step before α-helix B was extracted from the membrane. Both intermediates were observed in the C4 pathways where each secondary structure element unfolded in a single step.

Two pathways (D1 and D2) describe the extraction of α-helix A and the N-terminus (Figure 3-10 D). In the D1 pathway, the α-helix A and the N-terminus unfolded in one step while, in the D2 pathway, α-helix A unfolded in a first step before the N-terminus was pulled through the membrane.

In principal one could argue that the some of the shown unfolding peaks result from interactions of the protein with the mica surface. As a control, the same unfolding experiment was also performed on a highly-ordered pyrolytic graphite surface. The corresponding F-D curves are shown in Figure 3-11 and show the same unfolding events as those in Figure 3-10.

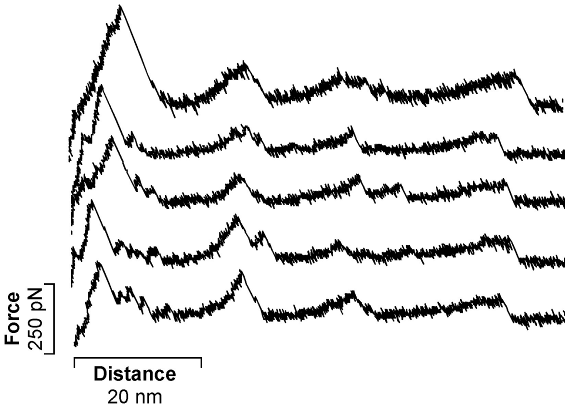

Figure 3-11 Unfolding BR from graphite. To ensure that the unfolding peaks are independent of membrane-surface interactions, BR was also unfolded from graphite. The recorded F-D curves show the same force peaks as those recorded on mica (Figure 3-10). Since one would expect a very different interaction between the protein and graphite compared to mica, these curves indicate that the unfolding intermediates are molecular properties.

3.4.3 Unfolding forces depend on pulling speed

In the unfolding pathways discussed above single and groups of secondary structure elements unfolded at forces between 50 – 200 pN. As one would expect from Chapter 3.2.2, the measured unfolding forces critically depend on the pulling speed. Each superimposition shown in Figure 3-12 is composed of 25 F-D curves recorded at the indicated pulling speeds. Apparently the pulling speed did not influence the unfolding pattern of BR as the individual force peaks remained at their positions (also see Chapter 3.4.6). However, it is evident that the height of the force peaks and thus the average forces required to unfold parts of the protein increased with increasing pulling speed.

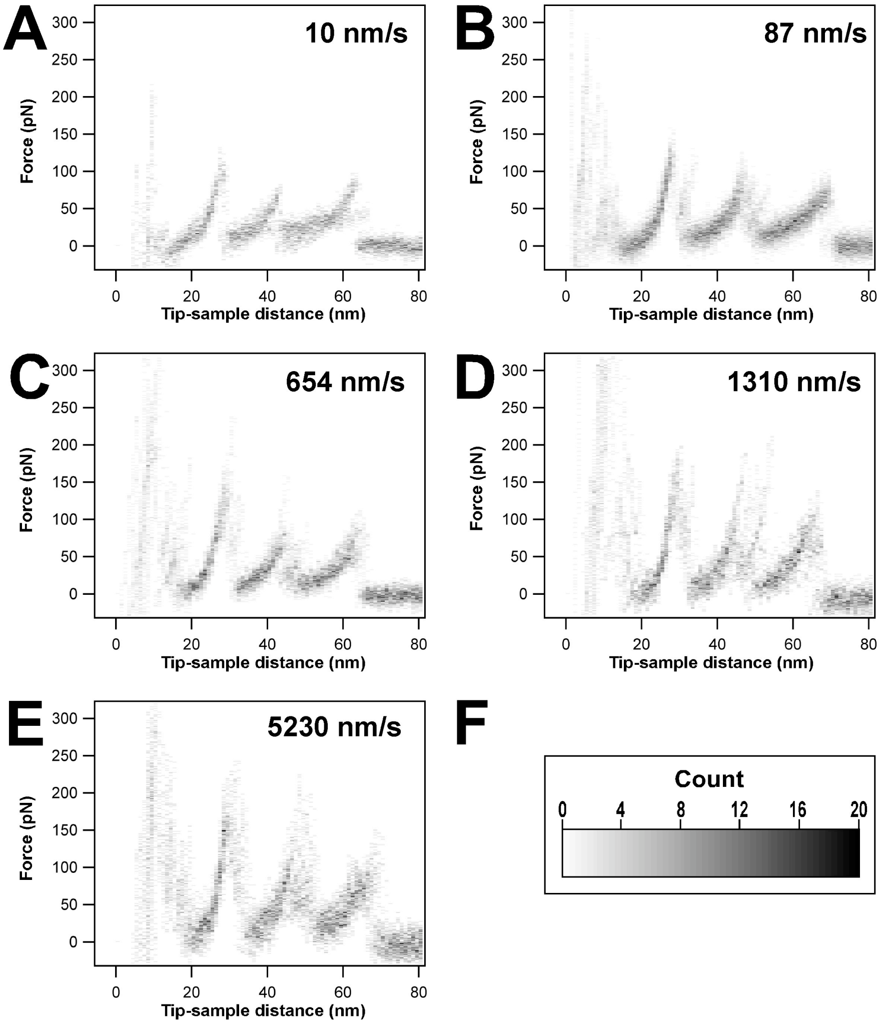

Figure 3-12 Unfolding BR at different pulling speeds. (A-E) Superimpositions of 25 F-D curves recorded on single BR molecules at the indicated pulling speeds. As observed in the superimpositions, the unfolding forces increase with increasing pulling speed. The gray shading of the superimpositions was achieved by compiling two-dimensional histograms. To generate the histograms a grid was applied to subdivide the superimpositions into 1 pN by 1 nm big fields and counting the number of data points in each field. The scale in (F) shows that 20 data points will color individual fields black (normalized to 10 curves with 2048 datapoints).

In Figure 3-13 the unfolding forces of the secondary structure elements are plotted as a function of the logarithm of the pulling velocity. The dynamic force spectrum for pairwise unfolding of α-helices is shown in Figure 3-13 A, while those of single secondary structure elements are given in Figure 3-13 B-F. For all unfolding events, a single linear regime was observed in the dynamic force spectrum, which indicated that the unfolding landscape can be approximated by a two-state model (Figure 3-1). To obtain the width of the potential barrier and the unfolding rates from these data, I have applied (i) Equation 3.10 (Chapter 3.2.2) and (ii) MC simulations (Chapter 3.2.3). The results are presented and discussed in the next chapter.

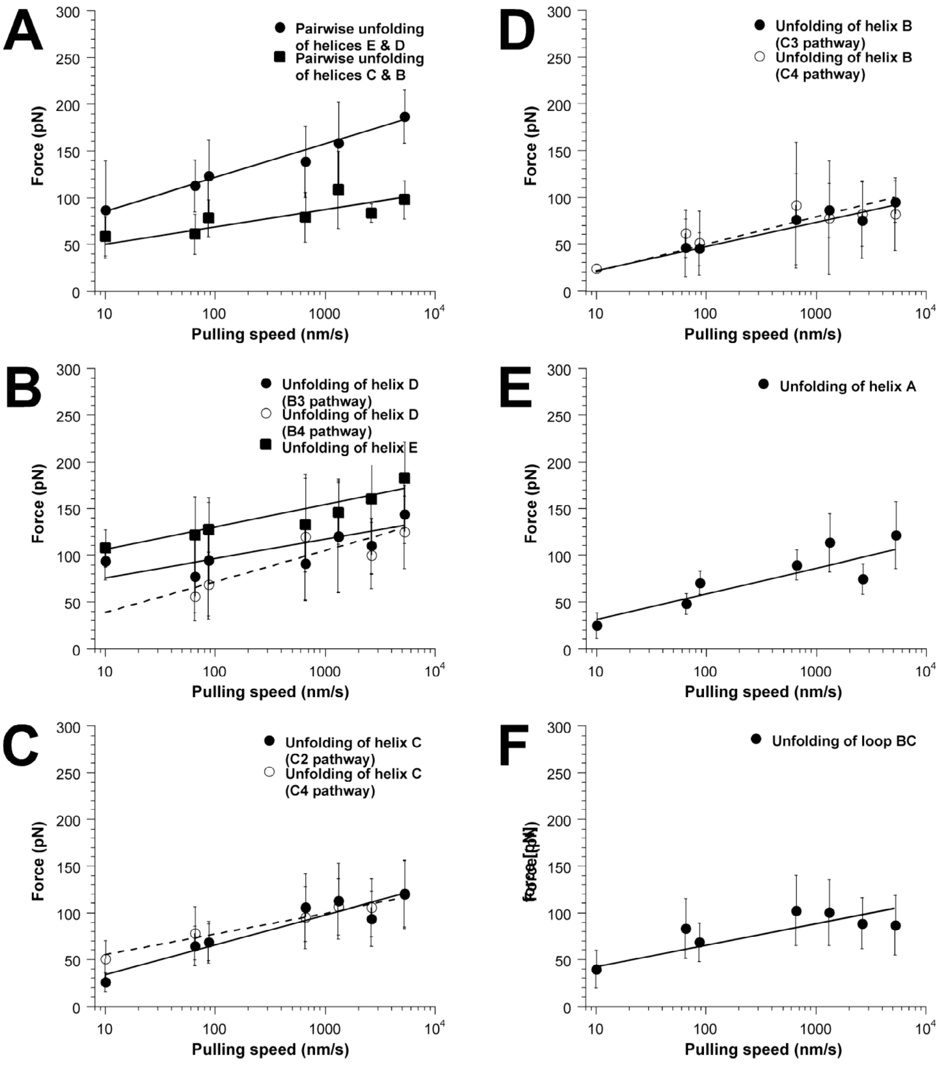

Figure 3-13 Unfolding forces as a function of pulling speed. (A) Pairwise unfolding of α-helices. (B-F) Unfolding of single secondary structure elements. For single and pairs of secondary structure elements a logarithmical increase of the unfolding force with pulling speed was measured. Solid and dashed lines represent MC simulations to analyze the experimental data given by filled (in case of solid lines) and open symbols (in case of dashed lines). Two data sets were obtained and analyzed independently as α-helices D, C and B occurred in two unfolding pathways.

3.4.4 Energy landscape of secondary structure elements

Table 2 summarizes the widths and the unfolding rates characterizing the energy landscapes of the secondary structure elements of BR. The values obtained from the two methods are in good agreement as the results of the MC simulations lie within the errors of the values determined with Equation 3.10.

Structural element(s)	Pathway - Peak position (aa)	Equation 3.10		M-C simulation	
		x_u [Å]	k_u^0 [s^{-1}]	x_u [Å]	k_u^0 [s^{-1}]
Pairwise unfolding of α-helices					
E & D *	B1-88	3.55 ± 0.18	4.7 ± 2.6 X 10^{-3}	3.2	1.0 X 10^{-2}
C & B *	C1-148	6.52 ± 1.65	7.0 ± 21.4 X 10^{-4}	8.6	3.4 X 10^{-5}
Single secondary structure elements					
α-helix E **	B3-88	4.44 ± 0.69	2.3 ± 5.3 X 10^{-4}	4.6	1.1 X 10^{-4}
α-helix D	B3-105	5.92 ± 1.93	1.5 ± 3.6 X 10^{-2}	7.7	1.5 X 10^{-2}
α-helix D	B4-105	3.59 ± 0.74	1.2 ± 1.6 X 10^{-1}	4.0	5.6 X 10^{-2}
α-helix C	C2-148	4.31 ± 0.87	2.3 ± 4.2 X 10^{-2}	3.9	5.6 X 10^{-2}
α-helix C	C4-148	4.71 ± 0.38	8.8 ± 6.8 X 10^{-3}	4.9	6.0 X 10^{-3}
α-helix B	C3-175	4.80 ± 0.65	6.6 ± 6.9 X 10^{-2}	5.4	3.1 X 10^{-2}
α-helix B	C4-175	5.45 ± 0.94	1.9 ± 2.8 X 10^{-2}	5.7	1.7 X 10^{-2}
α-helix A ***	D1-219	6.78 ± 0.97	1.9 ± 3.6 X 10^{-4}	6.8	1.8 X 10^{-4}
Loop BC	C4-158	6.13 ± 1.79	1.4 ± 4.6 X 10^{-3}	5.8	3.0 X 10^{-3}
Groups of secondary structural elements					
α-helix E (Pt. 1)	B2-88	3.46 ± 0.48	2.5 ± 3.2 X 10^{-2}	-	-
α-helix E (Pt. 1)	B4-88	3.51 ± 1.02	1.2 ± 3.6 X 10^{-2}	-	-
α-helix E (Pt. 2) + Loop DE + α-helix D	B2-94	3.17 ± 0.31	3.5 ± 3.1 X 10^{-2}	-	-
α-helix E (Pt. 2)+ loop DE	B4-94	3.19 ± 0.85	3.4 ± 8.6 X 10^{-2}	-	-
α-helix C + loop BC	C3-148	3.82 ± 0.89	7.3 ± 13.4 X 10^{-2}	-	-
Loop BC + α-helix B	C2-158	3.68 ± 0.44	9.5 ± 8.0 X 10^{-2}	-	-
α-helix A	D2-219	3.94 ± 0.67	6.0 ± 7.4 X 10^{-2}	-	-
N-terminus	D2-232	4.12 ± 0.62	3.6 ± 4.1 X 10^{-2}	-	-

* Including the connecting loops (see Figure 3.10)
** Including the 3 aa long loop DE
*** Including the 7 aa long N-terminus. This peak was chosen for the A-helix over the D2-219 peak as later occurs with a very low probability (<10%).

Table 2 Mechanical energy landscapes of secondary structure elements. The widths of the potential barriers and the unfolding rates were determined using MC simulations and Equation 3.10. MC simulations require a lot of computing time and thus were only applied to the helical pairs and single secondary structure elements. Equation 3.10 was applied to all force peaks and also yields the SD of the fit parameters.

For the unfolding of helical pairs (individual α-helices) I observed widths of the potential barriers ranging from 3.2 to 8.6 Å (3.6 to 7.7 Å). The fact that I only found one potential barrier suggests that the same interactions control the strength of the α-helices on a wide range of timescales, ranging from a few ms to seconds. This is apparent contrast to unbinding of biotin from avidin or PSGL-1 from L-selectin, where multiple barriers govern bond strength on the different timescales (Evans *et al.*, 2001; Merkel *et al.*, 1999). The width of the potential barriers indicated whether the α-helices are unfolded within the lipid bilayer or extracted from the membrane prior to unfolding. When extracting a biotinylated C18-lipid from stearoyl-oleoyl phosphatidylcholine bilayers, E. Evans and F. Ludwig found that two potential barriers had to be crossed at 7 and 12 Å respectively (Evans and Ludwig, 2000). As lipid molecules are extracted from the membrane without a large degree of conformational change and consistent with the concept of hydrophobic interaction, the outer barrier is of comparable magnitude to half the bilayer membrane and the inner barrier correlates to the position of the unsaturated bond in the oleoyl chain (Evans and Ludwig, 2000). However, the values I observed for single α-helices are much smaller than half the thickness of the PM (which would correspond to ≈ 30 Å) and thus suggest that breakage of inter- or intramolecular bonds started the unfolding process. This initial step could then be followed by cooperative unfolding or 'unzipping' of the helical structures.

The widths of the potential barriers also give an unambiguous answer if the detected unfolding pathways really reflect different unfolding trajectories in the potential landscape of the protein. The data in Table 2 show that the location of the transition state of a certain force peak is characteristic for the unfolding pathway. For example, unfolding of α-helix C occurred at the same position in the force spectrum as pairwise unfolding of α-helices C and B (Figure 3-10). Although in both cases force was applied to α-helix C, the individual extraction of α-helix C was triggered by ≈ 4.6 Å extension while in case of the pairwise unfolding of α-helices C and B the polypeptide had to be extended ≈ 7 Å. This indicates that two distinct unfolding routes along two different transition states were followed. This effect was also observed (albeit less clear) for the pairwise and stepwise unfolding of α-helices E and D.

The natural transitions rate over the potential barriers give a measure for the stability of the secondary structure elements in the absence of force. I found spontaneous unfolding rates in the range from 1.1 X 10^{-4} to 1.2 X 10^{-1} s^{-1} for single α-helices and 3.4 X 10^{-5} to 1.0 X 10^{-2} s^{-1} for pairs of α-helices (Table 2). Remarkably these values are of comparable magnitude to small water-soluble proteins like barnase (k_u = 2.3 X 10^{-5} s^{-1}; Best *et al.*, 2001) and Ig27 (k_u = 1.2 X 10^{-4} s^{-1}; Carrion-Vazquez *et al.*, 1999; Williams *et al.*, 2003). This result shows that individual transmembrane α-helices, which are considered folding intermediates, exhibit sufficient stability to form stable fragments prior to their assembly during the folding process. From the unfolding rates the free energy of activation required to unfold single and pairs of α-helices was calculated using Equation 3.6. Using relaxation times between 10^{-7} and 10^{-9} s (Chapter 3.2.2), I found activation energies of the order of 15 – 30 kcal/mol. These values lie relatively close to the theoretically predicted values (80 – 100 kcal/mol, Chapter 1.2.2). A more detailed discussion of the unfolding rates and comparison of the individual secondary structure elements is impeded by the fact that the values are typically associated with an error of one magnitude or more.

3.4.5 Unfolding pathways depend on pulling speed

Interestingly I found that the pulling speed also had an influence on the unfolding pathways. Although every possible pathway was observed at each pulling speed, the tendency of individual molecules to follow certain pathways was significantly altered. The unfolding probability of single α-helices increased with pulling speeds while pairwise unfolding was less often detected (Figure 3-14).

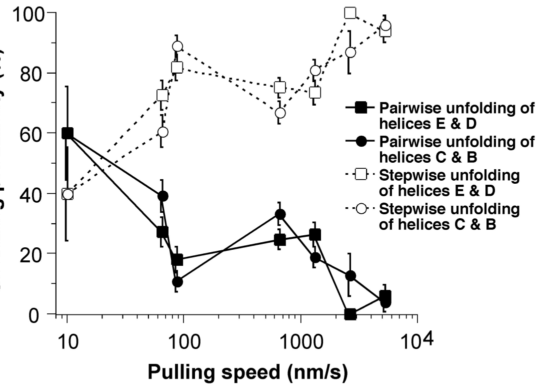

Figure 3-14 Unfolding pathways depend on pulling speed. The probability for unfolding single secondary structure elements increased with the pulling speed, while less pairwise unfolding was observed. The error bars correspond to the SEM frequency (Chapter 3.3). There was no observable speed-dependence of the two unfolding pathways of α-helix A and the N-terminus; only in rare cases (<10%) these element unfolded in two steps.

This indicated that the application of force tilted the unfolding barrier for single α-helices more than for pairwise unfolding. For α-helices E and D this seems very plausible as the unfolding barriers of single α-helices are wider as those for pairwise unfolding (Table 2) and energy barriers are always reduced proportional to their widths (Chapter 3.2.2). Interestingly, such force-induced pathways shifts have recently been reported for selectins (Barsegov and Thirumalai, 2005; Evans *et al.*, 2004) and the GTPase Ran (Nevo *et al.*, 2003).

Extrapolating the speed dependence of the unfolding pathways to slow pulling speeds suggests that the α-helices almost exclusively unfold in a pairwise conformation in the absence of force. This indicates that under native conditions the energy barrier for pairwise unfolding is significantly lower than the barriers of the two α-helices. Consequently the energy landscape can be qualitatively approximated such as shown in Figure 3-15. Although this landscape was sketched based on data collected in an off-equilibrium unfolding experiment, one might speculate that it is also valid for protein folding. In this case, the differences in the heights of the energy barriers would suggest that two α-helices preferably follow a pairwise folding pathway at equilibrium. Such a pairwise association of transmembrane α-helices during membrane protein folding was predicted to play an important role during membrane protein folding (Engelman and Steitz, 1981) and this prediction was also experimentally confirmed (e.g., see Kuhn, 1987).

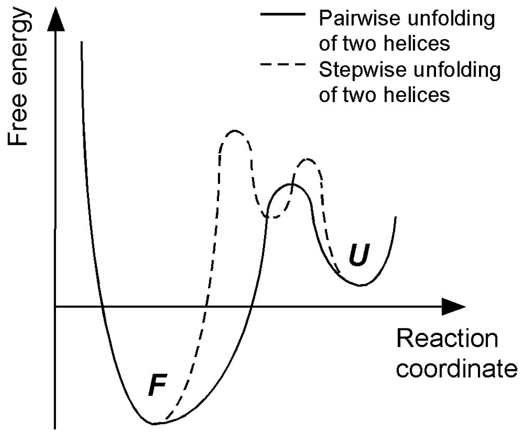
Free energy
Pairwise unfolding of two helices
Stepwise unfolding of two helices
U
F
Reaction coordinate

Figure 3-15 Energy landscape of a helical pair. Two possible unfolding routes exist for pairs of α-helices in BR. From the folded state (*F*) the two α-helices are either unfolded individually (dashed line) or pairwise (solid line) to the unfolded state (*U*). The shown approximation of the potential landscape at native conditions (zero force) was generated by extrapolating the speed-dependent unfolding probabilities to zero-force (Figure 3-14). Since the experimental data showed that the pairwise unfolding was chosen more frequently, its potential barrier should be lower than that for unfolding of individual α-helices.

3.5 Conclusions

Relatively little is known about the stability of membrane proteins. In the preceding chapters I have presented a single-molecule unfolding study of the membrane protein BR. In force spectroscopy experiments an external pulling force was applied to individual proteins resulting in sequential unfolding of their three-dimensional structures. Thus, in apparent contrast to conventional chemical or thermal denaturation approaches the off-equilibrium properties of single molecules were addressed here. The experiments revealed that individual BR molecules follow well-defined unfolding pathways via several unfolding intermediates. Although single α-helices were sufficiently stable to unfold in individual steps, they exhibited a certain probability to unfold pairwise. The observation that single α-helices are independently folded elements strongly supports the two-stage model of membrane protein folding (Chapter 1.2.2).

DFS experiments provided detailed insights into the mechanical energy landscape of these secondary structure elements. I found that single α-helices were stabilized by single potential barriers. It was also observed that α-helices associated pairwise forming a collective potential barrier. This clearly demonstrated that several unfolding trajectories in the molecules energy landscape co-exist. Mechanical unfolding of single α-helices was triggered by an extension of only ≈ 5 Å. This indicated that breakage of intramolecular interactions between or within secondary structure elements represented the starting point of a cooperative unfolding process. As one would expect, the position of the transition state during unfolding of the α-helices was in apparent contrast to the ones observed during the extraction of lipid molecules from membranes and suggested that α-helices are unzipped within the membrane bilayer. Molecular dynamics simulations will be required to provide further insights into the details of the unfolding process including the exact sequence of events associated with the unzipping of individual α-helices.

For the single α-helices I found natural unfolding rates of the order of 10^{-2} s^{-1}. Thus the stability of single α-helices is ≈ 100 s, which seems to be sufficient for assembly during the folding process. The DFS experiments also showed that these unfolding probabilities sensitively depend on the pulling speed. While the unfolding probability of single α-helices increased that of pairwise unfolding decreased with increasing pulling speed. Such forced induced pathway shifts have recently been reported for other biomolecular systems (Barsegov and Thirumalai, 2005; Evans *et al.*, 2004; Nevo *et al.*, 2003). Interestingly these data also indicated a pairwise association of α-helices in the absence of force and thus support the helical hairpin model of membrane protein folding (Engelman and Steitz, 1981).

4. Extended range of AFM force loading rates

4.1 Introduction

As introduced in Chapter 3, DFS experiments provide insights into the energy landscapes of biomolecular bonds by probing the potential barriers crossed during unfolding or unbinding processes. In case of the α-helices of BR, I found that ≈ 5 Å extension trigger their unfolding across single potential barriers. In apparent contrast, Merkel *et al.* demonstrated that during unbinding of biotin from avidin several potential barriers are crossed (Lo *et al.*, 2001; Merkel *et al.*, 1999). In the meantime, such mountainous energy landscapes have been reported for many weak non-covalent bonds (for a review, see Evans, 2001).

These examples illustrate that, in order to be able to detect multiple potential barriers, a wide range of loading rates spanning several orders of magnitude should be experimentally accessible. Most recent DFS experiments with the AFM had in common that the pulling speed was varied in the range from ≈ 10 nm/s to ≈ 10 µm/s (de Paris *et al.*, 2000; Williams *et al.*, 2003). However, to obtain a more complete picture of their kinetic properties, it would be desirable to investigate the systems in an increased range of pulling speeds (Lo *et al.*, 2001). At speeds higher than ≈ 10 µm/s, the speed-dependent hydrodynamic drag force acting on the cantilever is of the same magnitude as the peak forces measured on single biological molecules. As the tip velocity is not constant during typical measurements large deviations in the measured forces could be obtained if hydrodynamic effects are not considered. Thus hydrodynamic effects are currently limiting the maximum pulling speed and thus force loading rate in AFM force spectroscopy experiments.

Here, I combined hydrodynamic force measurements and theoretical considerations to provide an off-line method for the correct evaluation of force measurements recorded at pulling speeds up to three orders of magnitude higher than previously possible. To support and illustrate the theoretical considerations, the mechanical unfolding of a multi-domain protein consisting of 8 Ig27-domains was experimentally addressed at 30 µm/s pulling speed. I found that the presented method provides a more realistic picture of biomolecular interactions at fast pulling speeds. Other factors limiting AFM pulling speeds are discussed, also with respect to small cantilevers and other force probe methods.

4.2 Experimental procedures

AFM Instrumentation

A commercial AFM (Picoforce, di-Veeco) was equipped with a X-Y-Z-piezo scanner with a sensored and closed-loop 20 µm Z-axis. The spring constants of the silicon nitride cantilevers (small V-shaped lever: Olympus OTR4, see Chapter 3.3; large V-shaped lever: Microlever MSCT-AUNM-C, k_c ≈ 0.015 N/m, l ≈ 320 µm, w ≈ 22 µm, t ≈ 0.6 µm; di-Veeco) were calibrated in liquid using thermal fluctuation analysis (Chapter 2.4).

Sample preparation and F-D curve analysis

Individual Ig27-8 molecules were unfolded after adsorption to a freshly prepared gold surface using the large V-shaped lever in PBS (Sigma) as described in Chapter 2.6. I used the WLC model with a persistence length of 4 Å and a monomer length of 3.6 Å to describe the force-extension relationship of unfolded parts of the protein in the force spectrum (Chapter 2.5).

Correcting F-D curves for hydrodynamic drag forces

The recorded F-D curves were corrected for hydrodynamic drag using custom macros and built-in functions of Igor Pro. The curves were collected with the software of the AFM and then imported into Igor Pro. In order to reduce noise, I replaced the piezo-movement curves with line fits and the tip-sample distance was recalculated from these fits as described below. The velocity was calculated using a line fit window sliding over the smoothed tip-sample distance curve. The empirical drag coefficients, a_{eff} and d_{eff} (see below) ,were determined for every cantilever from F-D curves recorded at 70 µm/s pulling speed on the same sample surface where the unfolding experiments were performed.

4.3 Results and discussion

4.3.1 Hydrodynamic drag force acting on an AFM cantilever

Like any other object moved in a solution the AFM cantilever experiences a hydrodynamic drag force due to viscous friction with the surrounding liquid. Drag forces have been previously quantified for spheres as well as for an AFM cantilever close to a surface (Alcaraz *et al.*, 2002; Benmouna and Johannsmann, 2004; Cox and Brenner, 1967; Gittes and Schmidt, 1998). For the cantilever it has been suggested to scale the dimensions of the lever and the distance to the surface by introducing two empirical coefficients (Alcaraz *et al.*, 2002; O'Shea and Welland, 1998; Roters and Johannsmann, 1996). The drag force, F_d, acting on the cantilever can then be described as

$$F_d = \frac{6\Box\Box a_{eff}^{\ 2}}{d + d_{eff}} \cdot v_{tip} \qquad 4.1$$

where □ is the viscosity of the liquid, d the tip-surface distance and v_{tip} denotes the tip velocity. The empirical coefficients a_{eff} and d_{eff} represent the effective size of the cantilever (a_{eff}) and the effective cantilever tip height (d_{eff}) respectively. Equation 4.1 is valid in regimes of purely viscous flow, i.e. where the Reynolds number, Re, is below 1. The Reynolds number is given by

$$\mathrm{Re} = \frac{a_{eff} v_{tip} \Box}{\Box} \qquad 4.2$$

where □ is the density of the solution. For a typical measurement in water at room temperature (□ = 1 mNs/m^2, □ = 1 g/cm^3), Re is well below 1 for pulling speeds as high as a few millimeter/s.

The hydrodynamic drag force was quantified as a function of pulling speed and tip-sample distance for two V-shaped cantilevers of different size. Figure 4-1 A shows the linear dependence of the drag force on the pulling speed and Figure 4-1 B the more complex dependence on the tip-surface distance.

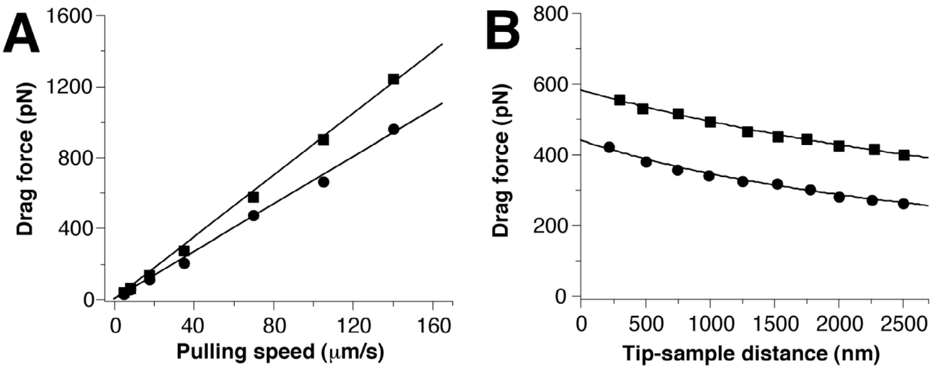

Figure 4-1 Hydrodynamic drag force acting on an AFM cantilever. Force measurements with AFM cantilevers are subject to hydrodynamic drag forces, which depend on the pulling speed and tip-sample distance. (A) Linear dependence of the drag force on the pulling speed recorded at a distance of 500 nm to the surface. Slopes of the linear fits are 8.68 ± 0.11 pNs/□m (squares, large lever in PBS) and 6.67 ± 0.11 pNs/□m (circles, small lever in water). (B) Non-linear dependence of drag force on the tip-sample distance (recorded at 70 □m/s), which allows determining the empirical drag coefficients a_{eff} and d_{eff} according to Equation 4.1 (solid lines). SDs are of comparable size as the markers.

As predicted, an increase in the drag force is observed close to the surface (Benmouna and Johannsmann, 2004; Roters and Johannsmann, 1996). Consequently, a_{eff} and d_{eff} were determined by measuring the drag force at a fixed speed for different tip-sample distances and fitting the data with Equation 4.1. For a_{eff} I obtained 35.13 ± 0.07 μm (small lever) and 52.06 ± 0.08 μm (large lever), while d_{eff} was 3.70 ± 0.18 μm (small lever) and 5.48 ± 0.17 μm (large lever). Although the above model predicts $F_d = 0$ for large separations, it accurately describes the drag force for a range of tip-sample distances sufficient for single-molecule force measurements (0 - 2.5 μm, Figure 4-1 B).

4.3.2 Correcting hydrodynamic effects

From Figure 4-1 it becomes clear that the hydrodynamic force has to be considered in force measurements with pulling speeds above a few μm/s as it reaches the same magnitude as the forces measured on single molecules. Including a correction factor for the hydrodynamic drag is complicated by the fact that the tip velocity is not constant during a typical measurement. Bending of the cantilever towards the surface is observed in most experiments where the cantilever is connected to the surface via flexible linker molecules, such as polymer spacers for the study of single ligand-receptor pairs or already unfolded domains in case of proteins (Hinterdorfer *et al.*, 2000; Rief *et al.*, 1997). Thus, a direct consequence of any adhesive event is that the tip velocity decreases. We recall from Chapter 2.2 that in these cases, the tip-surface distance can be written as

$$d = z_P - x \qquad 4.3$$

where z_p is the distance the surface has moved and x the cantilever deflection. The tip velocity can then be calculated by taking the derivative of the tip-sample distance with respect to time for each point of the curve according to

$$v_{tip} = \frac{dd}{dt} \qquad 4.4$$

As the tip velocity decreases during the measurement the hydrodynamic drag force acting on the cantilever will also decrease. Therefore, the real force applied to the molecule is underestimated if hydrodynamic effects are not considered. This additional hidden force, ΔF, can be written as

$$\Delta F = F_d(v,d) - F_d(v_{tip},d) \qquad 4.5$$

It is equal to the difference between the drag force calculated for the constant speed of the surface, $F_d(v,d)$, and the drag force calculated by taking the tip velocity at each point of the curve into account, $F_d(v_{tip},d)$. Accordingly the net force, F_{net}, acting on the molecule is

$$F_{net} = F_{measured} + \Delta F \tag{4.6}$$

where $F_{measured}$ is the measured F-D curve. Equation 4.6 is valid if the offset of the unprocessed data was corrected by moving the non-contact part of the curve to zero force.

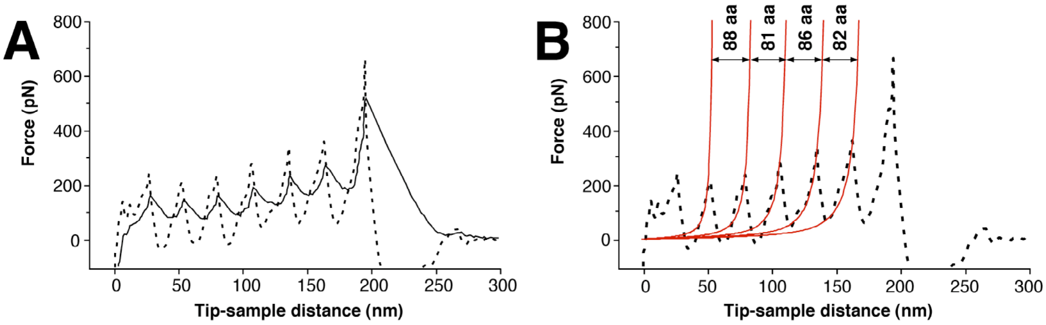

Figure 4-2 Unfolding a multi-domain protein at a pulling velocity of 30 μm/s. (A) F-D curve recorded during unfolding of a Ig27-8 molecule (solid line). The sequential unfolding of the domains results in the characteristic saw-tooth pattern. The dashed line corresponds to the same F-D curve after consideration of the hydrodynamic drag force. A significant increase in the peak forces by ≈50% is observed. (B) Fitting the corrected F-D curve with the WLC model indicates good agreement between the corrected experimental data and the expected extension pattern.

The predicted underestimation was observed during the unfolding of an Ig-27-8 at 29.7 μm/s (Figure 4-2). The continuous extension of the multi-domain protein leads to sequential unfolding of the domains and thus the curve shows the characteristic saw-tooth pattern (Figure 4-2 A, solid line). I measured an average unfolding force of 207.8 ± 35 pN (n=25) for the unfolding of single Ig27 domains. However, a force of ≈ 250 pN would be expected at this pulling speed when one extends the experimentally determined speed dependence of the unfolding forces to 30 μm/s (Williams *et al.*, 2003). To attribute this disagreement to the hydrodynamic effect described above, the tip-sample distance (Figure 4-3 A) and the tip velocity (Figure 4-3 B) was inspected in the course of the measurement. The tip-sample distance was derived according to Equation 4.3 and each of the 7 force peaks leads to a local deviation from the linear behavior (Figure 4-3 A, arrows). Remarkably, the tip velocity (Figure 4-3 B, solid line) is not constant during the F-D curve and differs by as much as ≈50% from the speed of the surface (Figure 4-3 B, dashed line). As mentioned above, the tip moves slower where the cantilever bends towards the surface. From the tip velocity I calculated the hydrodynamic drag force acting on the cantilever following Equation 4.1 (Figure 4–3 C). The observed decrease in the drag force indicates that the molecule is subject to a hidden force in addition to the measured force. The re-evaluation of the experimental curve following Equation 4.6 is shown in Figure 4-2 B, where the dashed line corresponds to the corrected F-D curve. It becomes clear that consideration of the hydrodynamic drag increases the peak forces significantly. After the correction the measured unfolding force of a single Ig27 domains is 274.7 ± 37.5 pN (n=25). As this value lies within the expected range it is suggested that correcting for the hydrodynamic drag allows a more correct evaluation of the measurement obtained at 29.7 μm/s pulling speed.

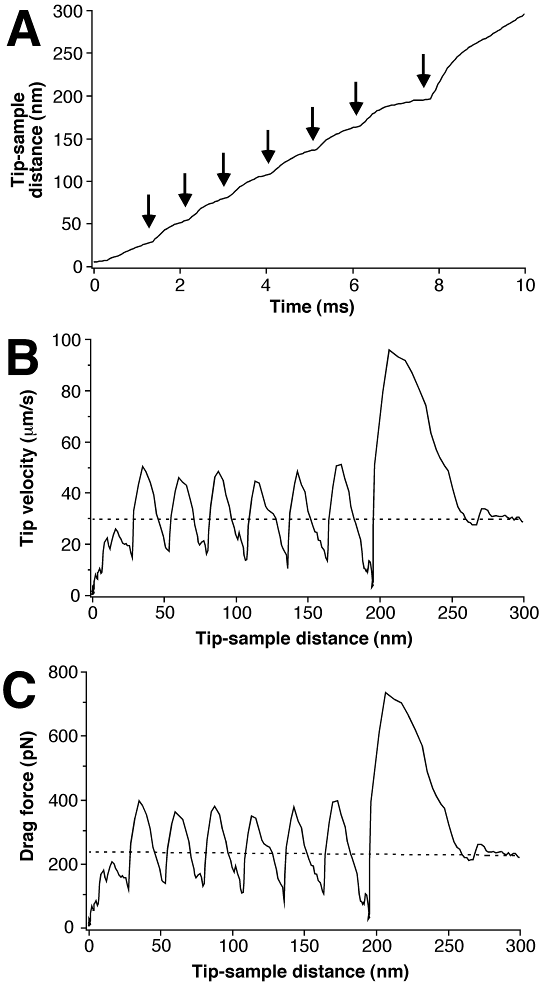

Figure 4-3 Tip velocity and hydrodynamic drag force. (A) The separation of tip and sample during the measurement shown in Figure 4-2 A was derived following Equation 4.3. A ridge in the linear curve is observed where the cantilever interacts with the surface (arrows). (B) The tip-sample distance was derivated with respect to time according to Equation 4.4 to obtain the velocity of the tip for each point of the F-D curve. As expected the tip moves slower when the cantilever interacts with the surface. (C) The hydrodynamic drag force acting on the tip of the cantilever was calculated for each point of the curve according to Equation 4.1. The dashed line indicates the drag force for an untethered cantilever.

4.3.3 Comparison to small cantilevers and other force probe methods

Such fast pulling experiments could previously only be conducted with ultra-small cantilevers (Viani *et al.*, 1999). Ultra-small cantilevers are typically ≈ 10-14 μm long, 3-5 μm wide and 100 nm thick (Viani *et al.*, 1999). The reduced cantilever size results in smaller drag coefficients and higher resonance frequencies and thus gives access to higher pulling speeds. However, the use of such small cantilevers requires special instrumentation with a smaller laser spot size (Viani *et al.*, 1999).

Furthermore the production and handling of small cantilevers is challenging as in order to obtain the same spring constant the cantilever needs to be thinner compared to regular cantilevers. It is important to note, that the presented correction procedure is also suitable to extend the pulling speed range of ultra-small cantilevers.

Although many force probe methods have been developed (Chapter 2.1), the AFM and the BFP may comprise the most frequently used techniques to measure forces at a single molecule level. The approach presented here allows a more complete investigation of the kinetic properties of single molecules by AFM as the range of accessible loading rates is extended. An extension becomes especially important, as force measurements performed with the BFP are limited to loading rates of ≈ 10^5 pN/s. This estimation is based on a maximal vesicle spring constant of 3 pN/nm and retraction speed of 20 μm/s (Evans, 2001; Merkel *et al.*, 1999). Faster retraction speeds may be difficult to achieve due to the temporal resolution of the optical detection systems and hydrodynamic contributions. As a loading rate of 10^5 pN/s corresponds to a pulling speed of 10 μm/s in AFM experiments (assuming a linker stiffness of 10 pN/nm) loading rates one to two orders of magnitude higher than the BFP now are accessible with AFM.

4.3.4 Other factors limiting AFM pulling speeds

The apparent maximum instrumental pulling speed in AFM single molecule force measurements is a few hundred μm/s (Lo *et al.*, 2001). However, even after considering hydrodynamic contributions, the resonance frequency of the cantilever and its visco-elastic response time limit AFM force measurements to lower pulling speeds. To ensure a proper response of the cantilever the frequency of any repetitive feature in the F-D spectrum should be significantly lower than the resonance frequency of the cantilever (Viani *et al.*, 1999). For pulling Ig27-8 with a cantilever of ≈ 8 kHz resonance frequency (e.g. the small V-shaped lever) a speed of ≈ 100 μm/s is the limit as this corresponds to a peak frequency in the F-D curve of ≈ 3 kHz. For BR, the resonance frequency of the cantilever limits the maximum pulling speed to a few μm/s (Chapter 3.4.3), since the unfolding peaks are often only separated by a few nm and thus appear with a very high frequency in the F-D curves.

Since the cantilever can be modeled as a Voigt-Kelvin (V-K) element (Chapter 5.2.1), its visco-elastic response shows creep determined by the spring constant, k_c, and the damping coefficient, η_c (Schultz, 1974). As a consequence any force is only properly detected if it is applied to the cantilever for timescales longer than $\tau = \eta_c / k_c$, which is the retardation time of the V-K element (Schultz, 1974).

Assuming a probe damping of the order of 10^{-3} pNs/nm (Chapter 5.4) and a spring constant of 100 pN/nm, the time scale of visco-elastic responses lies in the range of 10^{-5} s. Consequently a typical cantilever has a visco-elastic response frequency of ≈ 100 kHz and yields ≈ 30 responses per unfolding peak (≈ one response per nm) when unfolding Ig27-8 at 100 μm/s. In addition to the oscillatory measurements presented in Chapter 5, the response time is experimentally determined from the exponential relaxation of a cantilever after force peaks (Evans, 2001).

4.4 Conclusions

The AFM allows measuring the critical forces that unfold single proteins and rupture individual receptor-ligand bonds. To probe the shape of the energy landscape the dynamic strength of the system is probed at different force loading rates preferably spanning several orders of magnitude. This is usually achieved by varying the pulling speed between a few nm/s to a few μm/s, although for a more complete investigation of the kinetic properties higher speeds are desirable. The maximum pulling speed in AFM single-molecule force spectroscopy experiments was currently limited by a speed dependent hydrodynamic drag force, which reaches the same order of magnitude as the molecular forces above 10 μm/s pulling speed.

Here, I showed that the tip velocity significantly decreases when an AFM cantilever interacts with a surface via a polymeric linker. Thus, to avoid an underestimation of the forces applied to the studied interactions, the hydrodynamic force acting on the cantilever has to be considered in measurements recorded at pulling speeds > a few μm/s. The approach presented here allows to estimate the hydrodynamic contributions as function of pulling speed and tip-sample distance and therefore to extend the range of pulling speeds for all types cantilevers. Thus a more complete investigation of the kinetic properties under force is now achievable as it was shown that the dynamic range of bond strengths probed is currently primarily limited by the AFM pulling speed.

5. Visco-elasticity of single bacteriorhodopsins

5.1 Introduction

The mechanical properties of biological macromolecules play an important role in many fundamental biological processes (e.g., see Bustamante *et al.*, 2004; Howard, 2001) and thus have been extensively studied in force spectroscopy experiments. However, conventional F-D measurements are only capable of revealing the elastic response of the single molecules under consideration. In apparent contrast, most bio-molecular interactions exhibit time-dependent elastic and viscous forces (Humphris *et al.*, 2002; Humphris *et al.*, 2000; Sheu *et al.*, 2001; Thompson *et al.*, 2001), which should be analyzed independently analyzed to allow a deeper understanding of dynamic biological processes. In this chapter, I will introduce two force spectroscopy techniques suitable to measure the visco-elastic properties of single (bio-)molecules and apply them to BR.

The first approach is based on force modulation spectroscopy (FMS), which was pioneered by A. Humphris and M. Miles (Humphris *et al.*, 2000). In FMS, the AFM cantilever is sinusoidally oscillated while a single molecule is extended between the tip and the surface. Although a number of different groups have already applied FMS to study single molecules (e.g., see Forbes and Wang, 2004; Kienberger *et al.*, 2000; Ptak *et al.*, 2001), only their elastic responses were studied. Here, a more complete experimental and theoretical framework is presented, which allows elastic and dissipative molecular interactions to be uncoupled.

The second approach is based on the analysis of the Brownian motion of the AFM cantilever. In their initial experiments, Roters *et al.* monitored the thermal noise of the AFM cantilever at different separations from polymeric surfaces (Roters and Johannsmann, 1996). Here, I will demonstrate that the thermal cantilever motion can be analyzed during conventional F-D measurements to reveal the visco-elastic properties of single molecules. In the following, I will begin with introducing the theoretical concepts underlying the two techniques. Then I will compare their sensitivity and measure the visco-elastic response of single BRs.

5.2 Theoretical considerations

5.2.1 Resonance response of an AFM cantilever

A theoretical understanding of the motion of the AFM cantilever is a prerequisite to analyze the dynamic properties of a single molecule attached to it. In the simplest model, the cantilever is described as sphere attached to a spring. Assuming a harmonic response, the angular resonant frequency of the cantilever, ω_0, is (Chen *et al.*, 1994; Sarid, 1994)

$$\omega_0 = \sqrt{\frac{k_c}{m_c}} \qquad 5.1$$

where k_c is the spring constant and m_c the effective mass of the cantilever[12]. Within the context of this simple harmonic oscillator (SHO) model, the motion of the tip can be described by the following second order differential equation

$$F(t) = k_c x(t) + \gamma_c \frac{dx(t)}{dt} + m_c \frac{d^2x(t)}{dt^2} \qquad 5.2$$

Here, $F(t)$ is a driving force, x the tip displacement and γ_c the damping coefficient. The damping of the cantilever is often schematically represented by a dashpot and consequently the cantilever can be described as a V-K element (Figure 5-1). Importantly, the damping coefficient and the effective mass are not necessarily properties of the cantilever alone but also depend on its environment, such as the viscosity of the surrounding medium (Chen *et al.*, 1994; Roters and Johannsmann, 1996) or whether a molecule has attached to the tip (see below).

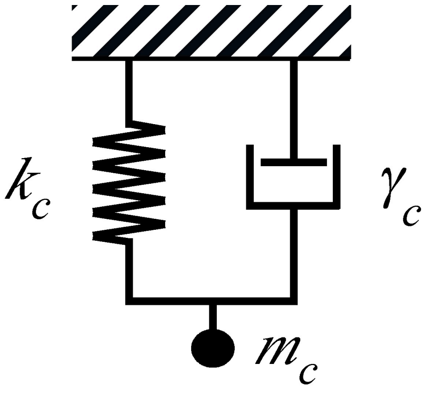

Figure 5-1 SHO model of the AFM cantilever. The cantilever is modelled as a bead of the mass m_c attached to spring with spring constant k_c and a dashpot with damping coefficient γ_c. The motion of such a V-K element is described by Equation 5.2.

---

[12] Equation 5.1 is valid in the absence of heavy damping. Generally speaking the resonance frequency, ω_{res}, is given by $\omega_{res} = \omega_0\sqrt{1 - \frac{1}{4Q^2}}$, where Q is the Q-factor (see below).

For a cantilever in air or liquid at ambient temperatures, the left hand side of Equation 5.2 equals a stochastic, frequency independent thermal drive force. If the cantilever is driven such as in dynamic force microscopy (Chapter 1.2), the left hand side of Equation 5.2 equals a sinusoidal driving force of the form $F_0 \cos(\omega t)$, where F_0 denotes the magnitude of the drive force (see below)

In addition to the thermal or external excitation of the cantilever, the deflection signal can contain electronic, acoustic or vibrational noise and mechanical drift. To exclude these sources of noise, the motion of the cantilever is most commonly analyzed in the frequency space. Fourier-transformation yields a frequency dependent amplitude spectrum, which can be described by (Chen *et al.*, 1994; Sarid, 1994)

$$A(\omega) = A_{DC} \frac{\omega_0^2}{\sqrt{(\omega_0^2 - \omega^2)^2 + \frac{\omega_0^2 \omega^2}{Q^2}}} \qquad 5.3$$

Here A_{DC} is the DC-amplitude, ω the cyclic frequency, ω_0 the cyclic resonant frequency ($\omega_0/2\pi$) and Q the quality (Q-) factor. The Q-factor is a alternative measure for the damping of the cantilever and thus also describes the ‘memory’ of the resonator. A cantilever with a large Q-factor tends to store information for a much longer time than a cantilever with a lower Q-factor[13]. A reduced Q-factor is found in water compared to air as it depends on the damping coefficient and effective mass according to (Chen *et al.*, 1994; Sarid, 1994)

$$Q = \frac{m_c \omega_0}{\gamma_c} \qquad 5.4$$

Every eigenmode of the cantilever can be described using Equations 5.2 and 5.3 with a characteristic resonant frequency and Q-factor. In Figure 5-2, the harmonic amplitude response function was fit to the first fundamental mode of an cantilever in water and found to describe the spectrum reasonably well (however, also see below).

For such a thermally excited cantilever, the SHO model allows k_c, γ_c, and m_c to be obtained either from the amplitude spectrum or more commonly from the PSD, which equals the square of the amplitude spectrum. By substituting Equations 2.2

---

[13] Thus the scan speed of SPMs can be increased using active Q-factor control (Humphris *et al.*, 2003; Humphris *et al.*, 2005).

and 5.1 into Equation 5.3 and by relating the strength of thermal energy to $k_B\ T\ \square$ (Landau and Lifshitz, 1980) the PSD can be written as

$$\left|X(\square)^2\right| = \frac{2k_B T \square_c}{\left[k_c \ \square\ m_c(2\square\square)^2\right]^2 + \square_c^2(2\square\square)^2} \qquad 5.5$$

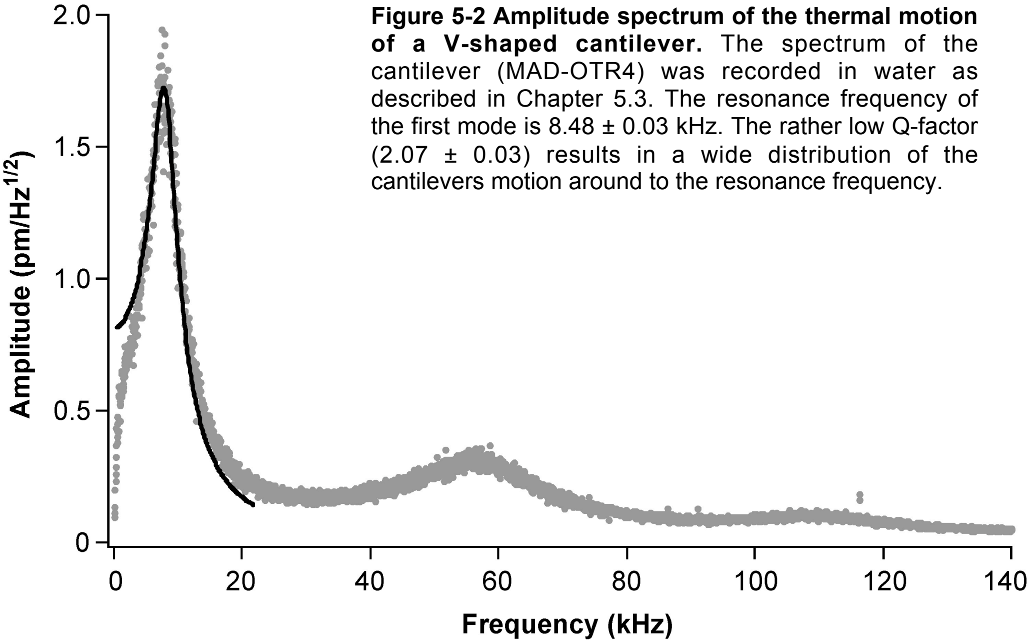

Figure 5-2 Amplitude spectrum of the thermal motion of a V-shaped cantilever. The spectrum of the cantilever (MAD-OTR4) was recorded in water as described in Chapter 5.3. The resonance frequency of the first mode is 8.48 ± 0.03 kHz. The rather low Q-factor (2.07 ± 0.03) results in a wide distribution of the cantilevers motion around to the resonance frequency.

Although the SHO model is widely used to describe the motion of AFM cantilevers, it was shown to be limited for oscillators immersed in viscous fluids. As already mentioned, the fluid moved with the cantilever lowers the Q-factor by increasing the damping and adding to the effective mass. The situation becomes complicated as the quantity of fluid involved depends on the frequency and thus the change in mass and damping are frequency dependent. The special case of an isolated oscillating sphere was already treated in the textbook by L.D. Landau and E.M. Lifshitz and later by Walters *et al.* (Landau and Lifshitz, 1987; Walters *et al.*, 1996). They showed that a sphere oscillating in water is still closely approximated by the SHO model. However, J.E. Sader has recently provided the community an analytical solution for a beam-shaped lever clamped on one side (Chon *et al.*, 2000; Sader, 1998). These studies indicated that the analogy with the SHO is only appropriate in the limit of small dissipation, or more specifically when the Q-factor is ≥ one (Sader, 1998). Although this condition is usually satisfied for experiments in air, cantilever in water have quality factors of the order of one. Therefore the SHO response function can only provide an estimate of the response of cantilevers in buffer solution. However, in the absence of a more elaborate description for V-shaped cantilevers the SHO model has been used in the following chapters.

5.2.2 Visco-elastic response of single molecules

To describe the visco-elastic properties of single molecules they were also modeled as V-K elements. Consequently, the molecule is characterized by its elasticity, k_{mol}, damping coefficient, γ_{mol}, and effective mass, m_{mol}. It is important to consider that the molecule and the cantilever act in parallel, as both are directly connected to the tip (Pethica and Oliver, 1987). This experimental situation (Figure 5-3 A) is equivalent to a more classical parallel assembly where both elements are connected to the same surface (Figure 5-3 B). As a consequence of the parallel organization, the visco-elastic properties of the molecule and cantilever are additive according to

$$k_{tot} = k_c + k_{mol} \tag{5.6}$$

$$\gamma_{tot} = \gamma_c + \gamma_{mol} \tag{5.7}$$

$$m_{tot} = m_c + m_{mol} \tag{5.8}$$

where k_{tot} is the elasticity, γ_{tot} the damping coefficient, and m_{tot} the effective mass of the cantilever-molecule system. Consequently the equation of motion of a cantilever with an attached molecule could also be written as

$$F(t) = k_{tot}x(t) + y_{tot}\frac{dx(t)}{dt} + m_{tot}\frac{d^2x(t)}{dt^2} \tag{5.9}$$

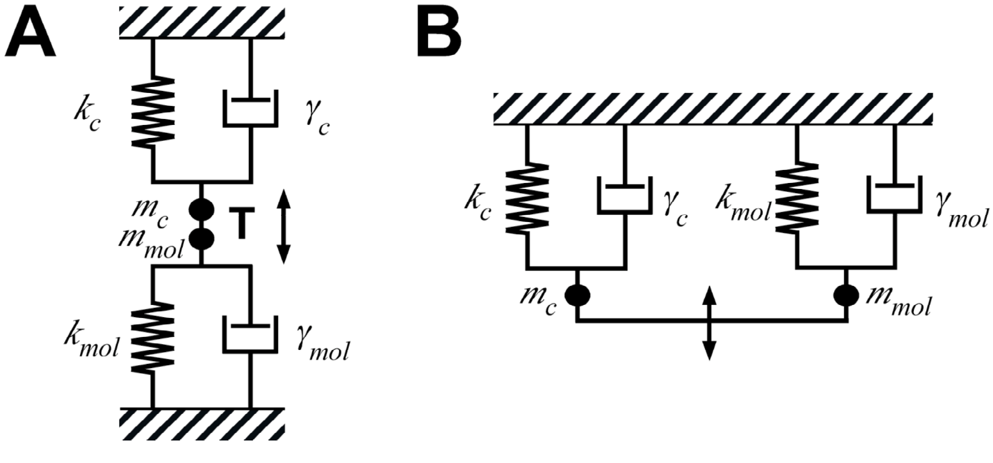

Figure 5-3 Modelling a single molecule attached to the AFM cantilever. (A) Cantilever and molecule are modelled as two V-K elements directly coupled to the tip (T). (B) Consequently, this arrangement is equivalent to more classical parallel organization where both elements are connected to the same surface.

Equations 5.6 – 5.8 directly relate the visco-elastic properties of a single molecule to the dynamic response of the cantilever-molecule system, keeping in mind that k_c, γ_c, and m_c are extracted from the motion of the free cantilever (Chapter 5.2.1). Importantly, subtracting k_c, γ_c, and m_c from k_{tot}, γ_{tot}, and m_{tot} as described in detail Chapter 5.3 also reduces hydrodynamic and surface effects (Benmouna and Johannsmann, 2002; Benmouna and Johannsmann, 2004)[14].

In the following I will introduce two different approaches to extract k_{tot}, γ_{tot} and m_{tot} from the motion of the tip. These are FMS (Chapter 5.2.3) and thermal motion spectroscopy (TMS; Chapter 5.2.4)[15]. I will focus on the elastic and viscous responses of singles molecule since a change in effective mass is usually not detected in single-molecule manipulation experiments (Kawakami *et al.*, 2004; Pethica and Oliver, 1987) and/or inertia often can be ignored (see below).

5.2.3 Force modulation spectroscopy

In FMS a sinusoidal drive signal was supplied to the AFM cantilever at an off-resonance frequency (Figure 5-4 A). Using a lock-in amplifier the amplitude, A, and phase, φ, response of the cantilever at the drive frequency was measured during conventional F-D curves. A superimposition of 15 F-D curves each recorded while unfolding a single BR and the corresponding amplitude and phase signals are shown in Figure 5-4. As in conventional force spectroscopy, the F-D curves were obtained from the quasi-static deflection of a cantilever (Figure 5-4 B). To compare the amplitude curves, each one was normalized with the free oscillation amplitude displaying a reproducible pattern among the curves (Figure 5-4 C).

From the amplitude and phase response, the elasticity and the damping coefficient of the cantilever-molecule system are obtained. Since the drive frequency, ω, is significantly below the resonance frequency of the cantilever its inertia can be neglected. To show this one firstly substitutes Equations 2.2, 5.1 and 5.4 into Equation 5.3, which yields

$$A(\omega) = \frac{F_0}{\sqrt{(k_{tot} - m_{tot}\omega^2)^2 + \omega^2 \gamma_{tot}{}^2}} \qquad 5.10$$

---

[14] Other strategies to reduce hydrodynamic interactions would be the use of cantilevers with sharp pointed tips (e.g. carbon nanotubes (Wong *et al.*, 1998)) or to approach the sample from the side such that the hydrodynamic interaction involves shear strain rather than compression (Betzig *et al.*, 1992).

[15] Other approaches to measure visco-elastic properties include frequency modulation at resonance (Gotsmann *et al.*, 1999) or transverse dynamic force microscopy (Humphris *et al.*, 2002).

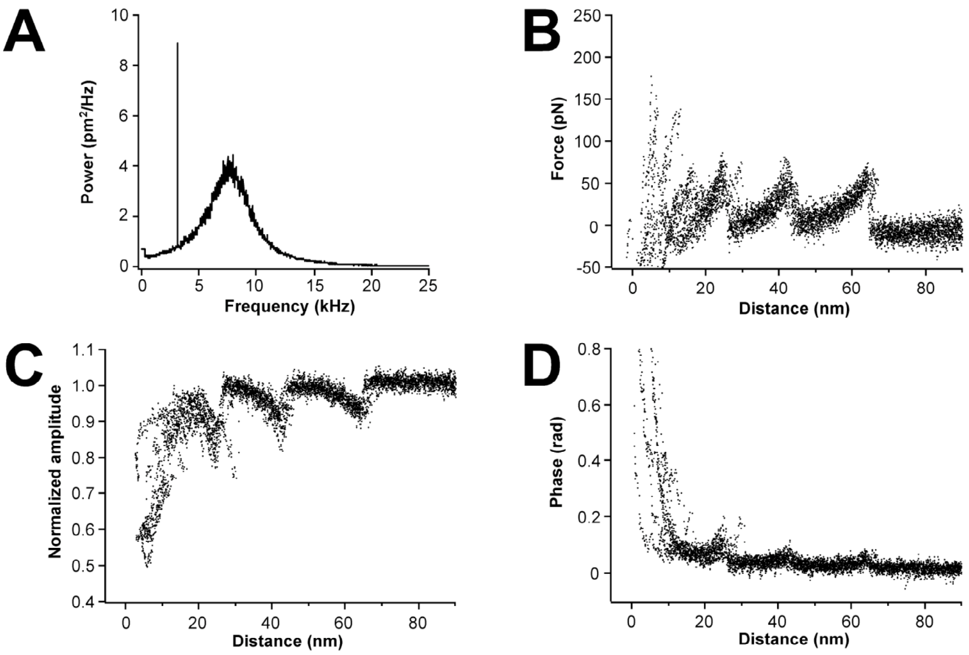

Figure 5-4 FMS of single BRs. (A) PSD with off-resonance excitation. The spectrum shows the typical thermal peak around the resonance frequency (≈ 8 kHz) and a spike at the off-resonance excitation frequency (3 kHz). (B) Superimposition of 15 F-D curves each recorded while unfolding a single BR molecule. The overlaid curves show a reproducible unfolding pattern similar to that observed in conventional unfolding experiments of BR (Chapter 3). (C and D) Application of a small oscillation to the cantilever allows the measurement of the molecular amplitude (C) and phase (D) response. The amplitude and phase curves were superimposed with the same distance offsets as the corresponding F-D curves.

If ω is much smaller than $\omega_0 = \sqrt{\frac{k_{tot}}{m_{tot}}}$, then $\left(\frac{\omega}{\omega_0}\right)^2 << 1$ and consequently $\frac{m_{tot}\omega^2}{k_{tot}} << 1$. Thus inertia can be ignored and Equation 5.10 can be simplified to

$$A(\omega) = \frac{F_0}{\sqrt{k_{tot}{}^2 + \omega^2 \gamma_{tot}{}^2}} \qquad 5.11$$

Accordingly, the phase of the oscillation can be simplified from (Chen *et al.*, 1994; Sarid, 1994)

$$\tan\varphi = \frac{\gamma_{tot}\omega}{(\omega_0{}^2 - \omega^2)m_{tot}} \qquad 5.12$$

to

$$\tan\varphi = \frac{\gamma_{tot}\omega}{k_{tot}} \qquad 5.13$$

From rearranging Equation 5.12 and 5.13 we finally obtain

$$k_{tot} = \frac{F_0}{A}\frac{1}{\sqrt{1+\tan^2\varphi}} \qquad 5.14$$

and

$$\gamma_{tot} = \frac{k_{tot}\tan\varphi}{\omega} \qquad 5.15$$

Equation 5.14 allows the elasticity and Equation 5.15 the damping constant of the cantilever-molecule system to be determined in terms of the drive force. By defining the phase response of the system zero when the cantilever is oscillating free above the surface the drive force is calculated following

$$F_0 = A_0 k_c \sqrt{1+\tan^2\varphi} = A_0 k_c \qquad 5.16$$

where A_0 denotes the free peak oscillation amplitude. Since the analysis showed the inertia can be ignored, only the elasticity and damping of the cantilever-molecule system are analyzed.

5.2.4 Thermal motion spectroscopy

In TMS the complete frequency response of a thermally excited cantilever is obtained in terms of the PSD. As shown in Figure 5-5, the first step in the analysis is to record an over-sampled F-D curve of the unfolding of the protein (Figure 5-5A).

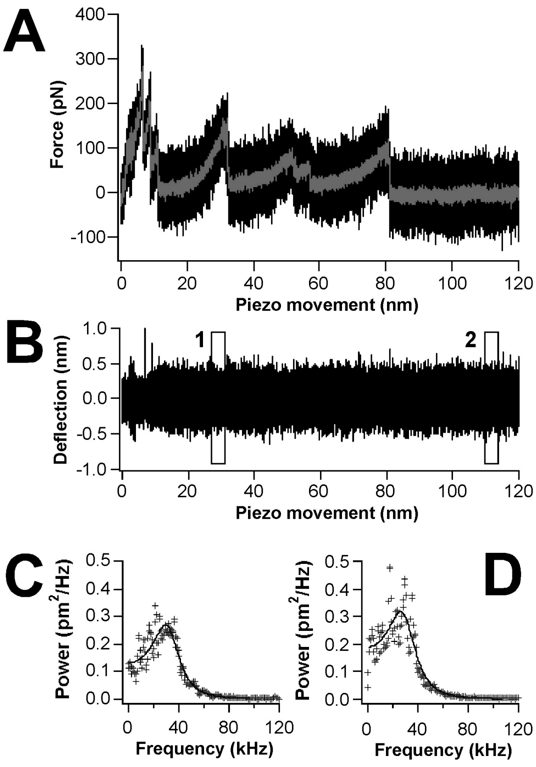

Figure 5-5 Analysis of thermal cantilever motion in a force-extension experiment. (A) F-D curve recorded on a single BR molecule with a novel small cantilever (Toda *et al.*, 2004). The gray line shows the same curve after smoothing. (B) Deflection signal of the F-D curve shown in A after hi-pass filtering with a cut-off frequency of 400 Hz. As examples, the analysis of two segments (marked 1 and 2) is shown in C and D. (C and D) PSDs calculated from the cantilever deflection in segment 1 (C) and segment 2 (D). The PSDs are well described by fitting by Equation 5.5 (solid lines) and reveal the visco-elastic properties of the molecule at that specific instance.

Then the Brownian cantilever motion is extracted from the curve using hi-pass filtering (Figure 5-5 B). In a next step the curve is divided into small windows and for each window the thermal noise PSD is calculated (Figure 5-5 C and D). Using Equation 5.5 the first fundamental mode in the PSD is analyzed and k_{tot}, γ_{tot}, and m_{tot} are determined. Although it was recently suggested to analyze of the frequency response of the excited cantilever (Kawakami *et al.*, 2005), it is desirable to work with a thermally excited cantilever since it oscillates with much smaller amplitudes.

5.3 Experimental procedures

Sample preparation

Native PMs were adsorbed to freshly cleaved mica as described in Chapter 3. Experiments were performed in 300 mM KCl, 20 mM Tris, pH 7.8.

AFM instrumentation

A commercial AFM (PicoForce or Multimode, di-Veeco) was extended with a PC equipped with 16-bit data acquisition electronics (6052E, National Instruments, Munich). Force spectroscopy was performed as described in Chapter 3 at 91 nm/s pulling speed in case of FMS and at 160 nm/s pulling speed in case of TMS. The spring constants and resonance frequencies of the silicon nitride or silicon cantilevers (short thin-legged NP-S, di-Veeco: k_c ≈ 0.26 N/m, v_{res} ≈ 10 kHz, l ≈ 115 μm, w ≈ 25 μm, t ≈ 0.6 μm; “Mini BioLever” BL-AC40TS, Olympus, Tokyo, Japan: k_c = 0.117 - 0.190 N/m, v_{res} ≈ 30 kHz, l ≈ 38 μm, w ≈ 16 μm, t ≈ 0.2 μm (Toda *et al.*, 2004); MAD-OTR4, di-Veeco or LOT-Oriel, Darmstadt: k ≈ 0.08 N/m, v_{res} ≈ 7 kHz, l ≈ 100 μm, w ≈ 15 μm, t ≈ 0.4 μm) were calibrated in buffer using thermal fluctuation analysis (Chapter 2.4).

FMS

For FMS, the AFM was equipped with a magnetic cantilever actuation system (di-Veeco; Figure 5-6) and 100 μm long magnetically coated silicon nitride cantilevers (MAD-OTR4, see above). Magnetic excitation Han *et al.*, 1996; Lindsay *et al.*, 1993, as well as other direct excitation methods Enders *et al.*, 2004; Rogers *et al.*, 2002, enable the drive signal to be directly related to the drive force and thus to the response of the cantilever. In addition, a substantial signal to noise advantage may be obtained if the tip is directly oscillated (Han *et al.*, 1996; Lindsay *et al.*, 1993) as opposed to indirect mechanical excitation with an acoustic transducer (Putman *et al.*, 1994; Schäffer *et al.*, 1996). To reduce contributions of 1/□ noise, the cantilever was oscillated at an off-resonance frequency of 3 kHz with free peak-to-peak amplitudes between 6 and 9 nm. The deflection signal was analyzed with a lock-in amplifier with 1 ms time constant (SR830DSP, Stanford Research Systems, Sunnyvale, CA, USA). The X- and Y-channels and the deflection of the cantilever were recorded with the external data-acquisition electronics and Labview software (National Instruments, Munich) at a sampling rate of 11.6 kHz. The X- and Y-channels were analyzed using Igor Pro to yield the amplitude and phase according to $A = \sqrt{X^2 + Y^2}$ and $\tan\square = YX^{\square 1}$. Except for the quasi-static F-D curves and the superimpositions, no smoothing was applied.

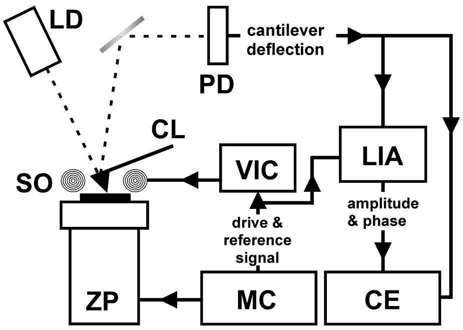

Figure 5-6 FMS instrumentation. An AFM with an optical detection system (photodetector, PD; laser diode, LD; piezoelectric actuator, ZP) was equipped with magnetically coated cantilevers (CL) and a solenoid (SO). The solenoid was driven by a voltage-current converter (VIC) connected to the sinusoidal drive signal from the microscope controller (MC). The cantilever deflection was analyzed in a lock-in amplifier (LIA) to separate amplitude and phase of the oscillation. Amplitude, phase and deflection were recorded with external capture electronics (CE).

To obtain the molecular visco-elastic response according to Equations 5.6 – 5.8, the visco-elasticity curves recorded during surface approach were replaced by line fits and subtracted from the corresponding visco-elasticity curves recorded during surface retract.

Each F-D curve was reconstructed by integrating the corresponding amplitude curve using a custom macro written in Igor Pro. For the peak finding routine (Chapter 5.4.4), the amplitude curves were integrated in a 4 nm window sliding over the curves with 0.4 nm steps. By subtracting the measured F-D data (Figure 5-11 A, gray line) from the reconstructed F-D data (Figure 5-11 A, solid lines) a difference curve was calculated and compared to the force threshold for each step (Figure 5-11 B, solid lines).

TMS

For TMS, the deflection signal was first low-pass filtered at 100 kHz with a hardware filter to avoid anti-aliasing and then digitized at 300 kHz sampling rate using Igor Pro. Deflection curves were analyzed using custom macros and built-in features of Igor Pro. The curves were first hi-pass filtered at 400 Hz (also to reduce contributions of 1/f noise) and then divided into windows. Each window was processed by calculating the PSD with 512 point hanning-type windows and fitting the PSD with Equation 5.5. Calculation and fitting of the PSD was independently double-checked using the thermal tune function of the AFM and the Origin software (Northampton, MA, USA). The molecular visco-elastic response was obtained as described for FMS.

5.4 Results and discussion

5.4.1 Signal-to-noise ratio and time resolution

In the preceding chapters, I have introduced FMS and TMS as two techniques to measure the visco-elastic properties of single molecules. In this first part of the discussion I will compare the signal-to-noise (S/N) ratio and the time resolution of these approaches. To estimate the S/N ratio I have analyzed F-D curves where no molecule had attached to the tip. These curves where treated as a time series in a tip-sample distance range between 0 and 160 nm to derive the peak noise when determining elasticities, Δk_c, and damping coefficients, $\Delta\gamma_c$[16]. From Figure 5-7 it becomes clear that there is no significant dependence of the elasticity and damping coefficient in this range of tip-sample distances, which would influence the calculation of the noise. In a next step, the apparent S/N ratio was determined from the ratio of the expected signal and the peak noise. For the expected signals I used the slopes of the F-D curve near the force peak of a typical BR peak (k_{mol} = 25 pN/nm; Figure 3.6) and the damping of a single dextran molecule (γ_{mol} = 0.2 μNs/m; Kawakami *et al.*, 2005).

For FMS, the analysis showed that the experiments will offer a S/N ratio of ≈ 9.6 when determining the elasticity (Figure 5-8 C) and ≈ 9.7 when determining the damping coefficient of a single molecule (Figure 5-8 D). The application of the lock-in technique might be the key to the good S/N ratio, since thermal fluctuations of the cantilever at all frequencies apart from the modulation frequency are excluded (Hoffmann *et al.*, 2001). Remarkably, this sensitivity is achieved with a very good time resolution of 1 ms, which is determined by the time constant of the lock-in amplifier and thus could be further optimized. However, adjusting the time constant of the lock-in amplifier is always a trade-off between time resolution and allowing sufficient oscillations per sampling period (here ≈ 3.3 oscillations were analyzed per sampling period; also see Chapter 7.3).

---

[16] Here, the peak noise was found to give a more sensible measure for the noise in the curves than the RMS noise.

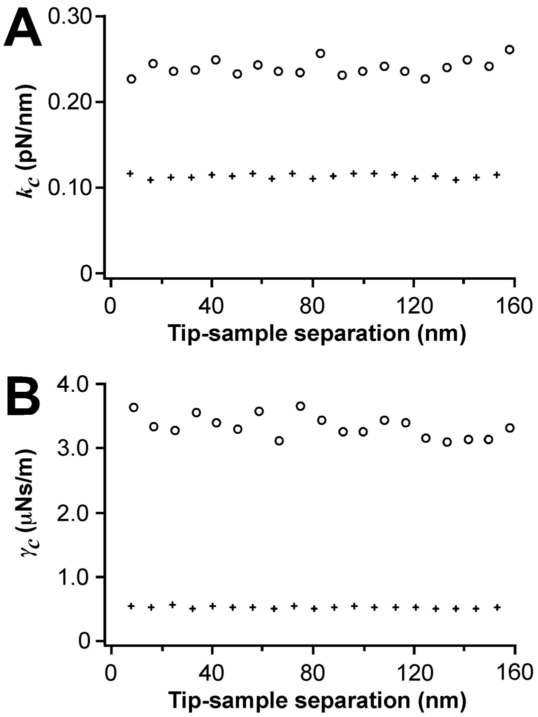

Figure 5-7 Distance dependent noise measurements. The elasticity (A) and damping coefficient (B) of the regular cantilever (circles) and the small cantilever (crosses) are shown as a function of the tip-sample distance. In this range of tip-sample distances, the regular cantilever (small cantilever) had a spring constant of ≈ 0.25 N/m (≈ 0.12 N/m) and damping coefficient of ≈ 3.5 μNs/m (≈ 0.25 μNs/m). Such empty F-D curves were analyzed to measure the peak noise of the cantilever. The exemplary curves shown here were determined using TMS and a window size of 50 ms. The same empty curves were collected with FMS (not shown). The magnetic cantilever had a spring constant of ≈ 0.09 N/m and the damping coefficient ≈ 3 μNs/m.

In TMS the peak noise in the elasticity and damping coefficient critically depend on the size of the windows the curves were divided into. Increasing the window size increased the time period available to calculate the frequency components of the motion of the cantilever and thus resulted in smaller noise and consequently a better apparent S/N-ratio. Importantly the noise and S/N-ratio critically depended on the type of cantilever used. Two types of cantilevers were tested which differed in their size, spring constants, and resonance frequencies (see Chapter 5.3). Choosing a small cantilever with high resonance frequency (≈ 30 kHz in buffer) significantly improved the S/N ratio in the measurements. While both cantilevers had similar performance in measuring the elasticity (Figure 5-8 A and C), only the smaller cantilever offered a sufficient S/N-ratio to resolve the damping coefficients (Figure 5-8 B and D). One probable reason for the better S/N-ratio of the small cantilever is its significantly higher resonance frequency. However, other size-dependent effects must be responsible for the drastic difference in the S/N-ratio when determining the damping coefficients.

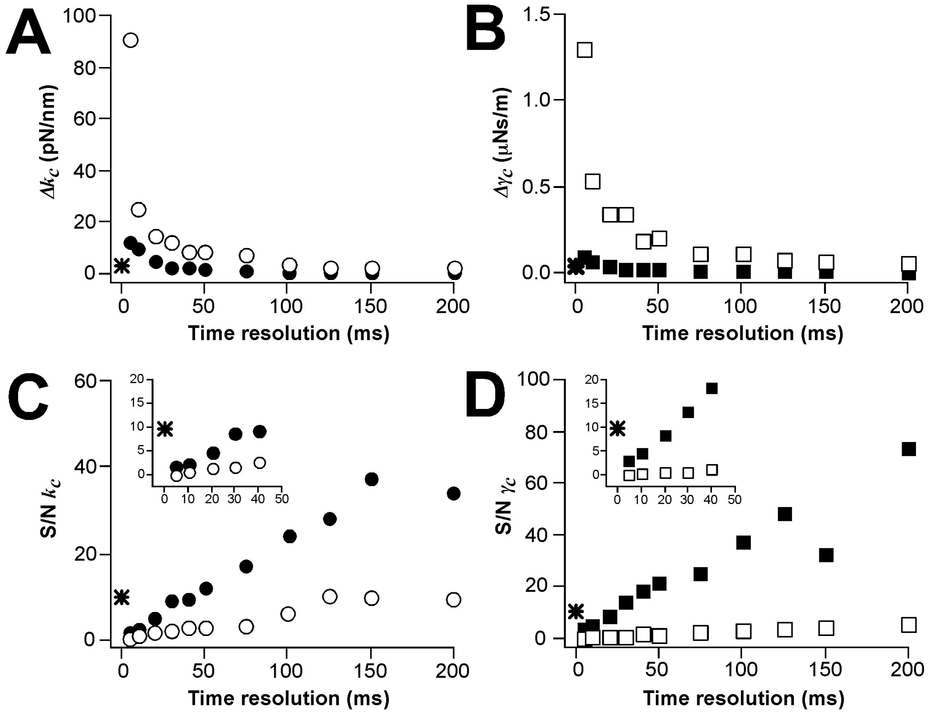

Figure 5-8 S/N-ratio of FMS and TMS as a function of time resolution. The peak noise in elasticity (A) and damping (B) measurements is shown as a function of the time resolution. The FMS data are represented by a star, while the TMS data are shown as open (regular cantilever) and full symbols (small cantilever). The time resolution is either defined by the time constant of the lock-in amplifier (in case of FMS) or the size of the window (in case of TMS). (C and D) The apparent S/N ratio was calculated using the expected peak elasticity and damping (k_{mol} = 25 pN/nm, γ_{mol} = 0.2 µNs/m) and the noise values from A and B. From C it becomes clear that FMS offers a sensible S/N ratio at a time resolution of 1 ms. For TMS, increasing the time period available for monitoring the cantilever motion reduces the noise. While both cantilevers showed similar performance in elasticity measurements (C), the damping information could only be extracted from the small cantilever measurements (D).

From these data one can immediately conclude that FMS is the method of choice if one is interested in the detection of short-lived intermediates (Figure 5-6 C and D, insets). The S/N ratio of TMS improves with increasing sampling time and a similar S/N ratio as with FMS is achieved with a time resolution of ≈ 30 ms. However, a sampling period of 30 ms appears to be very long if one studies molecular interactions in F-D measurements. Even at a relatively slow pulling speeds of 66 nm/s, one would only obtain ≈ one datapoint per two nm or ≈ 30 datapoints for a whole BR molecule. Nevertheless, TMS can be a very useful technique to study events with a relatively long life-time, especially as it is technically much easier to be realized compared to FMS.

5.4.2 Visco-elastic properties of single bacteriorhodopsins

Figure 5-9 summarizes the application of FMS (A-C) and TMS (D-F) to single BR molecules. In Figure 5-9 A and D, the F-D curves are shown while Figure 5-9 B, C, E, and F show the corresponding elasticities and damping coefficients. As expected from the analysis in the last chapter, only FMS allows resolving the stiffness and damping coefficient of single BR molecules. However, the stiffness of the first few unfolding intermediates is also detected in TMS, most probably as the very short peptide is sufficiently stiff to give a resolvable peak. Nevertheless, I will focus on the more sensitive FMS data in the discussion.

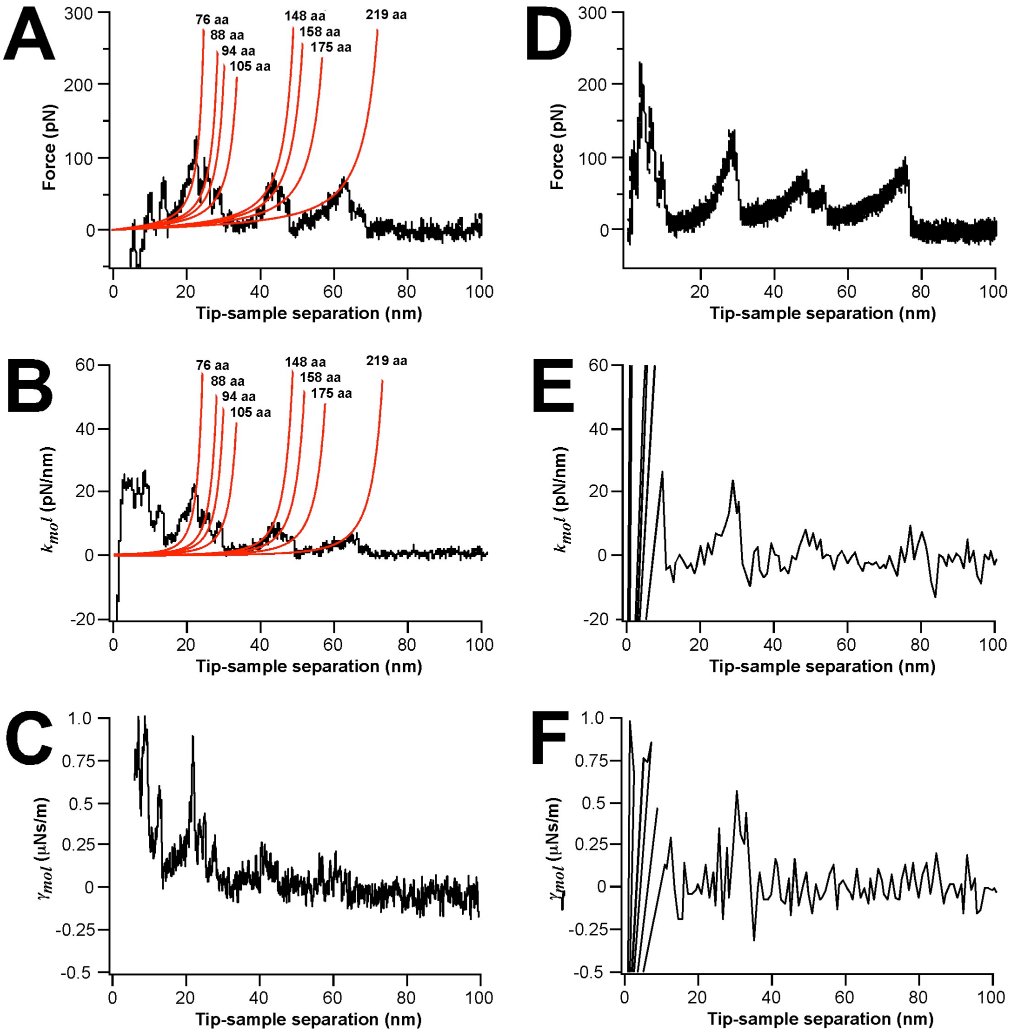

Figure 5-9 Elastic and dissipative response of BR. The elasticity and the damping coefficients of single BRs were determined using FMS (A-C) and TMS (D-F). (A and B) F-D curves recorded during unfolding of individual BRs. (C and D) Elastic response during the extension of the unfolded parts of BR. Solid lines in C are fits with the derivative of the WLC model (Equation 5.17). (E and F) Discrete events are observed in the damping of the molecules. For TMS the window size was adjusted such that ≈ one datapoint per nm is obtained.

For an interpretation of the elastic component one needs to recall from Chapters 2 and 3 that the characteristic saw-tooth pattern in the F-D curves stems from the mechanical extension of already unfolded secondary structure elements. As the force extension relationship of polypeptides can be well described using the WLC model, the elasticity curve should obey the derivative of Equation 2-11 with respect to distance that can be written as (Kienberger *et al.*, 2000; Marko and Siggia, 1995)

$$\frac{dF(d)}{dd} = \frac{k_B T}{l_p L}\left[0.5\left(1-\frac{d}{L}\right)^{-3}+1\right] \qquad 5.17$$

Figure 5-9 B shows that the peaks in the elasticity curve are well described by Equation 5.17 using the indicated number of aas and the same persistence and monomer lengths as for the F-D curve. The good agreement between the experimental curve and the predicted elasticity pattern verified that such a typical unfolding spectrum is dominated by the purely elastic extension of unfolded polypeptides (also see Chapter 5.4.4). From Figure 5-9 it then becomes clear that the peak stiffness of the extended polypeptide fragments was of the order of a few ten pN/nm.

Discrete events were also observed in the dissipative response of the molecules (Figure 5-9 C and F). However, their interpretation is more difficult than for the elastic response. The positions of the peaks suggest that they are associated with the unfolding of the secondary structure elements. This hypothesis agrees well with the finding that the extension of the unfolded polypeptide fragments is mostly elastic. Surprisingly, the dissipative interactions decrease strongly after the first force peak occurring at a tip-sample distance of ≈ 28 nm (Figure 5-9 C). This indicates, that the unfolding of the first few α-helices disrupts the tertiary structure of the protein and therefore lowers the dissipative interactions when unfolding the remaining α-helices. However, dissipation is measured for all α-helices of BR in agreement with experimental observations that individual α-helices are folded in the membrane bilayer (Chapter 1.2.2). Since the damping coefficient directly relates to the energy dissipated during unfolding, the measurements provide novel insights into the sequential unfolding of the secondary structure elements. However, from Figure 5-9 C and F it becomes clear that additional experiments with an improved S/N ratio will be required to obtain more precise pictures of the energy dissipation events (also see Chapter 7.3). In addition, the off-equilibrium nature of the measurement has to be considered if one is interested in equilibrium unfolding energies. However, the underlying principles to do so are not completely understood and focus of current research (Gore *et al.*, 2003; Hummer and Szabo, 2005).

5.4.3 Uncovering new unfolding intermediates

Surprisingly, the F-D curves obtained in FMS locally differed from those collected in conventional force spectroscopy. To compare the curves recorded in the two types of experiments, a peak finding algorithm developed by M. Kuhn (MPI-CBG, Dresden) was applied to 60 FMS and 300 conventional F-D curves. This analysis revealed the appearance of three new force peaks in the FMS F-D curves. These events are located at 76 aa, 125 aa, and 195 aa extension lengths, observed in 53.3% (75 aa), 43.3% (125 aa) and 45% (195 aa) of the curves and of comparable intensity as the other peaks (50 – 80 pN) (Figure 5-10). In the following, two possible explanations for the appearance of new force peaks in FMS curves are discussed.

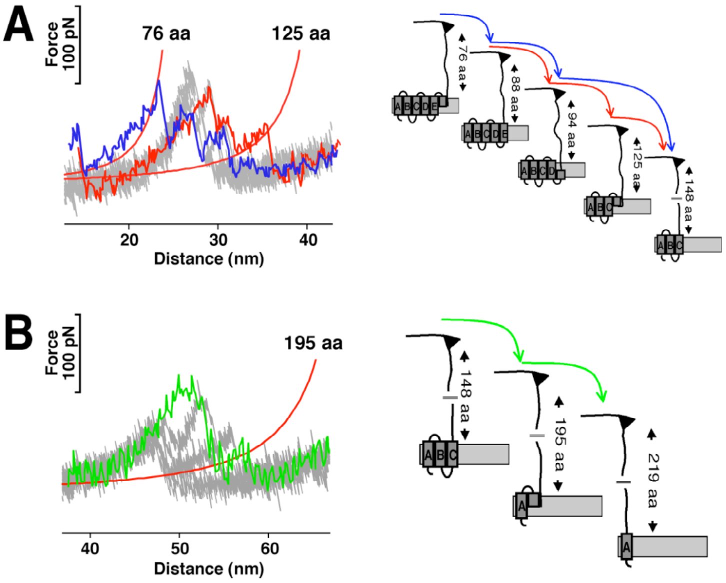

Figure 5-10 FMS reveals new unfolding intermediates. In the left frames the curves from the conventional pulling experiment are shown in gray, while individual FMS F-D curves are overlaid. The selected curves show the three new unfolding peaks each of which was detected in ≈50% of all curves. Fitting these peaks with the WLC model showed that they correspond to the extension of 76, 125 and 195 aas. As discussed in detail in Chapter 3, the positions of force peaks allow localizing the unfolding barriers in the structure of the protein (right frames).

Firstly, these events could correspond to previously inaccessible unfolding intermediates of BR. It should be noted that in the FMS experiments described here the pulling speed and therefore the loading rate applied to the transmembrane α-helices is not comparable to quasi-static measurements. Due to the oscillatory movement of the cantilever, tip velocities as high as ≈ 15 μm/s are reached both, towards and away from the direction of the quasi-static pulling force. However, the tip velocity will decrease and eventually reach zero as the tip approaches the maximum deflection during each oscillation. In Chapter 3.4.5, I showed that the detection of unfolding intermediates in BR depends on the pulling velocity and an increased velocity leads to the observation of a greater number of intermediates. Therefore, one could conclude that the oscillatory movement of the cantilever reveals new mechanical unfolding pathways in the energy landscape of the protein. In this scenario, the data suggests that stable intermediates are formed by the upper halves of α-helices F, D and B, which remain folded even after the lower halves of these α-helices were unfolded (Figure 5-10 A and B, right frames). As proposed earlier for α-helix E of BR and Halorhodopsin (Cisneros *et al.*, 2005), α-helices F, D and B obviously can follow two different unfolding pathways, in one of which they do not undergo cooperative unfolding.

For a different interpretation, it is important to consider that the quasi-static deflection of the cantilever (1 nm) is relatively small compared to the cantilever oscillation amplitude (3-5 nm peak-to-peak during polypeptide extension). Thus, 11 aa (4 nm) long unfolded polypeptide segments will be periodically relaxed towards the membrane surface and thereby eventually refold or aggregate. This scenario seems to be less probable than the first one, as new force peaks are only and reproducibly detected at three well-defined positions. In addition, the cantilever often does not fully relax after an unfolding event. This results in a small but maintained force applied to the polypeptide, which may prohibit recoiling or refolding.

Finding a structural explanation for the unfolding intermediates is not straightforward, especially as molecular dynamics simulations of the forced unfolding of BR are not available. However, the positions of the intermediate detected in α-helices B and F (Figure 5-10) correlate very well with the kinks of these α-helices. Like many α-helices of other membrane proteins, α-helices B and F are tilted and exhibit kinks centered at proline residues 50 and 186 respectively. To learn about the structural importance of these residues, the group of J. Bowie replaced them with alanines (Faham *et al.*, 2004; Yohannan *et al.*, 2003). Surprisingly, the thermal stability of BR was not altered by these mutations, nor was the proteins structure significantly affected. Thus, it was concluded that the kinks of wild type and mutant α-helices originates from cumulative interactions of surrounding residues rather than the presence of prolines. Here, the oscillatory F-D curves indicate that the kinks are responsible for the detection of two unfolding intermediates for each of these two α-helices and suggest that they reduce their unfolding cooperativity of the α-helices.

5.4.4 Resonstructing F-D curves: A novel approach to detect unfolding events

Besides its high sensitivity another major advantage of FMS is the availability of independently recorded amplitude and phase signals. As an example, I will show that the reconstruction of F-D curves by integrating amplitude curves offers an alternative technique to detect force events. In the absence of dissipation, a change in interfacial stiffness, $S(d)$, is detected by the cantilever as a change in oscillation amplitude. Under the assumption that the oscillation amplitude is small, the interfacial stiffness can be written as

$$S(d) = k_c\left(\frac{A_0}{A(d)} - 1\right) \qquad 5.18$$

where A_0 denotes the free oscillation amplitude and $A(d)$ is the amplitude as a function of tip-sample distance (Lantz *et al.*, 1999; Liu *et al.*, 1999). Integrating Equation 5.18 yields Equation 5.19 and thus the possibility to recalculate F-D curves from amplitude curves.

$$F(d) = -k_c \int \left(\frac{A_0}{A(d)} - 1\right) dd + C \qquad 5.19$$

In Equation 5.19, the constant C denotes the force at the point where the integration was started. Figure 5-11 shows that the reconstructed F-D curve is in excellent agreement with the measured curve in regions of elastic polypeptide extension (also compare to Chapter 5.4.2).

From Figure 5-11 A and Equation 5.19 it is also apparent that the reconstruction will not be successful in regimes where the slope of the F-D curves is negative as the integral of the amplitude is always positive (Lantz *et al.*, 1999; Liu *et al.*, 1999). Thus, a disagreement between measured and reconstructed data can be used to identify unfolding events as, in these cases, the force decreases with displacement. This approach is intrinsically different from the conventional peak detection routines, where smoothed curves are searched for local maxima and minima (e.g., see Kuhn *et al.*, 2005). As described in more detail in Chapter 5.3, the approach has been applied to detect peaks in FMS curves recorded on BR. All previously detected and the three new peaks could be localized. Figure 5-12 shows one exemplary curve.

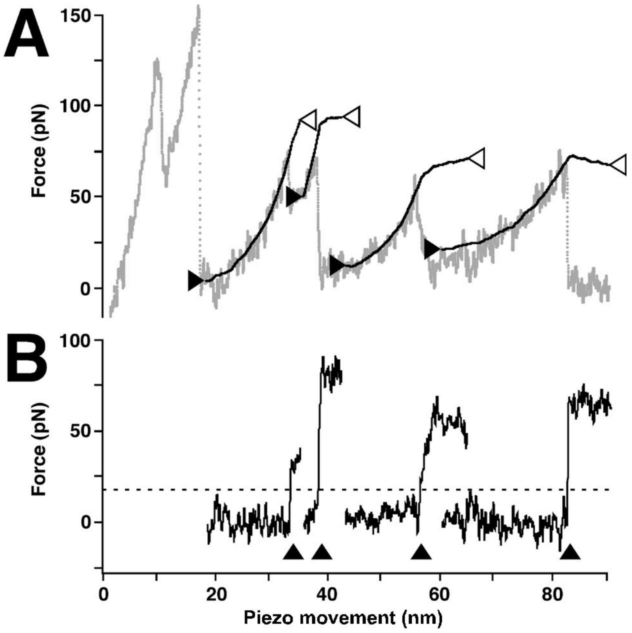

Figure 5-11 Reconstruction of a F-D curve. (A) An experimental F-D curve (gray line) was reconstructed from the corresponding amplitude curve in several segments (solid black lines flanked by two arrowheads). The X-position of the arrowheads corresponds to the point where the integration of each segment was started (full arrowheads) or stopped (open arrowheads). Consequently, the Y-positions of the full arrowheads correspond to the constant C in Equation 5.19 for each segment. Excellent agreement between reconstructed and measured data is obtained for areas of elastic polypeptide extension, while no agreement was observed if the reconstruction was performed over force peaks. (B) For each segment, a difference curve was calculated by subtracting the measured data from the reconstructed data. The poor overlap between reconstructed and measured data leads to a sudden increase in the difference curve (arrowheads), which can be used to detect unfolding events in F-D curves. The dashed line represents the force threshold of 20 pN used in the automated peak detection routine.

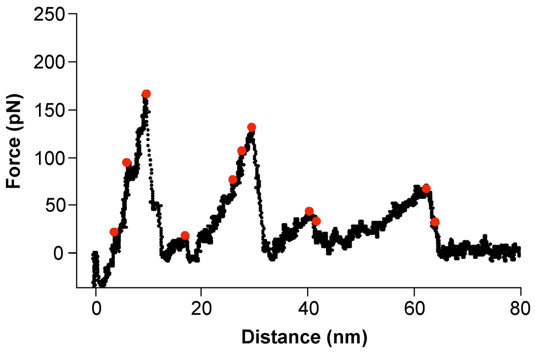

Figure 5-12 Typical result of the peak finding routine. The red dots on the FMS F-D curve indicate positions where the integration routine localized force peaks. For the detection routine, a force threshold of 20 pN was used (dashed line in Figure 5-11 B).

5.5 Conclusions

The past decade has seen a dramatic increase in our understanding of the mechanical properties of biological macro-molecules and their fundamental role in many biological processes (for a recent review, see Bustamante *et al.*, 2004). In single-molecule force-extension experiments, researchers have been studying the elastic properties of a wide class of bio-molecules in response to external pulling forces (Abu-Lail and Camesano, 2003; Hansma *et al.*, 2004; Janshoff *et al.*, 2000; Rief and Grubmüller, 2002). Here, I have presented two extensions to the existing AFM force spectroscopy experiments, which allow measuring the complex visco-elastic response of single (bio-)molecules.

In FMS, a small vertical oscillatory motion was supplied to the tip of the cantilever, while in TMS the thermal noise of the cantilever was analyzed during conventional force spectroscopy experiments. In both cases, the cantilever and molecule were modeled as two V-K elements acting in parallel and the two methods were shown to give similar results. However, FMS offers a much higher sensitivity than TMS. In addition, the FMS approach has a time resolution of only 1 ms, which is at least one order of magnitude faster than TMS. This highlights that FMS is the method of choice for the sensitive detection of the dynamic properties of short-lived intermediates, while TMS is a technically simple approach suitable to study relatively long phenomena.

Using the more sensitive FMS approach, I was able to measure the dynamic response of single BR molecules. For the elastic component, FMS provided a direct and continuous measurement of the stiffness of the single polypeptide strands. Also, the damping associated with the unfolding of single α-helices could be measured. In addition, I showed that FMS can uncover novel mechanical unfolding intermediates in single proteins. In particular, I found that the α-helices of BR do not always follow a cooperative unfolding pathway and that kinks result in reduced unfolding cooperativity of the α-helices. This highlights that the method provides a more detailed picture of a protein's mechanical energy landscape. Importantly, the reconstruction of F-D curves from amplitude curves offers a novel approach to detect mechanical unfolding intermediates.

6. General conclusions

The folding and stability of membrane proteins is a fundamental and long-standing biological problem. Historically, the study of membrane proteins has been hindered by experimental difficulties associated with the anisotropic environment of the lipid bilayer. In many cases, solubilizing high yields of stable and functional proteins and their reconstitution into lipid bilayers have proven to be non-trivial. In addition, the (thermodynamic) stability of membrane proteins is still not well characterized, as they cannot be denatured to completely unfolded sates using chemical agents or temperature. Thus it is not surprising that relatively little experimental information about the interactions stabilizing membrane proteins exist, particularly if compared to water-soluble proteins. In addition conventional (un-)folding techniques only probe the average behavior of large numbers of molecules. Consequently novel investigative approaches are required to observe co-existing (un-)folding pathways and non-accumulative intermediates, which may be populated in the multidimensional folding landscapes of single-molecules.

Here, I presented single-molecule measurements of the stability of the membrane protein BR. Individual BRs were unfolded and extracted from their native membranes using the cantilever of an AFM as a nanomanipulator. In these mechanical unfolding experiments, an external pulling force played the role of the denaturant and lead to unfolding of the three dimensional structure of single proteins. Remarkably single BRs unfolded step-wise in a sequence of multiple stable intermediates. In the majority of the cases, these well-defined unfolding intermediates corresponded to single secondary structure elements of the protein. In addition I found that individual BR molecules can choose between different unfolding pathways in a complex energy landscape. Although single α-helices were sufficiently stable to unfold in individual steps they also exhibited a certain probability to unfold in pairs. The observation that single α-helices are stable in the membrane strongly supports the two-stage model of membrane protein folding, where the α-helices act comparably to the domains of water-soluble proteins and form folding intermediates. Interestingly the probability for individual α-helices to unfold in pairs depended on the rate of the applied force. These data suggest that α-helices prefer a pairwise association at equilibrium and are in line with the helical hairpin motif, which has been shown to be important during the folding of membrane proteins.

Dynamic force measurements provided detailed insights into the energy landscape of the individual secondary structure elements. These experiments showed, that single □-helices and helical hairpins were stabilized by sharp energy barriers, which had a width of □10% of the length of the helical structures. This indicated that only small extensions of □ 5 Å were sufficient to break these relatively rigid structural elements, most probably as the starting point of a cooperative unzipping process. The stability of single □-helices was determined to be of the order of 100 s, which seems to be sufficient for assembly during the folding process.

Single-molecule force measurements are still a relatively young technique with a lot of untapped potential for important methodological improvements. In this thesis I complemented the conventional forced unfolding experiments with the development of new approaches to study the mechanical properties of single molecules. In Chapter 4, I have demonstrated that hydrodynamic effects need to be considered in fast single-molecule force measurements. Such fast measurements are desirable to obtain more complete kinetic pictures of single molecules. In chapter 5, I presented two force measurement techniques which allow the complex visco-elastic response of single (bio-)molecules to be determined. Using the more sensitive of these techniques I was able to uncouple the elastic and viscous response of single BR molecules. For the elastic component, I showed that the unfolding patterns are dominated by purely elastic extension of unfolded polypeptide fragments and a direct and continuous measurement of their stiffness was presented. Also, the damping associated with the unfolding of single □-helices could be measured, which relates to the dissipated energy. In addition, I showed that more mechanical unfolding intermediates of single proteins can be uncovered if a small oscillation amplitude is supplied to the cantilever. In particular I found that kinks result in a reduced unfolding cooperativity of transmembrane □-helices.

In summary these results show that single-molecule force measurements are a valuable tool to study the stability and mechanical properties of membrane proteins. In the near future, these and more advanced force measurement techniques will provide an even more detailed picture at which instances individual interactions contribute to the complex mechanisms of membrane protein folding and assembly.

7. Outlook

7.1 Hidden complexity in the forced unfolding of single proteins

In preceding chapters, I have introduced the AFM as a valuable tool to study the stability of single water-soluble and membrane proteins. I found that membrane proteins unfold in a well-defined sequence of several partly unfolded intermediates and described their energy landscapes. Until now we and others (e.g., see Dietz and Rief, 2004; Li *et al.*, 2005; Marszalek *et al.*, 1999) assumed that the unfolding transitions of these intermediates largely occur independently from each other. One will have to test this hypothesis in future experiments for a deeper understanding of the energetic properties of single proteins.

As an example, I have evaluated the unfolding forces of two intermediates in BR. Since a comparison of absolute forces is sensitive to inevitable errors in force calibration[17], I propose an alternative analysis approach based on force ratios. Here, I define force ratio as the normalized unfolding force of the second intermediate (e.g. α-helix D) obtained by dividing it by the unfolding force of the first intermediate (e.g. α-helix E) for each protein. This approach yields a population of force ratios near 1 and is insensitive to errors in force calibration[18]. An easy yet powerful way for analyzing this population is to compile it as a histogram since this allows immediate access to the distribution of the force ratios. Figure 7-1 A shows the force ratio histogram for α-helix D and E compiled from unfolding data of native (trimeric) BR. Three peaks are visible in the histogram, which can be well described with Gaussian fits. This indicates that, in trimeric BR, α-helices E and D co-exist in three distinct states, which differ in the relative strength of the α-helices. Surprisingly this is not observed in data obtained from M-C simulations (Figure 7-1 A, inset) or experimental data recorded monomeric BR (Figure 7-1 B). In latter cases, α-helices E and D unfold at a fixed force ratio as indicated by a single peak in the histograms.

These results suggest the presence of substantial hidden information in forced unfolding experiments of single proteins. Therefore it seems advisable to perform the suggested force ratio analysis in addition to DFS, FMS and temperature dependent force measurements. For BR, more detailed studies using different types of molecular assemblies and proteins with point mutations are required to determine the origin of the molecular interactions stabilizing the three co-existing states.

---

[17] Due to uncertainties in spring constant calibration (Chapter 2.4), unfolding forces measured in the same experiment cluster if the force of the first intermediate is plotted against the force of the second intermediate. Consequently, if data recorded in different experiments are pooled, this clustering leaves the wrong impression of a correlation.

[18] Consequently, the force ratio approach could also be a valuable concept for force measurement techniques where absolute values are not known.

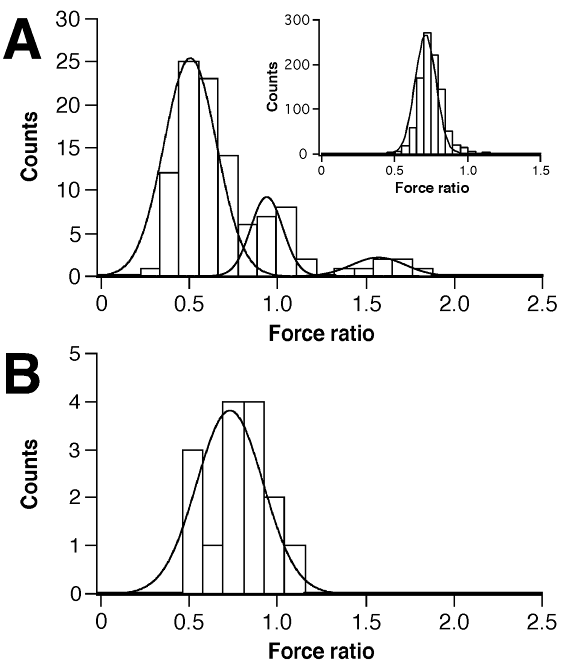

Figure 7-1 Force ratio histograms for α-helices E and D of BR. To generate the histograms, the unfolding force of α-helix D was divided by the unfolding force of α-helix E for each single molecule. (A) Trimeric BR shows a complex distribution, which is well described by 3 Gaussian fits centered at 0.51±0.02, 0.94±0.03 and 1.57±0.02 (n=104; *v*=654 nm/s). Inset: force ratio histogram of the corresponding MC simulation with a single peak centered at 0.72±0.01 (n=1000) (B) Data from monomeric BR show single peak centered at 0.74±0.02 (n=16). The trimeric data were taken from Chapter 3 and the monomeric data were provided by K.T. Sapra (BioTec, TU Dresden, Dresden)

7.2 Probing the folding of single (membrane) proteins

Since the pioneering work of C.B. Anfinsen (Anfinsen, 1973) protein folding has been an area of major interest for biological researchers. However, most protein folding studies have focused on many small water-soluble proteins, as membrane proteins are considerably more difficult to work with (Chapter 1.2.2). Very recently, we and others have introduced novel single-molecule folding techniques capable of measuring the folding kinetics and the folding trajectories of single (membrane) proteins (Kedrov *et al.*, 2004; Li and Fernandez, 2004). I would like to introduce these techniques, as they appear to become increasingly important for the study of membrane protein folding and misfolding in the future.

Our single-molecule folding experiments on the Na^+/H^+ antiporter NhaA from *E. coli* allowed to describe the folding process of single α-helices and to estimate their folding kinetics (Kedrov *et al.*, 2004). Using force spectroscopy the reconstituted NhaA molecules were partly unfolded leaving only two α-helices anchored in the lipid membrane. In the next step, the cantilever was lowered to close proximity (but not into contact) of the membrane surface thereby relaxing the unfolded polypeptide chain. At this stage, the system was left to equilibrate for 0.1 to five seconds allowing the coiled polypeptide chain to assume its free energy minimum. The efficiency of the refolding process was then measured from repeated unfolding cycles. In most cases all peaks which were observed during the initial unfolding were also detected if the refolding time was longer than > 5 seconds. This indicated that the secondary structures of NhaA spontaneously refold and supports the postulation that unfolding and folding of α-helices may be fully reversible (Hunt *et al.*, 1997; Popot *et al.*, 1987). Finally, plotting the refolding probability as a function of time allows the folding rate of these structural element of NhaA to be determined.

J.M. Fernandez and H. Li recently presented an exciting single-molecule folding study on the water-soluble protein Ubiquitin (Li and Fernandez, 2004). The implementation of a fast feedback loop, which controls the position of the piezoelectric element, allowed the application of well-defined forces to single molecules. It was shown, that the application of a pre-defined quench force (force-clamp spectroscopy) or a linearly increasing force (force-ramp spectroscopy) allows a more unambiguous measurement of the unfolding kinetics of single proteins (Oberhauser *et al.*, 2001; Schlierf *et al.*, 2004). Most importantly, lowering the quench-force below a critical level (≈ 15 pN) triggers the refolding of the stretched protein. During refolding, the piezoelectric element is constantly moving to maintain the small quench-force. As the trajectory of the piezoelectric element reflects the end-to-end distance of the protein a direct, time-resolved measure for the folding pathway and trajectory of an individual protein becomes available. In the last few months, we could successfully implement a versatile feedback loop, which offers a comparable response time to the one presented by Fernandez and Li(□ 4 ms). The realization of the force-feedback loop in combination with conventional unfolding experiments is one important step towards the application of force-clamp spectroscopy to membrane proteins.

I am convinced that these two methods will allow detecting the interactions and the intermediates during folding and thereby help to reconstruct the folding pathway of water-soluble and membrane proteins. Maybe the most important application of this approach will be to study misfolded proteins, i.e. those trapped in alternative kinetically stable conformations, and to reveal the influence physiologically relevant parameters on individual inter- and intramolecular interactions.

7.3 Single-molecule visco-elasticity measurements

In Chapter 5, I have presented two approaches to measure the visco-elastic properties of single molecules. These techniques are either based on the sinusoidal excitation of the cantilever or the analysis of thermal cantilever motion. In order to successfully continue these experiments, a few important steps should be taken in the near future. First of all the presented techniques should be applied as is to the proteins and polysaccharides of the extracellular matrix and the cytoskeleton as these play key roles in bio-mechanical processes. In particular, I would like to mention the protein collagen. Already in 2001, the group of P. Hansma used a conventional force spectroscopy setup to measure energy dissipation in single collagen molecules (Thompson *et al.*, 2001). From what we have learned in Chapter 5 I would expect plenty of new exciting insights if one would use the new technique presented there. Particularly these techniques should be combined with a recently developed preparation procedure, which yields collagen matrices with native-like structures (Jiang *et al.*, 2004).

In order to accurately describe the visco-elastic properties of these biologically relevant molecules, a few methodological improvements are required. The applicability of single-molecule visco-elasticity measurements would largely benefit if one were able to measure molecular responses as function of frequency. This becomes particularly important as the typical frequencies applied to single molecules in Chapter 5 (a few kHz) are not necessarily in range relevant to the native function of the molecules mentioned above. A very interesting way to study the frequency dependence was developed in the lab of D. Johannsmann (Gelbert *et al.*, 1999). Their recent theoretical concepts allow the frequency dependence of the dissipative response of molecular systems to be extracted from the thermal cantilever motion. Alternatively one could use a stiffer cantilever in FMS to gain a significantly increased S/N ratio and time resolution. The S/N ratio would benefit from the smaller displacement noise of the cantilever compared to the sinusoidal oscillation and would also allow the use of smaller oscillation amplitudes. As stiffer cantilevers usually have higher resonance frequencies, one could work at different drive frequencies and also reduce the time constant of the lock-in amplifier. Thus single-molecule force measurements with sub-ms time resolution could be possible.

Appendix

Abbreviations

μm	Micrometer (10^{-6} m)
Å	Ångstrom (10^{-10} m)
aa	Amino acid
AFM	Atomic force microscope
BFP	Biomembrane force probe
BR	Bacteriorhodopsin
DFS	Dynamic Force Spectroscopy
DLVO	Derjaguin-Landau-Verwey-Overbeek
EDL	Electrostatic double-layer
F-D	Force-distance
FJC	Freely jointed chain
FJC*	Extended freely jointed chain
FMS	Force modulation spectroscopy
GPCR	G-protein coupled receptor
Ig27-8	Octameric Immunoglobulin-27 construct
M-C	Monte-Carlo
ms	Millisecond (10^{-3} s)
nm	Nanometer (10^{-9} m)
PM	Purple membrane
pN	Piconewton (10^{-12} N)
PSD	Power spectral density
RMS	Root-mean-square
S/N	Signal-to-noise
SD	Standard deviation
SFA	Surface force apparatus
SHO	Simple harmonic oscillator
SPM	Scanning probe microscope
TMS	Thermal motion spectroscopy
V-K	Voigt-Kelvin
WLC	Worm like chain
WLC*	Extended worm like chain

Symbols

A	Amplitude (m)
A_{DC}	DC-amplitude (m)
a_{eff}	Effective cantilever size (m)
B	Measurement bandwidth (s^{-1})
d	Tip-sample distance / Extension (m)
D	Distance between two surfaces (m)
d_{eff}	Effective tip height (m)
dt	Time interval in MC simulation (s)
e_c	Electrolyte concentration
F	Force (N)
F_0	Magnitude of the drive force (N)
$F(t)$	Drive force (N)
F^*	Most probable unfolding/unbinding force (N)
F^*_{sim}	Most probable unfolding force in a MC simulation (N)
F_d	Hydrodynamic drag force (N)
F_{DLVO}	DLVO force per unit area (Nm^{-2})
F_{el}	EDL force per unit area (Nm^{-2})
$F_{measured}$	Measured F-D curve (N)
F_{min}	Smallest detectable force (N)
F_{net}	Net F-D curve including hydrodynamic contributions (N)
F_{RMS}	RMS force noise (N)

F_{vdw}	Van der Waals force per unit area (Nm^{-2})
H_a	Hamaker constant (□ 10^{-20} J for hydrocarbons in water)
k_B	Boltzmann constant (1.3806503 10^{-23} JK^{-1})
k_c	Spring constant (Nm^{-1})
k_{mol}	Molecular elasticity (Nm^{-1})
k_{tot}	Elasticity of a cantilever-molecule system (Nm^{-1})
k_u	(Natural) unfolding rate (s^{-1})
l	Length (m)
L	Langevin function
L_c	Contour length (m)
L_k	Kuhn length (m)
L_p	Persistence length (m)
m_c	Effective mass of the cantilever (kg)
m_{mol}	Effective molecular mass (kg)
m_{tot}	Effective mass of a cantilever-molecule system (kg)
n	Number of segments
N	Number of unfolding events
p	Frequency of peak appearance (%)
P_u	Unfolding probability
Q	Quality factor
Re	Reynolds number
r_f	Force loading rate (Ns^{-1})
s	Standard deviation of measured unfolding forces (N)
S	Stiffness of a polymer chain (N)
$S(d)$	Interfacial stiffness (Nm^{-1})
SEM	Standard error of the mean
t	Thickness (m)
T	Temperature (K)
v	Pulling speed (ms^{-1})
v_{tip}	Tip velocity (ms^{-1})
w	Width (m)
x	Deflection (m)
x□	Thermally averaged projection of an energy barrier (m)
x_u	Width of an energy barrier (m)
x_V	Deflection (V)
z_p	Piezo movement (m)
$\left\|x(t)^2\right\|$	Time-average mean-square displacement (m^2)
$\left\|X($□$)^2\right\|$	Power spectral density (m^2 or m^2Hz^{-1})
□F	Hidden force contribution (N)
□G_u^*	Free energy of activation for unfolding (J or J/mol, cal or cal/mol)
□□	Peak noise in damping measurements (Nsm^{-1})
□k_c	Peak noise in elasticity measurements (Nm^{-1})
□	Damping coefficient of the cantilever (Nsm^{-1})
□$_{mol}$	Molecular damping coefficient (Nsm^{-1})
□$_{ot}$	Damping coefficient of a cantilever-molecule system (Nsm^{-1})
□	Deflection sensitivity (Vm^{-1})
□	Stiffness of a polymer chain (Nm^{-1})
□	Surface charge density (Cm^{-2})
□	Retardation time of a V-K element (s)
□	Solution viscosity (Nsm^{-2})
□	Phase angle (rad)
□	Solution density (kgm^{-3})
□$_0$	Dielectric permittivity of free space ($C^2N^{-1}m^{-2}$)
□$_0$, v_0	Resonance frequency for little damping (s^{-1} or $rads^{-1}$)
□^{2}	Chi-square
□$_D$	Molecular damping in reaction rate theory (kgm^2s^{-2})
□$_0$	Diffusive relaxation time (s)
□$_r$	Relative dielectric permittivity of the electrolyte
□$_{res}$, v_{res}	Resonance frequency (s^{-1} or $rads^{-1}$)

List of publications

Peer-reviewed research articles

P.Y. Müller, H. Janovjak, A.R. Miserez, and Z. Dobbie
Processing of gene expression data generated by quantitative real-time RT-PCR.
Biotechniques 32(6): 1372-9. 2002.

H. Janovjak, M. Kessler, D. Oesterhelt, H.E. Gaub, and D.J. Müller
Unfolding pathways of native bacteriorhodopsin depend on temperature.
EMBO J. 22(19): 5220-9. 2003.

H. Janovjak, J. Struckmeier, M. Hubain, M. Kessler, A. Kedrov, and D.J. Müller
Probing the energy landscape of the membrane protein bacteriorhodopsin.
Structure 12(5): 871-9. 2004.

A. Kedrov, C. Ziegler, H. Janovjak, W. Kühlbrandt, and D.J. Müller
Controlled unfolding and refolding of a single sodium-proton antiporter using atomic force microscopy.
J. Mol. Biol. 340(5): 1143-52. 2004.

H. Janovjak, J. Struckmeier, and D.J. Müller
Hydrodynamic effects in fast AFM single molecule force measurements.
Eur. Biophys. J. 34(1): 91-6. 2005.

H. Janovjak, D.J. Müller, and A.D.L. Humphris
Molecular force modulation spectroscopy revealing the dynamic response of single bacteriorhodopsins.
Biophys. J. 88(2): 1423-31. 2005.

H. Janovjak, K.T. Sapra, and D.J. Müller
Complex stability of single proteins explored by forced unfolding experiments.
Biophys. J. 88(5): 37-9. 2005.

M. Kuhn, H. Janovjak, M. Hubain, and D.J. Müller
Automated alignment and pattern recognition of single-molecule force spectroscopy data.
J. Microsc. 218(Pt 2): 125-32. 2005.

C.B. Bippes, A.D. Humphris, D.J. Müller, and H. Janovjak
Direct measurement of single-molecule visco-elasiticity in AFM force-extension experiments.
Eur. Biophys. J., *in press.*

A. Kedrov, H. Janovjak, C. Ziegler, and D.J. Müller
Folding kinetics and pathways of single NhaA antiporters.
Submitted.

Review articles and book chapters

D.J. Müller, H. Janovjak, T. Lehto, L. Kuerschner, and K. Anderson
Observing structure, function and assembly of single proteins by AFM.
Prog. Biophys. Mol. Biol. 79(1-3): 1-43. 2002.

H. Janovjak, A. Kedrov, D. Cisneros, T.K. Sapra, J. Struckmeier, and D.J. Müller
Imaging and detecting molecular interactions of membrane proteins.
Neurobiol. Aging, *in press*

H. Janovjak, R. Sawhney, M. Stark, and D.J. Müller
A book chapter on Atomic Force Microscopy, to appear in the German textbook "Bioanalytik" (edited by F. Lottspeich, H. Zorbas; Spektrum Akademischer Verlag)

H. Janovjak and D.J. Müller
A book chapter on Atomic Force Microscopy, to appear in a handbook of modern microscopy techniques (edited by D.W. Hutmacher)

Acknowledgements

Only little of what was shown here would have been possible without my mentor and friend Daniel J. Müller. Thank you, Daniel, for a fantastic fime! You gave me the freedom to persue my own ideas but still I learned from you how to focus on the important things and how to speak with people. I remember our beginnings in the MPI back in 2001 - it only took us a few weeks to form a strong team! Today many things are different and both of us have moved on... but I'm happy to see that the team lasted for 4 years and is still out on the "folding science market"!

I'm indebted to Petra Schwille for her support, patience and many fruitful discussions. Thank you, Petra, for showing me how to look at many things (including biological membranes) from a very different perspective! I appreciate the many discussions we had, I'm grateful for your advice and that you provided such a pleasant atmosphere for my work.

I'm most grateful to Andy Humphris who introduced me to the "dynamic side" of single molecules. Thank you, Andy, for being such a patient and understanding teacher and friend! I will never forget your legendary visits to Dresden and my trips to Bristol. Despite your busy position you were a constant source of inspiration and had a major influence on my personal and scientific development!

Thank you,

Alexej Kedrov, for being such a fantastic wingman! You were a life-saver in many situations and I was very lucky to work next to an extraordinary person like you!

Jens "Strucki" Struckmeier, for being a great friend and your scientific and personal advice in the lab and on the Squash court.

Christian "Peppi" Bippes, for all your hard work and the fun and inside and outside lab!

Isabel "Belli" Richter for your help, being a friend, and for playing "Cat and Dog" once in a while! (My apologies to the rest of you for that...).

Martin Stark, Clemens Franz, David Cisneros, Kate Poole, Tiina Lehto, Erik Bartscherer, K. Tanuj Sapra, Jens Friedrichs and Pierre-Henri Puech for providing an exciting environment and helping me with papers and ideas - from each one of you I learned important things!

Last but not least I'm thankful to my family and friends

(listed in order of appearance)

my mother, father, and brother, Toni aka Fidu , Patrick, Fränzi, Edith , Berni,

Dan, CP & Julia, Gary, Anne, and Jelka

Bibliography

Abu-Lail, N.I. and Camesano, T.A. (2003) Polysaccharide properties probed with atomic force microscopy. *J Microsc*, **212**, 217-38.

Alcaraz, J., Buscemi, L., Puig-de-Morales, M., Colchero, J., Baro, A. and Navajas, D. (2002) Correction of microrheological measurements of soft samples with atomic force microscopy for the hydrodynamic drag on the cantilever. *Langmuir*, **18**, 716-21.

Alexander, S., Hellemans, L., Marti, O., Schneir, J., Elings, V., Hansma, P.K., Longmire, M. and Gurley, J. (1989) An atomic-resolution atomic-force microscope implemented using an optical lever. *Journal of Applied Physics*, **65**, 164-7.

Ando, T., Kodera, N., Takai, E., Maruyama, D., Saito, K. and Toda, A. (2001) A high-speed atomic force microscope for studying biological macromolecules. *Proc Natl Acad Sci U S A*, **98**, 12468-72.

Anfinsen, C.B. (1973) Principles that govern the folding of protein chains. *Science*, **181**, 223-30.

Ash, E.A. and Nicholls, G. (1972) Super-resolution aperture scanning microscope. *Nature*, **237**, 510-2.

Ashkin, A. (1997) Optical trapping and manipulation of neutral particles using lasers. *Proc Natl Acad Sci U S A*, **94**, 4853-60.

Ashkin, A., Dziedzic, J.M. and Yamane, T. (1987) Optical trapping and manipulation of single cells using infrared laser beams. *Nature*, **330**, 769-71.

Austin, R.H., Brody, J.P., Cox, E.C., Duke, T. and Volkmuth, W. (1997) Stretch genes. *Phys Today*, **50**, 31-8.

Bailey, S.W. (1984) Micas. *Rev.Mineral.*, **13**.

Barsegov, V. and Thirumalai, D. (2005) Dynamics of unbinding of cell adhesion molecules: transition from catch to slip bonds. *Proc Natl Acad Sci U S A*, **102**, 1835-9.

Baumann, C.G., Smith, S.B., Bloomfield, V.A. and Bustamante, C. (1997) Ionic effects on the elasticity of single DNA molecules. *Proc Natl Acad Sci U S A*, **94**, 6185-90.

Bell, G.I. (1978) Models for the specific adhesion of cells to cells. *Science*, **200**, 618-27.

Benmouna, F. and Johannsmann, D. (2002) Hydrodynamic interaction of AFM cantilevers with solid walls: An investigation based on AFM noise analysis. *Eur Phys E*, **9**, 435-41.

Benmouna, F. and Johannsmann, D. (2004) Viscoelasticity of gelatin surfaces probed by AFM noise analysis. *Langmuir*, **20**, 188-93.

Best, R.B., Fowler, S.B., Toca-Herrera, J.L. and Clarke, J. (2002) A simple method for probing the mechanical unfolding pathway of proteins in detail. *Proc Natl Acad Sci. USA*, **99**, 12143-8.

Best, R.B., Li, B., Steward, A., Daggett, V. and Clarke, J. (2001) Can non-mechanical proteins withstand force? Stretching barnase by atomic force microscopy and molecular dynamics simulation. *Biophys J*, **81**, 2344-56.

Betzig, E., Finn, P.L. and Wiener, J.S. (1992) Combined shear force and near-field scanning optical microscopy. *Appl Phys Lett*, **60**, 2484-6.

Bezanilla, F. (2005) Voltage-gated ion channels. *IEEE Trans Nanobioscience*, **4**, 34-48.

Bieri, O., Wirz, J., Hellrung, B., Schutkowski, M., Drewello, M. and Kiefhaber, T. (1999) The speed limit for protein folding measured by triplet-triplet energy transfer. *Proc Natl Acad Sci U S A*, **96**, 9597-601.

Binnig, G., Quate, C.F. and Gerber, C. (1986) Atomic force microscope. *Phys Rev Lett*, **56**, 930-3.

Binnig, G. and Rohrer, H. (1983) Scanning tunneling microscopy. *Surface science*, **126**, 236-44.

Blaurock, A.E. and Stoeckenius, W. (1971) Structure of the purple membrane. *Nat New Biol*, **233**, 152-5.

Booth, P.J. (2000) Unravelling the folding of bacteriorhodopsin. *Biochim Biophys Acta*, **1460**, 4-14.

Booth, P.J., Templer, R.H., Curran, A.R. and Allen, S.J. (2001) Can we identify the forces that drive the folding of integral membrane proteins? *Biochem Soc T*, **29**, 408-13.

Booth, P.J., Templer, R.H., Meijberg, W., Allen, S.J., Curran, A.R. and Lorch, M. (2001) In vitro studies of membrane protein folding. *Crit Rev Biochem Mol Biol*, **36**, 501-603.

Brockwell, D.J., Paci, E., Zinober, R.C., Beddard, G.S., Olmsted, P.D., Smith, D.A., Perham, R.N. and Radford, S.E. (2003) Pulling geometry defines the mechanical resistance of a beta-sheet protein. *Nat Struct Biol*, **10**, 731-7.

Bustamante, C., Chemla, Y.R., Forde, N.R. and Izhaky, D. (2004) Mechanical processes in biochemistry. *Annu Rev Biochem*, **73**, 705-48.

Bustamante, C., Marko, J.F., Siggia, E.D. and Smith, S. (1994) Entropic elasticity of lambda-phage DNA. *Science*, **265**, 1599-600.

Butt, H.-J., Jaschke, M. and Ducker, W. (1995) Measuring surface forces in aqueous solution with the atomic force microscope. *Bioelect. Bioenerg.*, **38**, 191-201.

Butt, H.J. and Jaschke, M. (1995) Calculation of thermal noise in atomic force microscopy. *Nanotechnology*, **6**, 1-7.

Carrion-Vazquez, M., Li, H., Lu, H., Marszalek, P.E., Oberhauser, A.F. and Fernandez, J.M. (2003) The mechanical stability of ubiquitin is linkage dependent. *Nat Struct Biol*, **10**, 738-43.

Carrion-Vazquez, M., Oberhauser, A.F., Fowler, S.B., Marszalek, P.E., Broedel, S.E., Clarke, J. and Fernandez, J.M. (1999) Mechanical and chemical unfolding of a single protein: a comparison. *Proc Natl Acad Sci U S A*, **96**, 3694-9.

Chen, G.Q. and Gouaux, E. (1999) Probing the folding and unfolding of wild-type and mutant forms of bacteriorhodopsin in micellar solutions: Evaluation of reversible unfolding conditions. *Biochemistry*, **38**, 15380-7.

Chen, G.Y., Warmack, R.J., Thundat, T., Allison, D.P. and Huang, A. (1994) Resonance response of scanning force microscopy cantilevers. *Rev Sci Ins*, **65**, 2532-7.

Chon, J.W.M., Mulvaney, P. and Sader, J.E. (2000) Experimental validation of theoretical models for the frequency response of atomic force microscope cantilever beams immersed in fluids *J Appl Phys*, **87**, 3978-88.

Cisneros, D.A., Oesterhelt, D. and Müller, D.J. (2005) Probing origins of molecular interactions stabilizing the membrane proteins halorhodopsin and bacteriorhodopsin. *Structure*, **13**, 235-42.

Cladera, J., Galisteo, M.L., Sabes, M., Mateo, P.L. and Padros, E. (1992) The role of retinal in the thermal stability of the purple membrane. *Eur J Biochem*, **207**, 581-5.

Cleveland, J.P., Anczykowski, B., Schmid, A.E. and Elings, V.B. (1998) Energy-dissipation in tapping-mode atomic-force microscopy. *Applied Physics Letters*, **72**, 2613-5.

Cleveland, J.P., Manne, S., Bocek, D. and Hansma, P.K. (1993) A nondestructive method for determining the spring constant of cantilevers force scanning probe microscopy. *Rev Sci Ins*, **64**, 403-5.

Cox, R.G. and Brenner, H. (1967) Slow motion of a sphere through a viscous fluid towards a plane surface: small gap widths including inertial effects. *Chem. Eng. Sci.*, **22**, 1753.

Czajkowsky, D.M., Iwamoto, H. and Shao, Z. (2000) Atomic force microscopy in structural biology: from the subcellular to the submolecular. *J Electron Microsc*, **49**, 395-406.

Czajkowsky, D.M. and Shao, Z. (2003) Inhibition of protein adsorption to muscovite mica by monovalent cations. *Journal of Microscopy*, **211**, 1-7.

de Paris, R., Strunz, T., Güntherodt, H.J. and Hegner, M. (2000) Force spectroscopy and dynamics of the biotin-avidin bond studied by scanning force microscopy. *Single Mol*, **1**, 285-90.

DeFelice, L.J. (2004) Transporter structure and mechanism. *Trends Neurosci*, **27**, 352-9.

Dietz, H. and Rief, M. (2004) Exploring the energy landscape of GFP by single-molecule mechanical experiments. *Proc Natl Acad Sci U S A*, **101**, 16192-7.

Drake, B., Prater, C.B., Weisenhorn, A.L., Gould, S.A., Albrecht, T.R., Quate, C.F., Cannell, D.S., Hansma, H.G. and Hansma, P.K. (1989) Imaging crystals, polymers, and processes in water with the atomic force microscope. *Science*, **243**, 1586-9.

Dufrene, Y.F. (2004) Using nanotechniques to explore microbial surfaces. *Nat Rev Microbiol*, **2**, 451-60.

Ellis, J.S., Abdelhady, H.G., Allen, S., Davies, M.C., Roberts, C.J., Tendler, S.J. and Williams, P.M. (2004) Direct atomic force microscopy observations of monovalent ion induced binding of DNA to mica. *J Microsc*, **215**, 297-301.

Enders, O., Korte, F. and Kolb, H.A. (2004) Lorentz-force-induced excitation of cantilevers for oscillation-mode scanning probe microscopy. *Surf Int Anal*, **36**, 119-23.

Engel, A. and Müller, D.J. (2000) Observing single biomolecules at work with the atomic force microscope. *Nat Struct Biol*, **7**, 715-8.

Engelman, D.M., Chen, Y., Chin, C.N., Curran, A.R., Dixon, A.M., Dupuy, A.D., Lee, A.S., Lehnert, U., Matthews, E.E., Reshetnyak, Y.K., Senes, A. and Popot, J.L. (2003) Membrane protein folding: beyond the two stage model. *FEBS Lett*, **555**, 122-5.

Engelman, D.M. and Steitz, T.A. (1981) The spontaneous insertion of proteins into and across membranes: the helical hairpin hypothesis. *Cell*, **23**, 411-22.

Erlandsson, R., McClelland, G., Mate, C.M. and Chiang, S. (1988) Atomic Force Microscopy using optical interferometry. *J Vac Sci Technol A*, **6**, 266-70.

Essen, L., Siegert, R., Lehmann, W.D. and Oesterhelt, D. (1998) Lipid patches in membrane protein oligomers: crystal structure of the bacteriorhodopsin-lipid complex. *Proc Natl Acad Sci U S A*, **95**, 11673-8.

Evans, E. (2001) Probing the relation between force, lifetime and chemistry in single molecular bonds. *Annu Rev Biophys Biomol Struct*, **30**, 105-28.

Evans, E., Berk, D. and Leung, A. (1991) Detachment of agglutinin-bonded red blood cells. I. Forces to rupture molecular-point attachments. *Biophys J*, **59**, 838-48.

Evans, E., Leung, A., Hammer, D. and Simon, S. (2001) Chemically distinct transition states govern rapid dissociation of single L-selectin bonds under force. *Proc Natl Acad Sci U S A*, **98**, 3784-9.

Evans, E., Leung, A., Heinrich, V. and Zhu, C. (2004) Mechanical switching and coupling between two dissociation pathways in a P-selectin adhesion bond. *Proc Natl Acad Sci U S A*, **101**, 11281-6.

Evans, E. and Ludwig, F. (2000) Dynamic strengths of molecular anchoring and material cohesion in fluid biomembranes. *J Phys Condens Matter*, **12**, A315-A20.

Evans, E. and Ritchie, K. (1997) Dynamic strength of molecular adhesion bonds. *Biophys J*, **72**, 1541-55.

Faham, S., Yang, D., Bare, E., Yohannan, S., Whitelegge, J.P. and Bowie, J.U. (2004) Side-chain contributions to membrane protein structure and stability. *J Mol Biol*, **335**, 297-305.

Filipek, S., Teller, D.C., Palczewski, K. and Stenkamp, R. (2003) The crystallographic model of rhodopsin and its use in studies of other G protein-coupled receptors. *Annu Rev Biophys Biomol Struct*, **32**, 375-97.

Filmore, D. (2004) It's a GPCR world. *Modern Drug Disc*, **7**, 24-8.

Flitsch, S.L. and Khorana, H.G. (1989) Structural studies on transmembrane proteins. 1. Model study using bacteriorhodopsin mutants containing single cysteine residues. *Biochemistry*, **28**, 7800-5.

Florin, E.L., Rief, M., Lehmann, H., Ludwig, M., Dornmair, C., Moy, V.T. and Gaub, H.E. (1995) Sensing specific molecular-interactions with the atomic force microscope. *Biosensors Bioelectr*, **10**, 895-901.

Forbes, J.G. and Wang, K. (2004) Simultaneous dynamic stiffness and extension profiles of single titin molecules: Nanomechanical evidence for unfolding intermediates *J Vac Sci Technol A*, **22**, 1439-43.

Fotiadis, D., Scheuring, S., Muller, S.A., Engel, A. and Muller, D.J. (2002) Imaging and manipulation of biological structures with the AFM. *Micron*, **33**, 385-97.

Frederix, P.T., Hoogenboom, B., W., Fotiadis, D., Müller, D.J. and Engel, A. (2004) Atomic force microscopy of biological samples. *MRS Bulletin*, **29**, 449-55.

Garcia, R. and Perez, R. (2002) Dynamic atomic force microscopy methods. *Surf Sci Rep*, **47**, 197-301.

Gelbert, M., Roters, A., Schimmel, M., Ruhe, J. and Johannsmann, D. (1999) Viscoelastic spectra of soft polymer interfaces obtained by noise analysis of AFM cantilevers. *Surf Int Anal*, **27**, 572-7.

Giessibl, F.J. (1995) Atomic-resolution of the silicon (111)-(7x7) surface by atomic-force microscopy *Science* **267**, 68-71.

Gittes, F. and Schmidt, C.F. (1998) Thermal noise limitations on micromechanical experiments. *Eur. Biophys. J.*, **27**, 75-81.

Göddenhenrich, T., Lemke, H., Hartmann, U. and Heiden, C. (1990) Force microscope with capacitive displacement detection. *J Vac Sci Technol A*, **8**, 383-7.

Gore, J., Ritort, F. and Bustamante, C. (2003) Bias and error in estimates of equilibrium free-energy differences from nonequilibrium measurements. *Proc Natl Acad Sci U S A*, **100**, 12564-9.

Gotsmann, B., Anczykowski, B., Seidel, C. and Fuchs, H. (1999) Determination of tip-sample interaction forces from measured dynamic force spectroscopy curves. *Appl Surf Sci*, **140**, 314-9.

Grigorieff, N., Ceska, T.A., Downing, K.H., Baldwin, J.M. and Henderson, R. (1996) Electron-crystallographic refinement of the structure of bacteriorhodopsin. *J Mol Biol*, **259**, 393-421.

Guthold, M., Zhu, X., Rivetti, C., Yang, G., Thomson, N.H., Kasas, S., Hansma, H.G., Smith, B., Hansma, P.K. and Bustamante, C. (1999) Direct observation of one-dimensional diffusion and transcription by Escherichia coli RNA polymerase. *Biophys J*, **77**, 2284-94.

Haltia, T. and Freire, E. (1995) Forces and factors that contribute to the structural stability of membrane proteins. *Biochim Biophys Acta*, **1241**, 295-322.

Han, W.H., Lindsay, S.M. and Jing, T.W. (1996) A magnetically driven oscillating probe microscope for operation in liquids. *Applied Physics Letters*, **69**, 4111-3.

Hanggi, P., Talkner, P. and Borkovec, M. (1990) Reaction rate theory - 50 years after Kramers. *Rev Mod Phys*, **62**, 251-341.

Hansma, H.G., Kasuya, K. and Oroudjev, E. (2004) Atomic force microscopy imaging and pulling of nucleic acids. *Curr Opin Struct Biol*, **14**, 380-5.

Heinz, W.F. and Hoh, J.H. (1999) Relative surface charge density mapping with the atomic force microscope. *Biophys. J.*, **76**, 528-38.

Hinterdorfer, P., Kienberger, F., Raab, A., Gruber, H.J., Baumgartner, W., Kada, G., Riener, C., Wielert-Badt, S., Borken, C. and Schindler, H. (2000) Poly(Ethylene Glycol): An ideal spacer for molecular recognition force microscopy/spectroscopy. *Single Mol*, **1**, 99-103.

Hodges, C.S. (2002) Measuring forces with the AFM: polymeric surfaces in liquids. *Advances in Colloid and Interface Science*, **99**, 13 - 75.

Hoffmann, P.M., Jeffery, S., Pethica, J.B., Ozer, H.O. and Oral, A. (2001) Energy dissipation in atomic force microscopy and atomic loss processes. *Phys Rev Lett*, **87**, 265502-4.

Howard, J. (2001) *Mechanics of Motor Proteins and the Cytoskeleton*. Sinauer Press, Sunderland, MA.

Hummer, G. and Szabo, A. (2005) Free energy surfaces from single-molecule force spectroscopy. *Acc Chem Res*, **38**, 504-13.

Humphris, A.D.L., Antognozzi, M., McMaster, T.J. and Miles, M.J. (2002) Transverse dynamic force spectroscopy: A novel approach to determining the complex stiffness of a single molecule. *Langmuir*, **18**, 1729-33.

Humphris, A.D.L., Hobbs, J.K. and Miles, M.J. (2003) Ultrahigh-speed scanning near-field optical microscopy capable of over 100 frames per second. *Applied Physics Letters*, **83**, 6-8.

Humphris, A.D.L., Miles, M.J. and Hobbs, J.K. (2005) A mechanical microscope: High-speed atomic force microscopy. *Applied Physics Letters*, **86**.

Humphris, A.D.L., Tamayo, J. and Miles, M.J. (2000) Active quality factor control in liquids for force spectroscopy. *Langmuir*, **16**, 7891-4.

Hunt, J.F., Earnest, T.N., Bousche, O., Kalghatgi, K., Reilly, K., Horvath, C., Rothschild, K.J. and Engelman, D.M. (1997) A biophysical study of integral membrane protein folding. *Biochemistry*, **36**, 15156-76.

Hutter, J.L. and Bechhoefer, J. (1994) Calibration of atomic force microscopy tips. *Rev Sci Instrum*, **64**, 1868-73.

Ikai, A. and Afrin, R. (2003) Toward mechanical manipulations of cell membranes and membrane proteins using an atomic force microscope: an invited review. *Cell Biochem Biophys*, **39**, 257-77.

Ishijima, A., Kojima, H., Higuchi, H., Harada, Y., Funatsu, T. and Yanagida, T. (1996) Multiple- and single-molecule analysis of the actomyosin motor by nanometer piconewton manipulation with a microneedle: Unitary steps and forces. *Biophys J*, **70**, 383-400.

Israelachvili, J. (1991) *Intermolecular and surface forces*. Academic Press, London.

Janshoff, A., Neitzert, M., Oberdörfer, Y. and Fuchs, H. (2000) Force spectroscopy of molecular systems - single molecule spectroscopy of polymers and biomolecules. *Angew Chem Int Ed*, **39**, 3212-37.

Jelesarov, I. and Bosshard, H.R. (1999) Isothermal titration calorimetry and differential scanning calorimetry as complementary tools to investigate the energetics of biomolecular recognition. *J Mol Recognit*, **12**, 3-18.

Jiang, F., Khairy, K., Poole, K., Howard, J. and Müller, D.J. (2004) Creating nanoscopic collagen matrices using atomic force microscopy. *Microsc Res Tech*, **64**, 435-40.

Kasas, S., Thomson, N.H., Smith, B.L., Hansma, H.G., Zhu, X., Guthold, M., Bustamante, C., Kool, E.T., Kashlev, M. and Hansma, P.K. (1997) Escherichia coli RNA polymerase activity observed using atomic force microscopy. *Biochemistry*, **36**, 461-8.

Kawakami, M., Byrne, K., Khatri, B., Mcleish, T.C., Radford, S.E. and Smith, D.A. (2004) Viscoelastic properties of single polysaccharide molecules determined by analysis of thermally driven oscillations of an atomic force microscope cantilever. *Langmuir*, **20**, 9299-303.

Kawakami, M., Byrne, K., Khatri, B., Mcleish, T.C., Radford, S.E. and Smith, D.A. (2005) Viscoelastic Measurements of Single Molecules on a Millisecond Time Scale by Magnetically Driven Oscillation of an Atomic Force Microscope Cantilever. *Langmuir*, **21**, 4765-72.

Kedrov, A., Ziegler, C., Janovjak, H., Kühlbrandt, W. and Müller, D.J. (2004) Controlled unfolding and refolding of a single sodium-proton antiporter using atomic force microscopy. *JMB*, **340**, 1143-52.

Kienberger, F., Pastushenko, V.P., Kada, G., Gruber, H.J., Riener, C., Schindler, H. and Hinterdorfer, P. (2000) Static and dynamical properties of single poly(ethylene glycol) molecules investigated by force spectroscopy. *Single Mol*, **1**, 123-8.

Kimura, Y., Vassylyev, D.G., Miyazawa, A., Kidera, A., Matsushima, M., Mitsuoka, K., Murata, K., Hirai, T. and Fujiyoshi, Y. (1997) Surface of bacteriorhodopsin revealed by high-resolution electron crystallography. *Nature*, **389**, 206-11.

Kramers, H.A. (1940) Brownian motion in a field of force and the diffusion model of chemical reactions *Physica*, **7**, 284-304.

Kratky, O. and Porod, G. (1949) Röntgenuntersuchung gelöster Fadenmoleküle. *Recl Trav Chim PB*, **12**, 1106-22.

Krogh, A., Larsson, B., von Heijne, G. and Sonnhammer, E.L. (2001) Predicting transmembrane protein topology with a hidden Markov model: application to complete genomes. *J Mol Biol*, **305**, 567-80.

Kuhn, A. (1987) Bacteriophage M13 procoat protein inserts into the plasma membrane as a loop structure. *Science*, **238**, 1413-5.

Kuhn, M., Janovjak, H., Hubain, M. and Müller, D.J. (2005) Automated alignment and pattern recognition of single-molecule force spectroscopy data. *J Microsc-Oxford*, **218**, 125-32.

Landau, L.D. and Lifshitz, E.M. (1980) *Statistical physics*. Pergamon Press, Oxford.

Landau, L.D. and Lifshitz, E.M. (1987) *Fluid Mechanics*. Pergamon Press, Oxford.

Lantz, M., Liu, Y.Z., Cui, X.D., Tokumoto, H. and Lindsay, S.M. (1999) Dynamic force microscopy in fluid. *Surf Int Anal*, **27**, 354-60.

Lapidus, L.J., Eaton, W.A. and Hofrichter, J. (2000) Measuring the rate of intramolecular contact formation in polypeptides. *Proc Natl Acad Sci U S A*, **97**, 7220-5.

Law, R., Harper, S., Speicher, D.W. and Discher, D.E. (2004) Influence of lateral association on forced unfolding of antiparallel spectrin heterodimers. *J Biol Chem*, **279**, 16410-6.

Law, R., Liao, G., Harper, S., Yang, G.L., Speicher, D.W. and Discher, D.E. (2003) Pathway shifts and thermal softening in temperature-coupled forced unfolding of spectrin domains. *Biophys J*, **85**, 3286-93.

Leckband, D. and Israelachvili, J. (2001) Intermolecular forces in biology. *Q Rev Biophys*, **34**, 105-267.

Lee, G.U., Chrisey, L.A. and Colton, R.J. (1994) Direct measurement of the forces between complementary strands of DNA. *Science*, **266**, 771-3.

Li, H.B. and Fernandez, J.M. (2004) Force-clamp spectroscopy monitors the folding trajectory of a single protein. *Science*, **303**, 1674-8.

Li, L., Huang, H.H., Badilla, C.L. and Fernandez, J.M. (2005) Mechanical unfolding intermediates observed by single-molecule force spectroscopy in a fibronectin type III module. *J Mol Biol*, **345**, 817-26.

Liang, S.D., Medich, D., Czajkowsky, D.M., Sheng, S.T., Yuan, J.Y. and Shao, Z.F. (2000) Thermal noise reduction of mechanical oscillators by actively controlled external dissipative forces. *Ultramicroscopy*, **84**, 119-25.

Lindsay, S.M., Lyubchenko, Y.L., Tao, N.J., Li, Y.Q., Oden, P.I., DeRose, J.A. and Pan, J. (1993) Scanning tunneling microscopy and atomic force microscopy studies of biomaterials at a liquid–solid interface. *J Vac Sci Technol A*, **11**, 808-15.

Liu, Y.Z., Leuba, S.H. and Lindsay, S.M. (1999) Relationship between stiffness and force in single molecule pulling experiments. *Langmuir*, **14**, 8547-8.

Lo, Y.S., Zhu, Y.J. and Beebe, T.P. (2001) Loading-rate dependence of individual ligand-receptor bond-rupture forces studied by atomic force microscopy. *Langmuir*, **17**, 3741-8.

Luecke, H., Schobert, B., Richter, H.T., Cartailler, J.P. and Lanyi, J.K. (1999) Structure of bacteriorhodopsin at 1.55 A resolution. *J Mol Biol*, **291**, 899-911.

Maeda, N. and Senden, T.J. (2000) A method for the calibration of force microscopy cantilevers via hydrodynamic drag. *Langmuir*, **16**, 9282-6.

Marko, J.F. and Siggia, E.D. (1995) Stretching DNA. *Macromolecules*, **28**, 8759.

Marshall, B.T., Long, M., Piper, J.W., Yago, T., McEver, R.P. and Zhu, C. (2003) Direct observation of catch bonds involving cell-adhesion molecules. *Nature*, **423**, 190-3.

Marszalek, P.E., Li, H.B., Oberhauser, A.F. and Fernandez, J.M. (2002) Chair-boat transitions in single polysaccharide molecules observed with force-ramp AFM. *Proceedings of the National Academy of Sciences of the United States of America*, **99**, 4278-83.

Marszalek, P.E., Lu, H., Li, H., Carrion-Vazquez, M., Oberhauser, A.F., Schulten, K. and Fernandez, J.M. (1999) Mechanical unfolding intermediates in titin modules. *Nature*, **402**, 100-3.

Marszalek, P.E., Oberhauser, A.F., Pang, Y.P. and Fernandez, J.M. (1998) Polysaccharide elasticity governed by chair-boat transitions of the glucopyranose ring. *Nature*, **396**, 661-4.

Marti, O., Elings, V., Haugan, M., Bracker, C.E., Schneir, J., Drake, B., Gould, S.A., Gurley, J., Hellemans, L. and Shaw, K. (1988) Scanning probe microscopy of biological samples and other surfaces. *J Microsc*, **152**, 803-9.

Marti, T., Otto, H., Mogi, T., Rosselet, S.J., Heyn, M.P. and Khorana, H.G. (1991) Bacteriorhodopsin mutants containing single substitutions of serine or threonine residues are all active in proton translocation. *J Biol Chem*, **266**, 6919-27.

Martin, Y., Williams, C.C. and Wickramasinghe, H.K. (1987) Atomic force microscope force mapping and profiling on a sub 100-Å scale. *J Appl Phys*, **61**, 4723-39.

Meixner, A.J. and Kneppe, H. (1998) Scanning near-field optical microscopy in cell biology and microbiology. *Cell Mol. Biol. (Noisy-le-grand)*, **44**, 673-88.

Merkel, R., Nassoy, P., Leung, A., Ritchie, K. and Evans, E. (1999) Energy landscapes of receptor-ligand bonds explored with dynamic force spectroscopy. *Nature*, **397**, 50-3.

Meyer, G. and Amer, N.M. (1988) Novel optical approach to atomic force microscopy. *Applied Physics Letters*, **53**, 1045-7.

Mitsui, K., Hara, M. and Ikai, A. (1996) Mechanical unfolding of alpha(2)-macroglobulin molecules with atomic force microscope. *FEBS Lett*, **385**, 29-33.

Mitsuoka, K., Hirai, T., Murata, K., Miyazawa, A., Kidera, A., Kimura, Y. and Fujiyoshi, Y. (1999) The structure of bacteriorhodopsin at 3.0 A resolution based on electron crystallography: implication of the charge distribution. *J Mol Biol*, **286**, 861-82.

Moy, V.T., Florin, E.L. and Gaub, H.E. (1994) Intermolecular forces and energies between ligands and receptors. *Science*, **266**, 257-9.

Muccio, D.D. and Cassim, J.Y. (1979) Interpretations of the effects of pH on the spectra of purple membrane. *J Mol Biol*, **135**, 595-609.

Mulholland, A.J. and Karplus, M. (1996) Simulations of enzymic reactions. *Biochem Soc Trans*, **24**, 247-54.

Müller, D.J., Amrein, M. and Engel, A. (1997) Adsorption of biological molecules to a solid support for scanning probe microscopy. *J Struct Biol*, **119**, 172-88.

Müller, D.J., Büldt, G. and Engel, A. (1995) Force-induced conformational change of bacteriorhodopsin. *J Mol Biol*, **249**, 239-43.

Müller, D.J., Engel, A. and Amrein, M. (1997) Preparation techniques for the observation of native biological systems with the atomic force microscope. *Biosensors Bioelectr*, **12**, 867-77.

Müller, D.J., Fotiadis, D., Scheuring, S., Müller, S.A. and Engel, A. (1999) Electrostatically balanced subnanometer imaging of biological specimens by atomic force microscope. *Biophys J*, **76**, 1101-011.

Müller, D.J., Janovjak, H., Lehto, T., Kuerschner, L. and Anderson, K. (2002) Observing structure, function and assembly of single proteins by AFM. *Prog Biophys Mol Biol*, **79**, 1-43.

Müller, D.J., Kessler, M., Oesterhelt, F., Möller, C., Oesterhelt, D. and Gaub, H. (2002) Stability of bacteriorhodopsin alpha-helices and loops analyzed by single-molecule force spectroscopy. *Biophys J*, **83**, 3578-88.

Neubauer, G., Cohen, S.R., McClelland, G.M., Horne, D. and Mate, C.M. (1990) Force microscopy with a bidirectional capacitance sensor. *Rev Sci Ins*, **61**, 2296-308.

Nevo, R., Stroh, C., Kienberger, F., Kaftan, D., Brumfeld, V., Elbaum, M., Reich, Z. and Hinterdorfer, P. (2003) A molecular switch between alternative conformational states in the complex of Ran and importin beta1. *Nat Struct Biol*, **10**, 553-7.

Nicklas, R.B. (1983) Measurements of the force produced by the mitotic spindle in anaphase. *J Cell Biol*, **97**, 542-48.

O'Shea, S.J. and Welland, M.E. (1998) Atomic force microscopy at solid-liquid interfaces. *Langmuir*, **14**, 4186-97.

Oberhauser, A.F., Hansma, P.K., Carrion-Vazquez, M. and Fernandez, J.M. (2001) Stepwise unfolding of titin under force-clamp atomic force microscopy. *Proc Natl Acad Sci U S A*, **98**, 468-72.

Oberhauser, A.F., Marszalek, P.E., Erickson, H.P. and Fernandez, J.M. (1998) The molecular elasticity of the extracellular matrix protein tenascin. *Nature*, **393**, 181-5.

Oesterhelt, D. and Stoeckenius, W. (1971) Rhodopsin-like protein from the purple membrane of Halobacterium halobium. *Nat New Biol*, **233**, 149-52.

Oesterhelt, D. and Stoeckenius, W. (1973) Functions of a new photoreceptor membrane. *Proc Natl Acad Sci U S A*, **70**, 2853-7.

Oesterhelt, D. and Stoeckenius, W. (1974) Isolation of the cell membrane of Halobacterium halobium and its fractionation into red and purple membrane. *Methods Enzymol*, **31**, 667-78.

Oesterhelt, F., Oesterhelt, D., Pfeiffer, M., Engel, A., Gaub, H.E. and Müller, D.J. (2000) Unfolding pathways of individual bacteriorhodopsins. *Science*, **288**, 143-6.

Okada, T. and Palczewski, K. (2001) Crystal structure of rhodopsin: implications for vision and beyond. *Curr Opin Struct Biol*, **11**, 420-6.

Ortiz, C. and Hadziioannou, G. (1999) Entropic elasticity of single polymer chains of poly(methacrylic acid) measured by atomic force microscopy. *Macromolecules*, **32**, 780-7.

Otto, H., Marti, T., Holz, M., Mogi, T., Lindau, M., Khorana, H.G. and Heyn, M.P. (1989) Aspartic acid-96 is the internal proton donor in the reprotonation of the Schiff base of bacteriorhodopsin. *Proc Natl Acad Sci U S A*, **86**, 9228-32.

Otto, H., Marti, T., Holz, M., Mogi, T., Stern, L.J., Engel, F., Khorana, H.G. and Heyn, M.P. (1990) Substitution of amino acids Asp-85, Asp-212, and Arg-82 in bacteriorhodopsin affects the proton release phase of the pump and the pK of the Schiff base. *Proc Natl Acad Sci U S A*, **87**, 1018-22.

Pashley, R.M. (1981) Hydration forces between mica surfaces in aqueous electrolyte solutions. *J. Colloid Interface Sci.*, **80**, 153-62.

Pashley, R.M. (1981) Hydration forces between mica surfaces in Li^+, Na^+, Na^+ and Cs^+ electrolyte solutions: a correlation of double layer and hydration forces with surface cation exchange properties. *J. Colloid Interface Sci.*, **83**, 531-46.

Pebay-Peyroula, E., Rummel, G., Rosenbusch, J.P. and Landau, E.M. (1997) X-ray structure of bacteriorhodopsin at 2.5 angstroms from microcrystals grown in lipidic cubic phases. *Science*, **277**, 1676-81.

Pennyworth, A. (2005) Batman Begins, Warner Bros. Entertainment Inc.

Pethica, J.B. and Oliver, W.C. (1987) Tip surface interactions in STM and AFM. *Phys Scr T19*, **A**, 61-6.

Philippsen, A., Im, W., Engel, A., Schirmer, T., Roux, B. and Muller, D.J. (2002) Imaging the electrostatic potential of transmembrane channels: atomic probe microscopy of OmpF porin. *Biophys J*, **82**, 1667-76.

Popot, J.L. and Engelman, D.M. (2000) Helical membrane protein folding, stability, and evolution. *Annu Rev Biochem*, **69**, 881-922.

Popot, J.L. and Engelmann, D.M. (1990) Membrane protein folding and oligomerization: the two stage model. *Biochemistrty*, **29**, 4031-7.

Popot, J.L., Gerchman, S.E. and Engelman, D.M. (1987) Refolding of bacteriorhodopsin in lipid bilayers. A thermodynamically controlled two-stage process. *J Mol Biol*, **198**, 655-76.

Proksch, R., Lal, R., Hansma, P.K., Morse, D. and Stucky, G. (1996) Imaging the internal and external pore structure of membranes in fluid: Tapping Mode scanning ion conductance microscopy. *Biophys. J.*, **71**, 2155-7.

Proksch, R., Schäffer, T.E., Cleveland, J.P., Callahan, R.C. and Viani, M.B. (2004) Finite optical spot size and position corrections in thermal spring constant calibration. *Nanotechnology*, **15**, 1344-50.

Ptak, A., Takeda, S., Nakamura, C., Miyake, J., Kageshima, M., Jarvis, S.P. and Tokumoto, H. (2001) Modified atomic force microscope applied to the measurement of elastic modulus for a single peptide molecule. *J Appl Phys*, **90**, 3095-9.

Pusch, M. and Jentsch, T.J. (2005) Unique structure and function of chloride transporting CLC proteins. *IEEE Trans Nanobioscience*, **4**, 49-57.

Putman, C.A.J., van der Werf, K., de Grooth, B.G., van Hulst, N.F., Greve, J. and Hansma, P.K. (1992) A new imaging mode in the atomic force microscopy based on the error signal. *SPIE*, **1639**, 198-204.

Putman, C.A.J., Van der Werf, K.O., De Grooth, B.G., Van Hulst, N.F. and Greve, J. (1994) Tapping mode atomic-foce microscopy in liquid. *Applied Physics Letters*, **64**, 2454-6.

Racker, E. and Hinkle, P.C. (1974) Effect of temperature on the function of a proton pump. *J Membr Biol*, **17**, 181-8.

Radford, S.E. (2000) Protein folding: progress made and promises ahead. *Trends Biochem Sci*, **25**, 611-8.

Radmacher, M., Tillmann, R.W., Fritz, M. and Gaub, H.E. (1992) From molecules to cells: imaging soft samples with the atomic force microscope. *Science*, **257**, 1900-5.

RCSB. Research Collaboratory for Structural Bioinformatics, Protein Data Bank (PDB), www.pdb.org.

Rief, M., Fernandez, J.M. and Gaub, H.E. (1998) Elastically coupled two-level systems as a model for biopolymer extensibility. *PRL*, **81**, 4764-7.

Rief, M., Gautel, M., Oesterhelt, F., Fernandez, J.M. and Gaub, H.E. (1997) Reversible unfolding of individual titin immunoglobulin domains by AFM. *Science*, **276**, 1109-12.

Rief, M., Gautel, M., Schemmel, A. and Gaub, H.E. (1998) The mechanical stability of immunoglobulin and fibronectin III domains in the muscle protein titin measured by atomic force microscopy. *Biophys J*, **75**, 3008-14.

Rief, M. and Grubmüller, H. (2002) Force spectroscopy of single biomolecules. *Chemphyschem*, **3**, 255-61.

Rief, M., Oesterhelt, F., Heymann, B. and Gaub, H.E. (1997) Single molecule force spectroscopy on polysaccharides by atomic force microscopy. *Science*, **275**, 1295-7.

Rogers, B., York, D., Whisman, N., Jones, M., Murray, K., Adams, J.D., Sulchek, T. and Minne, S.C. (2002) Tapping mode atomic force microscopy in liquid with an insulated piezoelectric microactuator. *Rev Sci Ins*, **73**, 3242-4.

Roters, A. and Johannsmann, D. (1996) Distance-dependent noise measurements in scanning force microscopy. *J. Phys. Condens. Matter*, **8**, 7561-77.

Sader, J.E. (1998) Frequency response of cantilever beams immersed in viscous fluids with applications to the atomic force microscope. *J Appl Phys*, **84**, 64-76.

Saenz, J.J., Garcia, N., Grutter, P., Meyer, E., Heinzelmann, H., Wiesendanger, R., Rosenthaler, L., Hidber, H.R. and Güntherodt, H.J. (1987) Observation of magnetic forces by the atomic force microscope. *Journal of Applied Physics*, **62**, 4293-5.

Sanders, C.R. and Myers, J.K. (2004) Disease-related misassembly of membrane proteins. *Annu Rev Biophys Biomol Struct*, **33**, 25-51.

Sarid, D. (1994) *Scanning Force Microscopy*. Oxford University Press, Oxford.

Schäffer, T.E., Cleveland, J.P., Ohnesorge, F., Walters, D.A. and Hansma, P.K. (1996) Studies of vibrating atomic force microscope cantilevers in liquid. *J Appl Phys*, **80**, 3622-7.

Scheuring, S., Levy, D. and Rigaud, J.L. (2005) Watching the components of photosynthetic bacterial membranes and their in situ organisation by atomic force microscopy. *Biochim Biophys Acta*, **1712**, 109-27.

Scheuring, S., Müller, D.J., Stahlberg, H., Engel, H.A. and Engel, A. (2002) Sampling the conformational space of membrane protein surfaces with the AFM. *Eur. Biophys. J.*, **31**, 172-8.

Schlierf, M., Li, H. and Fernandez, J.M. (2004) The unfolding kinetics of ubiquitin captured with single-molecule force-clamp techniques. *Proc Natl Acad Sci U S A*, **101**, 7299-304.

Schnell, S. and Turner, T.E. (2004) Reaction kinetics in intracellular environments with macromolecular crowding: simulations and rate laws. *Prog Biophys Mol Biol*, **85**, 235-60.

Schönenberger, C. and Alvarado, S.F. (1989) A differential interferometer for force microscopy. *Rev Sci Ins*, **60**, 3131-34.

Schultz, J.M. (1974) Sinusoidal loading and the mechanical loss measurement. In Amundson, N.R. (ed.), *Polymer materials science*. Prentice Hall, Inc., Englewood Cliffs, New Jersey, Vol. 1, pp. 371-9.

Schulz, G.E. (2002) The structure of bacterial outer membrane proteins. *Biochim Biophys Acta*, **1565**, 308-17.

Schulz, G.E. (2003) Transmembrane beta-barrel proteins. *Adv Protein Chem*, **63**.

Seddon, A.M., Curnow, P. and Booth, P.J. (2004) Membrane proteins, lipids and detergents: not just a soap opera. *Biochim Biophys Acta*, **1666**, 105-17.

Senden, T.J., di Meglio, J.M. and Auroy, P. (1998) Anomalous adhesion in adsorbed polymer layers. *Eur Phys J B*, **3**, 211-6.

Sheu, M.T., Huang, J.C., Yeh, G.C. and Ho, H.O. (2001) Characterization of collagen gel solutions and collagen matrices for cell culture. *Biomaterials*, **22**, 1713-9.

Shnyrov, V.L. and Mateo, P.L. (1993) Thermal transitions in the purple membrane from Halobacterium halobium. *FEBS Lett*, **324**, 237-40.

Smith, S.B., Cui, Y. and Bustamante, C. (1996) Overstretching B-DNA: the elastic response of individual double-stranded and single-stranded DNA molecules. *Science*, **271**, 795-9.

Smith, S.B., Finzi, L. and Bustamante, C. (1992) Direct mechanical measurements of the elasticity of single DNA molecules by using magnetic beads. *Science*, **258**, 1122-6.

Stark, M., Möller, C., Müller, D.J. and Guckenberger, R. (2001) From images to interactions: high-resolution phase imaging in tapping-mode atomic force microscopy. *Biophys J*, **80**, 3009-18.

Stroh, C.M., Ebner, A., Geretschlager, M., Freudenthaler, G., Kienberger, F., Kamruzzahan, A.S., Smith-Gill, S.J., Gruber, H.J. and Hinterdorfer, P. (2004) Simultaneous topography and recognition imaging using force microscopy. *Biophys J*, **87**, 1981-90.

Sugawara, Y., Ohta, M., Ueyama, H. and Morita, S. (1995) Defect motion on an InP(110) surface observed with noncontact atomic force microscopy. *Science*, **270**, 1646-8.

Svoboda, K. and Block, S.M. (1994) Biological applications of optical forces. *Annu Rev Biophys Biomol Struct*, **23**, 247-85.

Tamayo, J. and Garcia, R. (1996) Deformation, contact time, and phase-contrast in tapping mode scanning force microscopy. *Langmuir*, **12**, 4430-5.

Tamayo, J. and Garcia, R. (1998) Relationship between phase-shift and energy-dissipation in tapping-mode scanning force microscopy. *Applied Physics Letters*, **73**, 2926-8.

Taneva, S.G., Caaveiro, J.M., Muga, A. and Goni, F.M. (1995) A pathway for the thermal destabilization of bacteriorhodopsin. *FEBS Lett*, **367**, 297-300.

Thompson, J.B., Kindt, J.H., Drake, B., Hansma, H.G., Morse, D.E. and Hansma, P.K. (2001) Bone indentation recovery time correlates with bond reforming time. *Nature*, **414**, 773-6.

Toda, A., Kitazawa, M. and Yagi, A. (2004) Silicon tip cantilevers for force microscopy in water with resonance of 20 kHz or above. *Jpn J Appl Phys*, **43**, 4671-5.

Tokunaga, M., Aoki, T., Hiroshima, M., Kitamura, K. and Yanagida, T. (1997) Subpiconewton intermolecular force microscopy. *Biochem Biophys Res Commun*, **231**, 566–9.

Torres, J., Stevens, T.J. and Samso, M. (2003) Membrane proteins: the 'Wild West' of structural biology. *Trends Biochem Sci*, **28**, 137-44.

Tortonese, M. (1997) Cantilevers and tips for atomic force microscopy. *IEEE Eng Med Biol Mag*, **16**, 28-33.

Treolar, L.R.G. (1975) *The physics of rubber elasticity*. Oxford University Press, Oxford.

Tskhovrebova, L. and Trinick, J. (2003) Titin: properties and family relationships. *Nat Rev Mol Cell Biol*, **4**, 679-89.

Viani, M.B., Pietrasanta, L.I., Thompson, J.B., Chand, A., Gebeshuber, I.C., Kindt, J.H., Richter, M., Hansma, H.G. and Hansma, P.K. (2000) Probing protein–protein interactions in real time. *Nat Struct Biol*, **7**, 644-7.

Viani, M.B., Schäffer, T.E., Chand, A., Rief, M., Gaub, H.E. and Hansma, P.K. (1999) Small cantilevers for force spectroscopy of single molecules. *J. Appl. Phys.*, **86**, 2258-62.

Viani, M.B., Schäffer, T.E., Paloczi, G.T., Pietrasanta, L.I., Smith, B.L., Thompson, J.B., Richter, M., Rief, M., Gaub, H.E., Plaxco, K.W., Cleland, A.N., Hansma, H.G. and Hansma, P.K. (1999) Fast imaging and fast force spectroscopy of single biopolymers with a new atomic force microscope designed for small cantilevers. *Rev Sci Ins*, **70**, 4300-3.

Wagner, P. (1998) Immobilization strategies for biological scanning probe microscopy. *FEBS Lett*, **430**, 112-5.

Wallin, E. and von Heijne, G. (1998) Genome-wide analysis of integral membrane proteins from eubacterial, archaean, and eukaryotic organisms. *Protein Sci*, **7**, 1029-38.

Walters, D.A., Cleveland, J.P., Thomson, N.H., Hansma, P.K., Wendman, M.A., Gurley, G. and Elings, V. (1996) Short cantilevers for atomic force microscopy. *Rev. Sci. Ins.*, **67**, 3583-90.

Wang, M.D., Yin, H., Landick, R., Gelles, J. and Block, S.M. (1997) Stretching DNA with optical tweezers. *Biophys J*, **72**, 1335-46.

Weihs, T.P., Nawaz, Z., Jarvis, S.P. and Pethica, J.B. (1991) Limits of imaging resolution for atomic force microscopy of molecules. *Applied Physics Letters*, **59**, 3536-8.

Weissman, J.S. and Kim, P.S. (1991) Reexamination of the folding of BPTI - predominance of native intermediates. *Science*, **253**, 1386-93.

White, S.H. and Wimley, W.C. (1999) Membrane protein folding and stability: physical principles. *Annu Rev Biophys Biomol Struct*, **28**, 319-65.

Williams, P.M. and Evans, E. (2002) Dynamic Force Spectroscopy: II. Multiple Bonds. In Flyvbjerg, H., Jülicher, F., Ormos, P. and David, F. (eds.), *Physics of Bio-Molecules and Cells*. EDP Sciences – Springer-Verlag, Vol. Ecoles des HOUCHES d'Ete, LXXV, pp. 186-203.

Williams, P.M., Fowler, S.B., Best, R.B., Toca-Herrera, J.L., Scott, K.A., Steward, A. and Clarke, J. (2003) Hidden complexity in the mechanical properties of titin. *Nature*, **422**, 446-9.

Wong, S.S., Woolley, A.T., Odom, T.W., Huang, J.L., Kim, P., Vezenov, D.V. and Lieber, C.M. (1998) Single-walled carbon nanotube probes for high-resolution nanostructure imaging. *Appl Phys Lett*, **73**, 3465-7.

Yang, W.Y. and Gruebele, M. (2003) Folding at the speed limit. *Nature*, **423**, 193-7.

Yohannan, S., Faham, S., Yang, D., Whitelegge, J.P. and Bowie, J.U. (2003) The evolution of transmembrane helix kinks and the structural diversity of G protein-coupled receptors. *Proc Natl Acad Sci U S A*, **101**, 959–63.

Erklärung

Hiermit versichere ich, daß ich die vorliegende Arbeit ohne unzulässige Hilfe Dritter und ohne Benutzung anderer als der angegebenen Hilfsmittel angefertigt habe; die aus fremden Quellen direkt oder indirekt übernommen Gedanken sind als solche kenntlich gemacht. Die Arbeit wurde bisher weder im Inland noch im Ausland in gleicher oder ähnlicher Form einer anderen Prüfungsbehörde vorgelegt.

Die vorliegende Arbeit wurde von November 2002 bis August 2005 unter der wissenschaftlichen Betreuung von Frau Prof. Dr. Petra Schwille und Herrn Prof. Dr. Daniel J. Müller am Biotechnologischen Zentrum der Technischen Universität Dresden durchgeführt.

Dresden, den 3. August 2005

Harald Janovjak